Development of Micro-Electromechanical Systems in GaN

Thesis by

Robert P. Strittmatter

In Partial Fulfillment of the Requirements

for the Degree of

Doctor of Philosophy

California Institute of Technology

Pasadena, California

2003

(Submitted June 30, 2003)

To Evan Zachary Arlett Strittmatter

List of Publications

Work related to this thesis has been or will be published under the following titles:

Fabrication of GaN suspended microstructures,
R.P. Strittmatter, R.A. Beach, T.C. McGill, Applied Physics Letters, **17**, (12), 110 (2001).

GaN Schottky diodes for piezoelectric strain sensing,
R.P. Strittmatter, R.A. Beach, J. Brooke, E. Preisler, G.S. Picus, T.C. McGill, Journal of Applied Physics, **93**, (8), 1 (2003).

Piezoelectrically enhanced capacitive strain sensors using GaN MIS diodes,
R.P. Strittmatter, R.A. Beach, G.S. Picus, T.C. McGill, submitted to Journal of Applied Physics.

Piezoelectric strain sensing with GaN MIS diodes,
R.P. Strittmatter, R.A. Beach, G.S. Picus, T.C. McGill, submitted to Sensors and Actuators A.

Measurement of the quality factor of GaN micro-resonators,
R.P. Strittmatter, R.A. Beach, G.S. Picus, T.C. McGill, in production for Journal of Vacuum Science and Technology.

Work not contained in this thesis:

Nitridation of Epitaxially Grown 6.1A Semiconductors Studied by X-ray Photoelectron Spectroscopy,
E.J. Preisler, R.P. Strittmatter, T.C. McGill, submitted to Applied Surface Science.

Spin injection from ferromagnetic metal to semiconductor via a Schottky barrier,

J. Brooke, S. Ichiriu, N. Oldham, E. Preisler, R.P. Strittmatter, T.C. McGill, in production.

Abstract

This thesis is focused on the development of micro-electromechanical systems (MEMS) in III-V nitride semiconductors, with a primary emphasis on gallium-nitride (GaN). Though GaN exhibits unique properties that make it an effective platform for MEMS devices, to date, this field of study has received almost no attention in the nitride community. As a result, the research outlined in this thesis represents the very first steps in the development of GaN for this application.

A critical issue for the advancement of GaN MEMS is the development of transducers to actuate and sense motion in deformable microstructures. In the second chapter of this text, we present two classes (and four instances) of strain transducers, native to GaN, which take advantage of its large piezoelectric constants. Unlike in conventional insulating crystals, the presence of free charge carriers in the semiconductor has a strong bearing on its response to strain. The action of piezoelectricity within a semiconductor allows for a family of versatile and sensitive transducers in GaN.

Another basic issue facing this new field is the establishment of a fabrication technology to create suspended structures on the micron and nanometer scale. In Chapter 3, we describe two processes that were developed to fashion a wide range of MEMS devices in both p-type and n-type GaN. Each process exploits a distinct electrochemical etch which is dopant selective, the two etches being complementary. In one process, a photo-electrochemical method was adapted to undercut p-GaN epilayers that were grown on top of n-type sacrifical layers. For the other, a novel anodic etch was developed to undercut n-GaN layers. Both methods feature high dopant selectivity, rapid undercutting rates, and lateral etch control.

The final chapter brings together both major research thrusts in the study of resonant cantilevers with integrated piezoelectric transducers. These devices are evaluated in terms of two important benchmarks: (i) the sensitivity to detect endpoint

displacement, and (ii) the quality factor of the resonance. In the former case, the devices met up with our theoretical expectations; in the latter, no fundamental material limitation was found.

Contents

List of Figures

List of Tables

Chapter 1 Introduction

1.1 Thesis Overview

This thesis is focused on the development of micro-electromechanical systems (MEMS) in III-V nitride semiconductors, with a primary emphasis on gallium-nitride (GaN). Though GaN exhibits unique properties that make it an effective platform for MEMS devices, to date, this field of study has received almost no attention in the nitride community. As a result, the research outlined in this thesis represents the very first steps in the development of GaN for this application.

A critical issue for the advancement of GaN MEMS is the development of transducers to actuate and sense motion in deformable microstructures. In the second chapter of this text, we present two classes (and four instances) of strain transducers, native to GaN, which take advantage of its large piezoelectric constants. Unlike in conventional insulating crystals, the presence of free charge carriers in the semiconductor has a strong bearing on its response to strain. The action of piezoelectricity within a semiconductor allows for a family of versatile and sensitive transducers in GaN.

Another basic issue facing this new field is the establishment of a fabrication technology to create suspended structures on the micron and nanometer scale. In Chapter 3, we describe two processes that were developed to fashion a wide range of MEMS devices in both p-type and n-type GaN. Each process exploits a distinct electrochemical etch which is dopant selective, the two etches being complementary. In one process, a photo-electrochemical method was adapted to undercut p-GaN epilayers that were grown on top of n-type sacrifical layers. For the other, a novel anodic etch was developed to undercut n-GaN layers. Both methods feature high dopant selectivity, rapid undercutting rates, and lateral etch control.

The final chapter brings together both major research thrusts in the study of res-

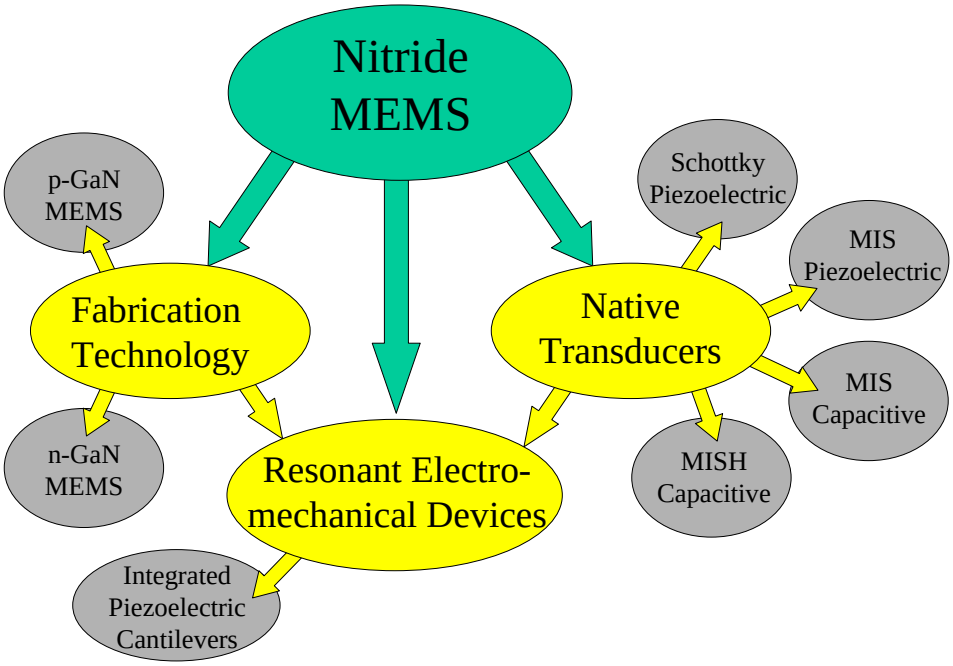

Figure 1.1: Overview of Thesis.

onant cantilevers with integrated piezoelectric transducers. These devices are evaluated in terms of two important benchmarks: (i) the sensitivity to detect endpoint displacement, and (ii) the quality factor of the resonance. In the former case, the devices met up with our theoretical expectations; in the latter, no fundamental material limitation was found.

Fig. 1.1 gives a graphical overview of the relationship between the major results contained in this thesis, and a sense of the overall flow of the presentation.

1.2 Background and Motivation

The wide bandgap III-V nitride material system, including GaN, AlN, InN and derivative ternary alloys, has been the subject of intensive research in recent years. Initial interest in these semiconductors was spurred by the demonstration (and later commercialization) of blue and violet light-emitting diodes which used a InGaN quantum-well for the active layer [1]. Soon after came the first reports of continuous-wave laser diodes [2], which have since achieved room-temperature lifetimes in excess of

10^4 hours. More recently, the large and tunable direct bandgap of $Al_xGa_{1-x}N$ alloys (ranging from 3.4 eV for GaN to 6.2 eV for AlN) has received attention for solar-blind ultraviolet photodetectors [3].

Aside from these opto-electronic applications, the nitrides have shown considerable promise for use in high speed and high power electronics. By far, the most significant advancement in this arena has been heterostructure field-effect transistors (HFETs) operating at microwave frequencies (10-100 GHz) [4]. These transistors take advantage of the two-dimensional electron gas which forms at a AlGaN/GaN heterojunction, with unusually large carrier concentrations ($10^{13}/cm^2$) that arise from the combined effect of spontaneous and piezoelectric polarization [5]. In addition, the large critical field for avalanche breakdown in these wide bandgap semiconductors has motivated interest in high power switches and rectifiers [6].

A significant hurdle in the development of nitride devices has been the lack of a suitable lattice-matched substrate. To date, GaN has been grown on highly incommensurate substrates such as sapphire or SiC, leading to a high density of crystallographic defects. Recently, a major effort to create free-standing GaN wafers has culminated in their commercial release within the year. Epitaxial growth on these substrates will lead to major improvements for the MEMS devices discussed here, as well as for nitride electronics as a whole.

Outside of the nitrides, several wide bandgap semiconductors have been studied for use in MEMS. Most advanced among these is SiC, whose high temperature stability allows it to feature in microsensors that can operate in higher than 600 °C ambients [7]. Furthermore, the large elastic modulus of this material is advantageous for high frequency microresonators [8]. Also notable in this arena is ZnO, a piezoelectric semiconductor which has long been used in thin film surface acoustic wave devices . More recently, this material has been incorporated into Si MEMS in the form of a sputter deposited surface layer [9]. However, the low crystal quality of this coating results in effective piezoelectric constants which are much lower than in bulk ZnO [10]. Furthermore, the highly reactive and temperature sensitive nature of this material limits its broader applicablity in microdevices [11].

Several material properties of GaN make it an attractive platform for MEMS applications. Foremost among these is the unique combination of strong piezoelectric activity with developed semiconductor capabilities. As discussed later, the orientation of the piezoelectric fields in GaN is ideal for transducers based on simple vertical devices patterned on the semiconductor surface. To sense (or actuate) strain, the transducer must only be placed on one surface of a deformable microstructure, with the semiconductor itself serving as the back contact. These sensors become even more capable when they are integrated in close proximity to monolithic amplifiers or signal processing stages. In addition to its inherent transduction ability, the unusually high chemical inertness of GaN makes it suitable for MEMS applications in corrosive environments. Likewise, its thermal stability is suited for high temperature applications, such as gas pressure sensors for internal combustion engines. Radiation hardness allows it to feature in gyros for space satellites or instrumentation for nuclear power systems. Transparency at visible wavelengths, coupled with the advanced opto-electronic abilities of the nitrides, could find application in optical micro-switches, waveguides, and even suspended microdisk lasers. And finally, as discussed later, GaN can be machined to the sub-micron level by means of a versatile fabrication technology. This process allows for a wide range of MEMS geometries, including microfluidic channels and vertically stacked microstructures.

1.3 Outline of Thesis

The remainder of this thesis is organized as follows.

Chapter 2 is devoted to the development of transducers native to GaN. All of the transducers studied here are formed out of some type of semiconductor diode. Based on their sensing methodology, these devices can be divided into two broad classes. In the first class, strain in the semiconductor is detected by a transient voltage which arises across the diode. These sensors are the most akin to conventional piezoelectrics, and can measure only time varying strain. Two instances of this type are presented: Schottky and metal-insulator-semiconductor (MIS). In the

second class, strain is sensed by a steady-state change in the capacitance of the diode. These transducers can measure both static and ac strain. On the surface, they resemble ordinary capacitive sensors; in reality, however, their operation is also heavily rooted in piezoelectric effects. Here again, two instances are presented: MIS and metal-insulator-semiconductor-heterojunction (MISH).

The first section of Chapter 2 gives a brief survey of piezoelectric effects in III-V nitrides and lays down a basic framework to model the effects of strain in the context of semiconductor device physics.

In the next section, we report on the electromechanical response of Schottky diodes, formed on n-GaN, as a function of the strain frequency and the applied dc bias. These measurements reveal high strain detection sensitivity for frequencies above $\sim$ 10 Hz. The observed amplitude and phase of the electromechanical output can be largely explained using a simple model of piezoelectric charge generation on either side of the depletion layer. In addition, the noise spectral density of these diodes was measured under the same conditions, allowing us to infer the signal to noise ratio for strain detection.

In section 2.3, we present data on the electromechanical response of high quality n-GaN MIS diodes formed with SiO_2. By modifying the earlier model to account for the distinct device physics of a MIS capacitor, excellent agreement with the measurements is obtained. For these devices, the strain response is strongly dependent on the bias applied to the diode. At the end of the section, we demonstrate how this dependence can be used to effect nonlinear mixing or parametric amplification of the strain signal within the transducer itself.

In section 2.4, MIS diodes are studied once again, but this time for capacitive strain sensing. When subjected to static strain, they were found to exhibit a steady-state change in capacitance; as a result, they can be used to detect strain with frequencies all the way down to dc. We model the role of piezoelectricity in this context, and obtain excellent agreement with measurements. The model is then used to develop design criteria which optimize the strain detection sensitivity. The sensitivity of the devices tested here rivals that of the best silicon piezoresistive sensors, but could attain

nearly tenfold improvement with only minor design changes. Finally, we consider the effects of interface states on sensor performance and demonstrate how static strain sensing in GaN MIS diodes is enabled by the high quality of the oxide interface.

In the final section (2.5), we present preliminary data on capacitive sensing in MISH diodes. These devices exhibit a sharp knee in the capacitance-voltage profile when the 2DEG at the heterojunction starts to deplete under the gate. When biased in this transition region, they were found to exhibit a large response to strain. While these initial results seem promising, further effort is required to both calibrate and model these sensors.

Chapter 3 describes two processes that were developed to allow for the fabrication of suspended microstructures in both p-type and n-type GaN. For the first process, a dopant selective photo-electrochemical (PEC) etch was adapted to undercut p-GaN epilayers that were grown on top of n-type sacrifical layers. In the second, a novel anodic electrochemical etch is used achieve the converse result. Both fabrication methods feature high dopant selectivity, rapid undercutting rates, and lateral etch anisotropy.

The first section of the chapter offers a brief survey on wet etching in the nitrides, focusing on the chemical reactions and semiconductor electrochemistry which govern the two etches discussed above. The next section describes in detail the process developed to fabricate p-GaN microstructures. In addition to technical aspects of the procedure itself, data is presented on a wide range of devices which were fashioned in this way, including microfluidic pumps, piezoelectric strain sensors, and sub-micron scale beams. The final section deals with the fabrication of n-GaN devices. Though this process is currently less developed, it will likely play a leading role in the future development of GaN MEMS. Here, we outline the technical steps which are unique to the anodic etch, and present data on n-GaN cantilevers. At the end of this section, we demonstrate the use of anodic etching to create three-dimensional stratified MEMS in GaN.

Chapter 4 concludes the thesis with data and modeling of simple cantilevers, fashioned in n-GaN, with integrated Schottky and MIS transducers. These electrome-

chanical devices were evaluated in terms of their endpoint displacement sensitivity and their resonance quality factor Q. The first two sections deal with experimental details related to the measurements, including: (i) the epitaxial structure of the GaN samples; (ii) the overall device geometry; (iii) the steps followed during fabrication; and (iv) the setup used to excite the cantilevers and measure their electrical response in an evacuated ambient. The following section (4.3) sets forth a model of piezoelectric transuction through a Schottky contact on the top surface of the cantilever. The analysis here differs from our earlier results to account for the nonuniform strain inside a bending beam. At the conclusion of this section, an expression for the gauge factor is obtained, relating the output voltage to the endpoint deflection of the cantilever. Section 4.4 presents data on the impulse response of the devices in varying ambient pressures. These measurements are then used to infer the sensitivity and the quality factor. Though the sensitivity of the transducers met up with our theoretical expectations, the Q's were found to be rather low. At this point, we discuss possible dampening factors which may be limiting the Q. In particular, we derive a theoretical expression for the acousto-electric dampening caused by the ohmic dissipation of electrical currents in the bulk of the semiconductor. This loss mechanism is far too small to account for the data, and furthermore, does not impose a fundamental limitation for the use of GaN in micro-resonators. In the conclusion of this chapter, we speculate on the causes of the low Q's, and propose future research paths aimed at eliminating them.

Bibliography

[1] S. Nakamura, M. Senoh, N. Iwasa, and S. Nagahama, Applied Physics Letters **67**, 1868 (1995).

[2] S. Nakamura, M. Senoh, S. Nagahama, N. Iwasa, T. Yamada, T. Matsushita, Y. Sugimoto, and H. Kiyoku, Appl. Phys. Lett **69**, 4056 (1996).

[3] A. Osinsky, S. Gangopadhyay, R. Gaska, B. Williams, M. Khan, D. Kuksenkov, and H. Temkin, Appl. Phys. Lett **71**, 2334 (1997).

[4] M. Micovic, N. Nguven, P. Janke, W. Wong, P. Hashimoto, L. McCray, and C. Nguyen, Electronics Letters **36**, 358 (2000).

[5] E. Yu, X. Dang, P. Asbeck, S. Lau, and G. Sullivan, Journal of Vacuum Science and Technology B **17**, 1742 (1999).

[6] Z. Bandic, P. Bridger, E. Piquette, T. McGill, R. Vaudo, V. Phanse, and J. Redwing, Appl. Phys. Lett **74**, 1266 (1999).

[7] X. Song, S. Rajgopal, J. Melzak, C. Zorman, and M. Mehregany, Silicon Carbide and Related Materials 2001, Pts 1 and 2, Proceedings Materials Science Forum **389**, 755 (2002).

[8] Y. Yang, K. Ekinci, X. Huang, L. Schiavone, M. Roukes, C. Zorman, and M. Mehregany, Appl. Phys. Lett **78**, 162 (2001).

[9] D. Polla and L. Francis, Annual Review of Material Science **28**, 563 (1998).

[10] F. Blom, F. Van de Pol, G. Bauhuis, and T. Popma, Thin Solid Films **204**, 365 (1991).

[11] T. Xu, G. Wu, G. ZHang, and Y. Hao, Sensors and Actuators A **104**, 61 (2003).

Chapter 2 Piezoelectric Transduction in III-V Nitride Semiconductors

2.1 Overview

The following chapter focuses on piezoelectric transduction in GaN. Two classes of sensors are presented, these being distinguished by the nature of their electrical response to strain. In the first class, strain is measured by the transient voltage which develops across the terminals of the sensor; in the second, strain is detected by a change in the steady-state capacitance. Every transducer presented in this chapter is housed in a conventional semiconductor device: Schottky and MIS diodes for the first class, MIS and MISH diodes for the second. The ability of these common devices to sense (and induce) strain stems from strong piezoelectric activity inside the semiconductor. To set the stage for the discussions to follow, this section gives a brief survey of polarization effects in the III-V nitrides.

Fig. 2.1 shows a schematic of the GaN crystal structure (wurtzite) common to all of the nitrides. This structure consists of alternating hexagonal planes of Ga and N which, when viewed in pairs, are stacked vertically following an ABAB sequence. By convention, the c-axis is perpendicular to these planes, pointing from Ga to N along the vertical bonds shown in the figure. On sapphire or SiC substrates, GaN grows parallel to the c-axis. Due to the lack of mirror symmetry across the basal planes, however, two distinct polarities of the growth can occur, and sometimes even a mixture. For the samples discussed in this chapter, all grown by MOCVD on sapphire, the GaN is unipolar and oriented along the c-axis, i.e., the arrow in Fig. 2.1 points away from the substrate.

The ionicity of the III-V nitride compounds (N being electropositive), coupled with the wurtzite structure, give rise to strong polarization fields. In addition to the (piezoelectric) polarization which results from strain, the symmetry class of the crystal allows for spontaneous (or permanent) polarization along the c-axis. Using reduced engineering notation [2], the polarization vector P_i in GaN can be expressed by:

$$P_i = \epsilon_0 \chi_{ij} E_j + e_{iJ} S_J + P_i^{sp} \tag{2.1}$$

where χ_{ij} is the susceptibility tensor, E_j is the electric field, e_{iJ} is the piezoelectric

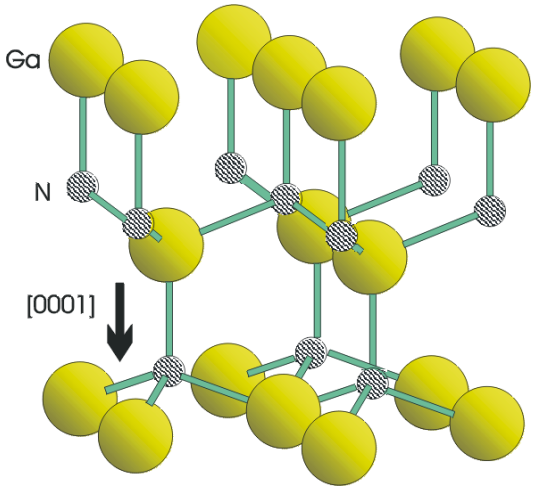

Figure 2.1: Schematic of the GaN wurtzite crystal structure. (From Beach [1])

tensor, S_J is the (6-component) strain vector, and P_i^{sp} is the spontaneous polarization [3]. Note that summation is implied, and upper case indices refer to one of six components. The first term on the right side of Eqn. 2.1 refers to the ordinary dielectric contribution to the polarization, while the last two relate to the piezoelectric and spontaneous contributions.

Given the symmetry of the wurtzite crystal, the (3×6) piezoelectric matrix e_{iJ} will have only the following nonvanishing entries:

$$\begin{pmatrix} . & . & . & . & e_{15} & . \\ . & . & . & e_{15} & . & . \\ e_{31} & e_{31} & e_{33} & . & . & . \end{pmatrix} \tag{2.2}$$

with only three of these quantities being independent. Here, the z (or x_3) axis coincides with the c-axis of the crystal; x_1 and x_2 are any arbitrary perpendicular directions in the basal plane.

Phys. Const.	GaN	AlN	InN	Reference
e_{31} (C/m^2)	-0.36	...	...	[6]
e_{31} (C/m^2)	...	-0.58	...	[7]
e_{31} (C/m^2)	-0.49	-0.60	-0.57	[5]
e_{33} (C/m^2)	1.0	...	...	[6]
e_{33} (C/m^2)	...	1.55	...	[7]
e_{33} (C/m^2)	0.73	1.46	0.97	[5]
P_3^{sp} (C/m^2)	-0.029	-0.081	-0.032	[5]

Table 2.1: List of reported piezoelectric constants for the nitrides. (Adapted from Yu *et al.* [4])

Table 2.1 lists values for the spontaneous and piezoelectric constants gleaned from the nitride literature. While these values are fairly well established for AlN, there is still serious disagreement for GaN no doubt resulting from the wide range of material quality in use [4]. For InN, only theoretical values have been reported. For the modeling of GaN transducers later in this chapter, theoretical values were used: e_{31} = -0.49 and e_{33} = 0.73 C/m^2 [5].

Table 2.2 compares the nitride constants with those for some common piezoelectric materials. Note that the nitrides have significantly larger activity than quartz, the mainstay of crystal resonators. Furthermore, for the wurtzite materials, longitudinal strains (the first 3 components of S_J) are coupled into polarization along the z-axis; this is ideal for strain sensors which are based on vertical devices patterned on a c-plane surface. The vertical electric field in these devices can also be used to induce stress in the crystal by means of the converse piezoelectric effect:

$$T_I = c_{IJ} S_J - e_{jI} E_j \tag{2.3}$$

where T_I is the 6-component stress vector and c_{IJ} is the elastic stiffness matrix [3].

The electrostatic consequences of polarization in GaN can be derived from Poisson's equation $\nabla \cdot \vec{D} = \rho_f$, where ρ_f is the free charge density and $\vec{D} \equiv \epsilon_0 \vec{E} + \vec{P}$ is the displacement [8]. For all of the measurements discussed later, the strain in the GaN was longitudinal, with negligible shear components (S_4,S_5,S_6=0). Furthermore, in all of the transducers, the electric field is directed vertically except at the very device

Material	Symmetry Class	e_{11}	e_{14}	e_{15}	e_{22}	e_{31}	e_{33}	Ref.
Gallium Arsenide	Cub. 43m		0.154					[3]
Quartz	Trig. 32	0.171	-0.0436					[3]
GaN	Hex. 6mm			?		-0.49	0.73	[5]
InN	Hex. 6mm			?		-0.57	0.97	[5]
Zinc Oxide	Hex. 6mm			-0.48		-0.573	1.32	[3]
AlN	Hex. 6mm			?		-0.60	1.46	[5]
Lithium Niobate	Trig. 3m	.	.	3.7	2.5	0.2	1.3	[3]

Table 2.2: Piezoelectric activity of various materials. (Adapted from Ballantine *et al.* [3])

periphery. Under these conditions, Poisson's equation will read:

$$\frac{dE_z}{dz} = \frac{(\rho_f + \rho_b)}{\epsilon_{33}} \tag{2.4}$$

where ϵ_{33} is the dielectric constant and ρ_b is the volume bound charge density brought on by strain:

$$\rho_b = -e_{3J}\frac{dS_J}{dz} \tag{2.5}$$

In addition to this bulk charge, polarization will cause a bound sheet charge density σ_b to appear at both c-plane surfaces of the crystal. At the upper face, it takes on the value:

$$\sigma_b = e_{3J}S_J + P_3^{sp} \tag{2.6}$$

This bound charge, in addition to any free sheet charge, will determine the boundary conditions for the electric field at the edges of the GaN layer.

Bibliography

[1] R. Beach, *Column III Nitride Growth, Characterization, and Devices*, 1st ed. (California Institute of Technology, Pasadena, CA, USA, 2001).

[2] J. Nye, *Physical Properties of Crystals*, 2nd ed. (Oxford University Press, New York, NY, USA, 1985).

[3] D. Ballantine, R. White, S. Martin, A. Ricco, E. Zellers, G. Frye, and H. Wohltjen, *Acoustic Wave Sensors*, 1st ed. (Academic Press, San Diego, CA, USA, 1997).

[4] E. Yu, X. Dang, P. Asbeck, S. Lau, and G. Sullivan, Journal of Vacuum Science and Technology B **17**, 1742 (1999).

[5] A. Zoroddu, F. Bernardini, P. Ruggerone, and V. Fiorentini, Physical Review B **64**, 1 (2001).

[6] A. D. Bykhovski, B. L. Gelmont, and M. S. Shur, Journal of Applied Physics **81**, 6332 (1997).

[7] J. Gualtieri, J. Kosinski, and A. Ballato, IEEE Transactions on Ultrasonics Ferroelectrics and Frequency Control **41**, 53 (1994).

[8] R. Wangsness, *Electromagnetic Fields*, 2nd ed. (John Wiley and Sons, New York, NY, USA, 1986).

2.2 Schottky Diodes

2.2.1 Introduction

In recent years, piezoelectric effects in III-V nitrides have been studied extensively. For the most part, this research has centered on the effects of static strain built into nitride heterostructures, for example, in heterostructure field effect tranisitors (HFETs) [1] or quantum-well light-emitting diodes [2]. The study of nitride devices under dynamic strain conditions may prove to be an equally fertile area of research. Aside from the more standard applications of semiconductor strain sensors and acoustic wave circuit elements, this research is highly relevant to the emerging field of GaN micro-electromechanical systems (MEMS). Owing to its unique material properties (wide-bandgap, large piezoelectric coefficients, chemical inertness), coupled with a well developed fabrication technology [3], GaN is poised to make a major impact in the arena of micron and sub-micron scale mechanical devices. For this application, effective transducer designs must be studied and ultimately optimized for the purposes of exciting and detecting strain.

Previous research on strain detection in the nitrides has focused on exploiting their piezoresistive properties [4],[5],[6],[7]. In measurements on n-GaN, Bykhovski *et al.* found low, metallic-grade gauge factors in response to static strain but gauge factors as high as ∼130 for dynamic strain [5]. For p-GaN, Gaska *et al.* carried out piezoresistance measurements using Schottky contacts and observed very large gauge factors (∼260) depending upon the bias applied across these contacts [4]. This large piezoresistive effect was attributed to strain-induced changes in both the bulk and contact resistivities.

Though GaN has very large piezoelectric constants, surprisingly little effort has been directed toward the study of strain sensors which harness the piezoelectric effect directly. This may stem from the common notion that free charge carriers in GaN will move rapidly to negate any piezoelectric charge that is induced by strain. However, in devices which block the flow of free charge currents, such as Schottky, metal-insulator-semiconductor (MIS) or p-n diodes, this screening effect is hindered. In such devices,

a voltage can develop across the depletion region in response to piezoelectric charge. Loosely speaking, the persistence of this voltage will depend upon the effective RC time constant of the device and the electrical network to which it is connected. For state of the art Schottky diodes on n-GaN, with their large differential resistance in reverse, this persistence time can be on the order of seconds. Importantly, these same basic semiconductor devices can also be used to excite mechanical strain via the converse piezoelectric effect.

In this work, we have studied the electrical response of Schottky diodes on n-GaN resulting from simple harmonic strain disturbances. This response was measured as a function of the excitation frequency and the dc bias applied to the diode. On the basis of the combined data, we conclude that the transduction mechanism at work in these devices is piezoelectric and not piezoresistive in nature. Sec. II of this paper describes the experimental setup used for these measurements. In Sec. III(A), we present the observed dependence of the electromechanical signal on both the strain frequency and the applied bias. This data is then compared with a model for piezoelectric transduction in a Schottky diode, which we outline in Sec. III(B). Finally, in Sec. III(C), we present measurements of the voltage noise spectral density under the same conditions and infer a signal to noise ratio for strain detection.

2.2.2 Experimental Setup

The GaN samples used in this experiment were grown by metalorganic chemical vapor deposition (MOCVD) on a c-plane sapphire substrate. The growth consists of three epitaxial layers: (i) a 40 nm AlN buffer layer; (ii) a 2.0 μm n^+-GaN base layer which was doped with Si at a level of $10^{18}/\text{cm}^3$; and (iii) a 2.0 μm surface layer lowly doped at $3.0 \times 10^{16}/\text{cm}^3$. The GaN layers were grown at a substrate temperature of 1050 $^\circ$C using trimethylgallium and ammonia for precursors with a V/III molar flow ratio of 2800. The crystal orientation of the resulting film was Ga-polar (0001).

For the Schottky diodes, the ohmic contact consists of a Al-Ni-Au (50 nm-30 nm-50 nm) stack which was sputter deposited after a brief surface etch in dilute

hydro-flouric acid. The Schottky contact was formed by sputtering 100 nm of Au on a surface cleaned only by standard solvents. The current-voltage characteristics for a typical Schottky diode are shown in Fig. 2.2. Fits to the experimental data give a forward state ideality factor of $n \sim 2.1$ and a differential resistance at 0 V bias in excess of $10^{12}\Omega$. The reverse leakage current, shown in the semi-log inset of Fig. 2.2, is likely the result of field-crowding effects near the periphery of the Schottky contact. Separate experiments have revealed that insulating guard rings dramatically reduce this leakage.

Fig. 2.18 shows the experimental setup used to study the electrical response of these diodes to mechanical strain. GaN samples were cleaved into a rectangular shape with a length of 30 mm and a width of 5 mm. Referring to the coordinate axis shown in the figure, both the Schottky and ohmic contacts for the diode were patterned in thin (100 μm) strips oriented along the y-axis with a total area of 0.2 mm^2. Each strip was connected at one end to a 100 $\mu m \times 100$ μm wire-bond pad that was electrically isolated from the GaN below by 200 nm SiN insulating layer.

One end of the rectangular sample was firmly adhered to a rigid support fixture, thereby forming a cantilever. A thin wire, affixed at the underside of the free end of the cantilever, was connected to a solenoidal transducer. This transducer supplied a time varying point force along the z-axis which excites the fundamental bending mode of the cantilever structure. Accordingly, the primary deformation of the GaN epilayer is a mixture of longitudinal strain in x and in z, which we denote as S_1 and S_3 respectively using the standard reduced notation [8]. Due to the mechanically free boundary condition on the upper surface of the GaN layer, these components of the strain are related by,

$$S_3 = -\frac{C_{31}}{C_{33}} S_1 \tag{2.7}$$

where C_{ij} are the components of the reduced GaN elastic tensor. Given the relative thinness of the GaN epilayer (4 μm) compared to the sapphire substrate (400 μm), the strain is approximately uniform in z across the film thickness, but varies in x along the length of the cantilever.

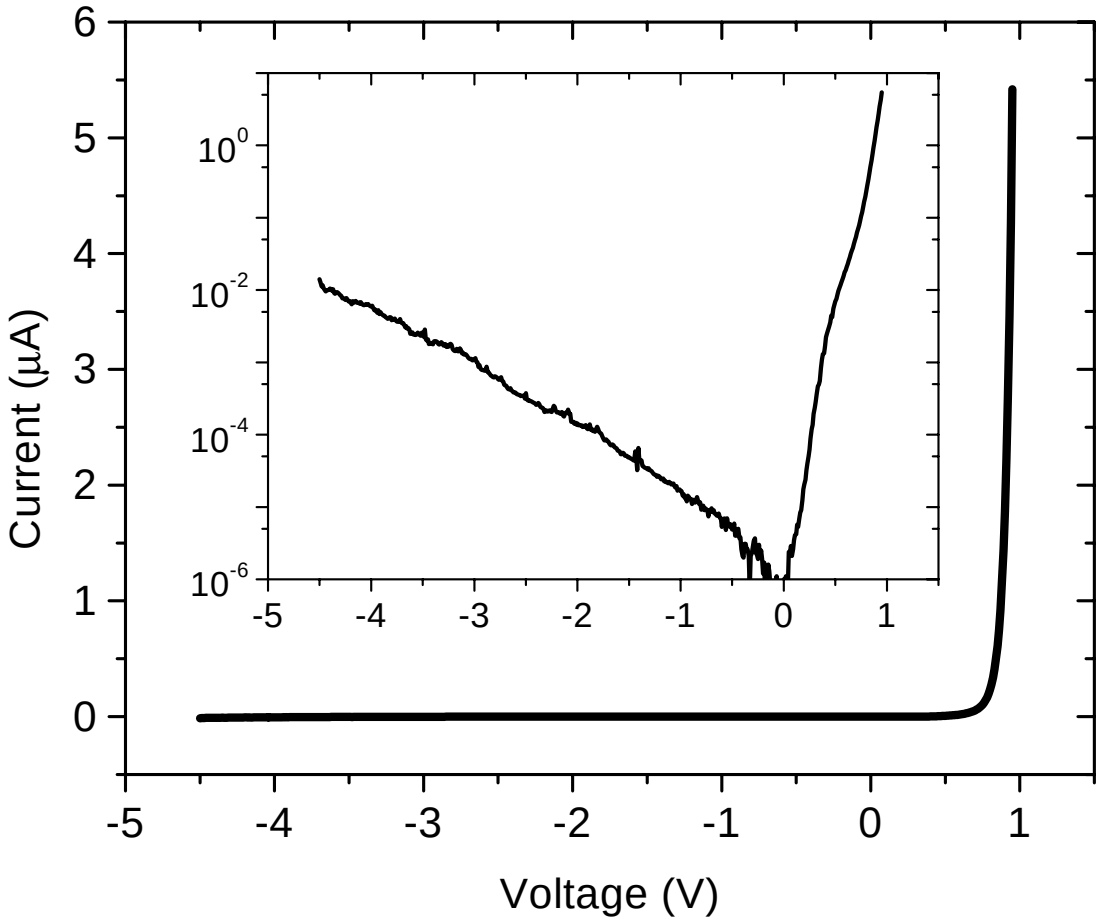

Figure 2.2: Current-voltage characteristics for a typical GaN Schottky diode with area of 0.2 mm^2. The inset shows current in log scale.

Electrical measurements were performed using a SR850 digital lock-in amplifier. The lock-in drove the solenoidal tranducer through a custom bridge amplifier with flat frequency response throughout the range of 0-10 kHz. At the same time, it measured the amplitude and phase of the voltage generated by the Schottky diode in response to this mechanical excitation. As shown in Fig. 2.18, variable dc voltages were applied to the diode through a high impedance biasing network ($30M\Omega$).

To calibrate the strain conditions in the GaN epilayer, a commercial metallic strain gauge (not shown in Fig. 2.18) was affixed to the surface in the vicinity of the Schottky diode. For frequency scans, these gauges were used to correct for any amplitude or phase variability of the strain induced in the GaN epilayer. Throughout this experiment, the gauges measured strain amplitudes for S_1 in the range of $1-4\times 10^{-6}$. However, given both the relatively large size of the commercial gauges (and the notorious variability in their gauge factor), the actual strain at the Schottky contact could only be known to within a factor of 4 at best.

2.2.3 Results and Discussion

Response to Frequency and DC Bias

Fig. 2.4 shows the amplitude of the a.c. voltage output by a typical diode as a function of the mechanical drive frequency (f). Each curve corresponds to a different dc bias state of the diode but the same strain amplitude. As seen in the plot, these curves share the same functional form, differing only in vertical scale. The electromechanical response of the diode increases linearly with f for low frequencies, and then rolls off to a constant value for higher frequencies. Fig. 2.5 plots the phase of the output voltage relative to the phase of the strain in the GaN epilayer over the same frequency range. The dependence of phase on frequency shown here was found to be essentially identical for all biases below the turn-on voltage. For frequencies approaching 0 Hz, the diode output is -90° out of phase with the strain; as the frequency increases, this phase difference moves toward -180°.

In part B of this section, we present a simple model based on piezoelectric trans-

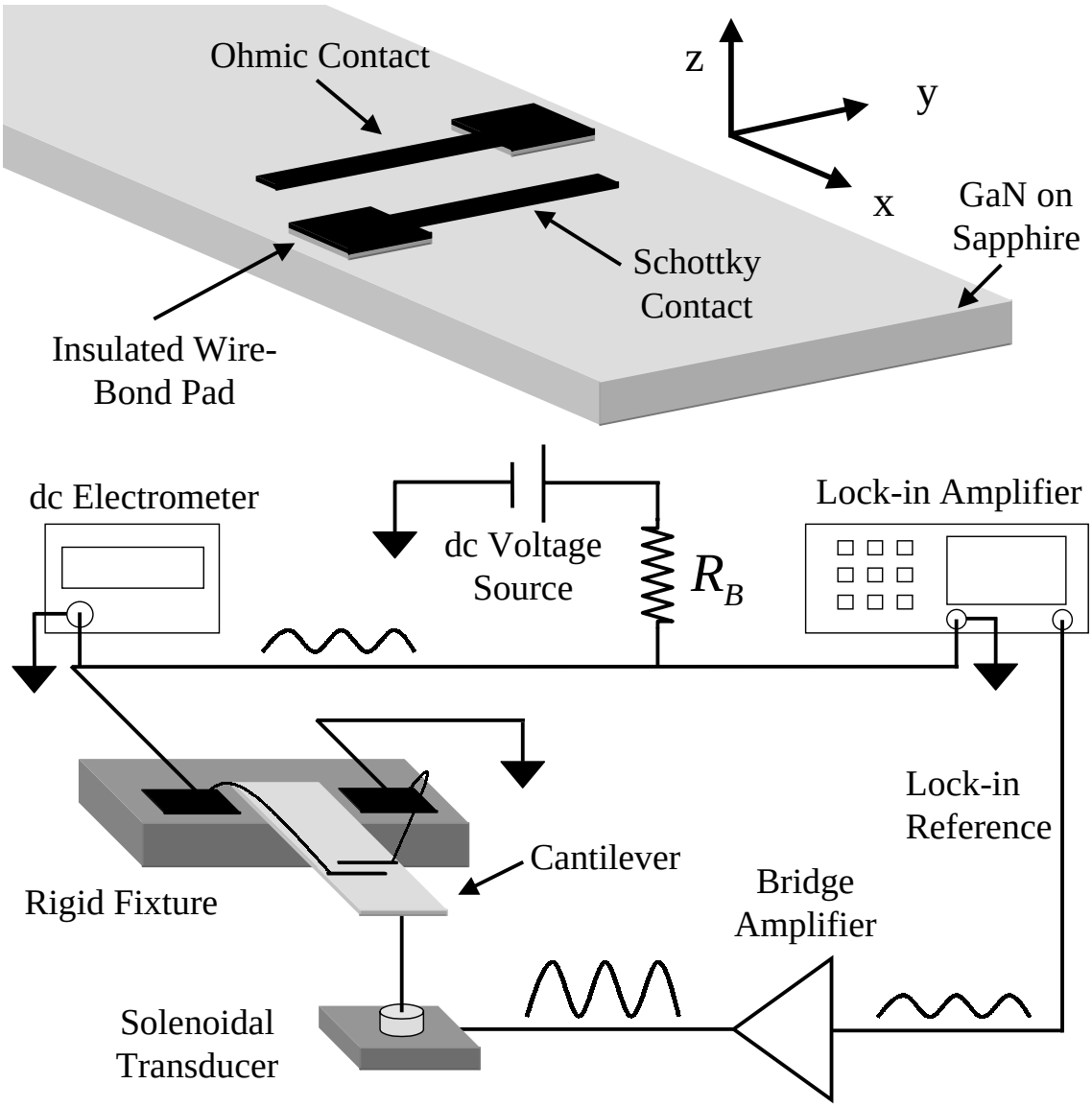

Figure 2.3: Schematic of experimental setup.

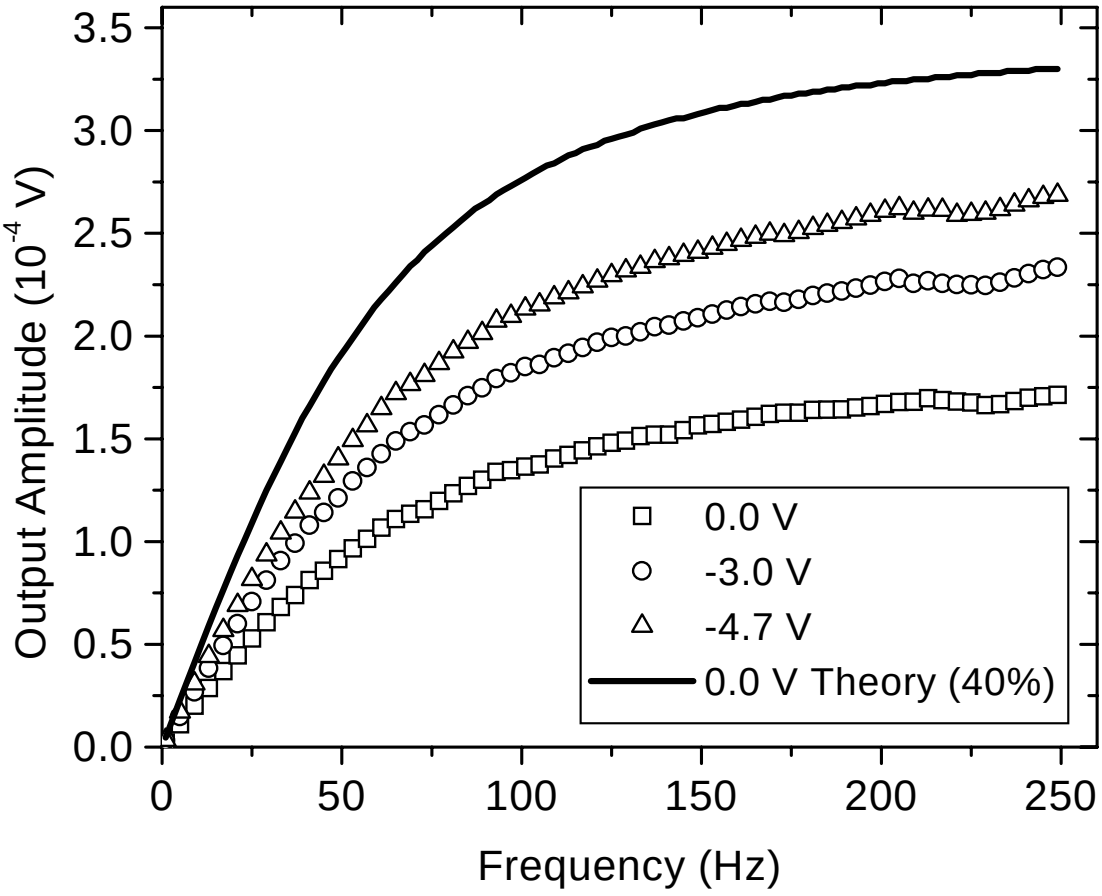

Figure 2.4: Voltage output amplitude as a function of strain frequency for several dc bias states of the Schottky diode. All curves are normalized to a strain amplitude of 1×10^{-6}. The solid line shows the model prediction for 0V bias at a reduced scale (40%).

duction to account for the frequency response data. For the moment, however, one general conclusion stands out from the experimental data: piezoresistive effects are not among the physical origins of the transduction mechanism. For one, the vanishing of the signal amplitude at low frequency confirms that no static piezoresistive activity is at work. More convincing, however, is the behavior of the phase versus frequency (Fig. 2.5): to within an overall sign, the voltage arising from a varying piezoresistance should be in-phase (0° or 180°) with the mechanical strain at low frequencies and transition to ±90° only at high frequencies where the read-out circuit becomes capacitance limited.

Further evidence of this general conclusion is furnished by the bias dependence of the electro-mechanical output, shown in Fig. 2.6 for a typical diode. For each curve, the excitation frequency was kept constant, and the amplitude of the electrical response was charted as a function of the dc bias applied to the diode. The corresponding phase data is seen in Fig. 2.7. At each frequency, the curves exhibit the same qualitative features. In forward bias, where the differential resistance of the diode becomes low, the amplitude drops off rapidly. With no external bias (0V), significant amplitude is measured, and in reverse bias, the amplitude increases almost linearly with voltage. Indeed, for all frequencies, the voltage response from the diode roughly doubles in the span of 0 to -8V. Thus, the bias applied to the diode can be used to amplify or modulate the signal coming from the strain transducer, a property which is useful for processing the sensor output.

The presence of a strong electromechanical signal with no external bias weighs in further against piezoresistivity. Theoretically, piezeoresistive sensors generate an electrical output which is proportional to the bias applied; output at 0V bias is simply forbidden. However, on the basis of Fig. 2.6, it may be tempting to argue that a combination of piezoelectric and piezoresistive effects are at play; the former would account for the response at 0V, while the latter would explain the increasing response with reverse bias. As noted earlier, these transduction mechanisms have very different phase characteristics. Therefore, with increasing reverse bias, one would expect to observe a steadily changing phase as the relative contributions of each effect changes.

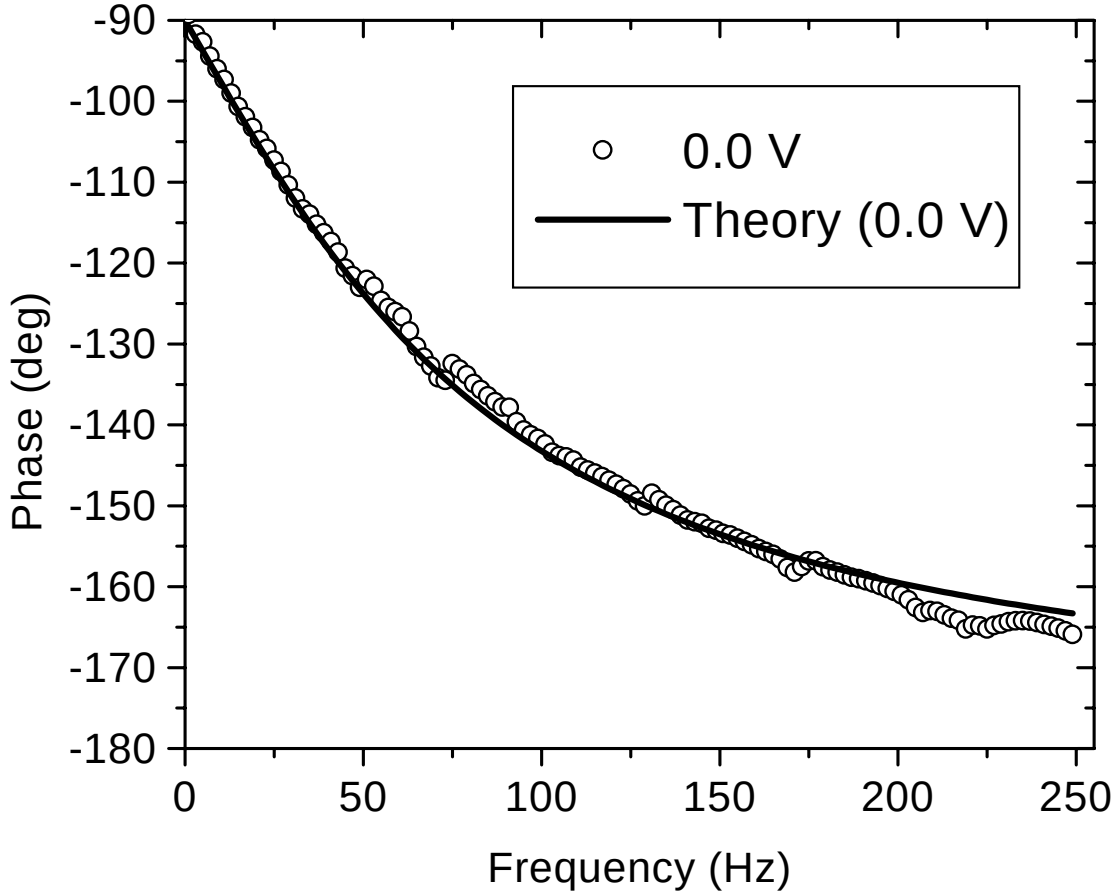

Figure 2.5: Phase of the output signal relative to the strain as a function of frequency. All reverse bias states of the diode give indistinguishable phase response. The solid line represents theory.

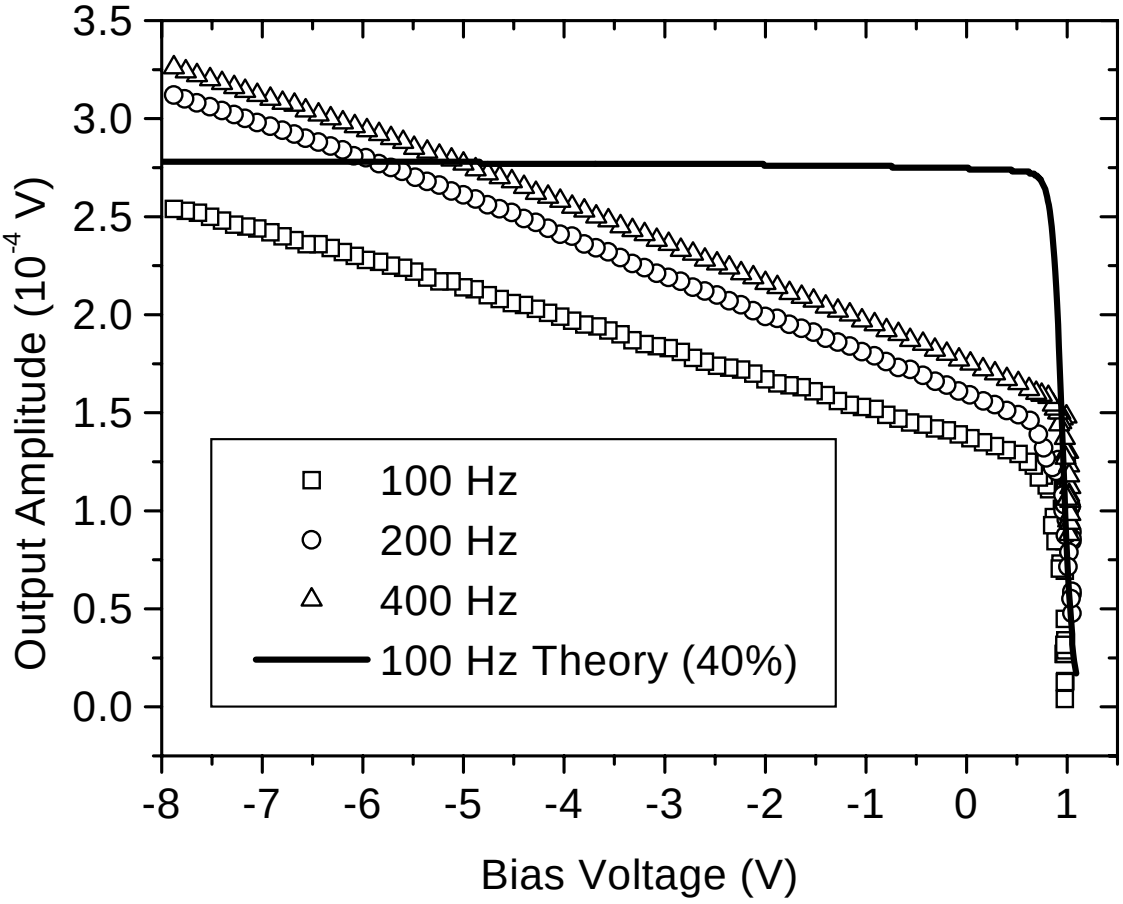

Figure 2.6: Voltage output amplitude as a function of dc bias for several strain frequencies. All curves are normalized to a strain amplitude of 1×10^{-6}. The solid line shows the model prediction for 100Hz at a reduced scale (40%).

Fig. 2.7 shows quite the contrary: at every frequency, the phase of the sensor output is essentially constant throughout the reverse bias region. Evidently, the physical cause of transduction in these diodes has the same electrical character in reverse bias as it does with no bias.

Model

The model presented here shares the same basic approach employed by Blom *et al.* [9] in their study of piezoelectric activity in metal-insulator-semiconductor (MIS) diodes on ZnO, a wide bandgap semiconductor closely related to GaN. Though these authors were concerned with the converse problem of exciting rather than detecting mechanical strain, their work laid a basis for understanding piezoelectric effects in the context of basic semiconductor device physics.

To simplify the discussion below, we make the following assumptions:

I) The strain in the GaN epilayer is uniform in the vicinity of the Schottky diode. The two nonzero components of strain have a simple harmonic time dependence of the form $S_1(t) = S_{1,0}exp(i\omega t)$ and $S_3(t) = S_{3,0}exp(i\omega t)$, where the amplitudes are related by Eqn. 2.41.

II) The ohmic contact of the diode is ideal with negligibly small contact resistance. As a result, this contact always sits at a potential equal to that of the bulk semiconductor outside the depletion region.

III) The Schottky contact is an ideal metal-semiconductor junction for which the barrier height Φ_b does not change as a result of strain.

Fig. 2.8(a) shows a cross section of the Schottky contact with the associated depletion region inside the semiconductor. The width of this depletion layer, W, and the voltage dropped across it, V, are related from standard solid-state device physics by:

$$V_{bi} - V = \frac{qN_dW^2}{2\epsilon_s} \tag{2.8}$$

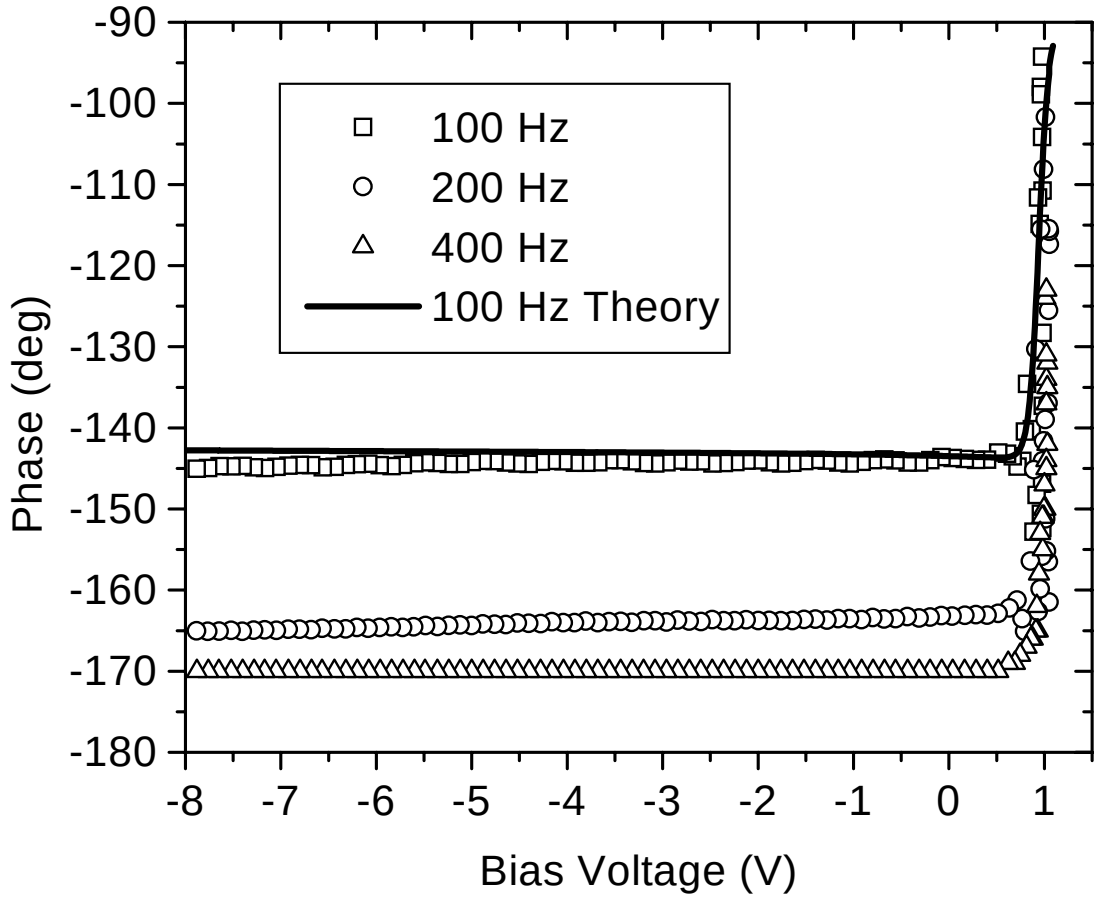

Figure 2.7: Phase of the output voltage relative to the strain as a function of dc bias for several different frequencies. The solid line shows the model prediction for 100Hz.

where N_d is the doping density, ϵ_s is the dielectric constant, and V_{bi} is the built-in voltage of the metal-semiconductor junction [10].

When the GaN film is strained, bound charge appears in the semiconductor due to the direct piezoelectric effect. Because the strain is spatially uniform, this bound charge takes the form of equal and opposite sheet charge densities on either surface of the epilayer (see Fig. 2.8(b)). For our strain conditions, the sheet charge density, σ_b, at the top surface is given by:

$$\sigma_b = e_{31}S_1 + e_{33}S_3 = \left(e_{31} - \frac{C_{31}}{C_{33}}e_{33}\right)S_1 \equiv e'_{31}S_1 \tag{2.9}$$

Here, e_{ij} refer to components of the GaN piezoelectric tensor, and e'_{31} defines an effective piezoelectric constant appropriate for our coupled strain conditions (Eqn. 2.41).

In an insulating crystal, this piezoelectric charge distribution would give rise to a uniform electric field between the surfaces. In regions of n-type GaN that are not depleted, however, free electrons will move rapidly to expel any field. When the Schottky contact is strained, free carriers move essentially instantly to screen the bound charge ($-\sigma_b$) that develops at the bottom face of the epilayer. To accomplish this screening, mobile carriers will likely either: (i) move into or out of GaN-sapphire interface states, or (ii) accumulate very close to the surface in the highly conductive layer that typically forms at this interface. If the strain does not continue to change in time, the bound charge (σ_b) at the top face of the epilayer will eventually be screened as well, in this case by a net change in free charge (of opposite sign) occupying either GaN-metal interface states or the sheet charge at the bottom surface of the metal [11]. If, however, the Schottky barrier provides infinite resistance to the flow of electrons from the bulk to the metal interface (the more realistic case is addressed below), the screening of the bound charge at the top surface will be incomplete. To conserve free charge in this case, the net flow of carriers to the bottom face must be balanced by a corresponding change in the width (W) of the depletion layer above. In effect, then, the bound charge induced at the bottom surface is passed onto the edge of the

depletion layer. For a Schottky contact of area A, this charge balance requires that:

$$-AqN_d\frac{dW}{dt} = A\frac{d\sigma_b}{dt} \equiv I_{pz} \tag{2.10}$$

where we have introduced I_{pz} to represent the current leaving the semiconductor side of the depletion layer in response to strain. For our strain conditions, this piezoelectric current will be given by:

$$I_{pz} = Ae'_{31}\frac{dS_1}{dt} = Ae'_{31}\left(i\omega S_{1,0}e^{i\omega t}\right) \tag{2.11}$$

Substitution of Eqn. 2.10 into Eqn. 2.36 allows us to solve for the time rate of change of the voltage generated across the diode as a result of the strain:

$$\frac{dV}{dt} = \frac{W}{A\epsilon_s}I_{pz} = \frac{I_{piezo}}{C_d} \tag{2.12}$$

where $C_d = A\epsilon_s/W$ is the capacitance of the Schottky diode. Note that Eqn. 2.12 gives the open-circuit response of a diode if no free charge currents can flow from one side of the Schottky barrier to the other.

In reality, of course, charge will flow across the barrier as a result of intrinsic leakage mechanisms. Furthermore, in our measurements, the diodes were connected to an external sensing circuit which provided an additional path for current flow. When strain is applied, this free current, I_{free}, will act to restore equilibrium across the diode. To account for it, we must modify Eqn. 2.10 to read:

$$-AqN_d\frac{dW}{dt} = I_{pz} - I_{free} \tag{2.13}$$

The free current from the metal to the semiconductor side of the diode is determined by the voltage across the diode and the effective impedance Z of all the conduction paths: $I_{free} = V/Z$. With this impedance known, Eqns. 2.13 and 2.36 can be combined to determine the voltage generated by strain.

Fig. 2.8(c) shows the circuit conditions relevant to our measurements. Here, the

intrinsic capacitance and differential resistance of the Schottky diode are represented by C_d and R_d respectively. Note that both of these parameters depend on the dc bias applied to the diode. The external measurement circuit is composed of R_b, the resistance from the biasing network, and C_s, the stray capacitance of the test fixture. Using elementary circuit analysis to find the impedance, we can then solve for the small-signal a.c. voltage generated by the diode as a result of excitation at frequency ω:

$$V(t;\omega) = \left[\frac{i\omega R'}{1 + i\omega R'C'}\right] A e'_{31} S_{1,0} e^{i\omega t} \tag{2.14}$$

Here, R' and C' are the effective parallel resitance and capacitance of the network:

$$C' = C_d + C_s \quad 1/R' = 1/R_d + 1/R_b \tag{2.15}$$

Note that $V(t;\omega)$ is exactly the voltage that would result from a current source I_{pz} connected in parallel with the Schottky diode (as shown in Fig. 2.8(c)). In this model, then, all piezoelectric activity inside the Schottky diode is electrically equivalent to an external parallel current source of magnitude given by Eqn. 2.11.

Theoretical plots of Eqn. 2.14 are shown in Figs. 2.4 through 2.7 for comparison with the experimental data. To calculate I_{pz} for these curves, we used material constants for GaN quoted in the literature: $e_{31} = -0.44$, $e_{33} = 0.86$ C/m^2 and $C_{31}/C_{33} = 0.20$ [12]. These constants yield an effective piezoelectric constant of $e'_{31} = -0.61\, C/m^2$. The strain, as mentioned earlier, was measured by the commercial micro-gauges. All other parameters appearing in Eqn. 2.14, including the capacitance-voltage (C-V) characteristics of the diode, were measured independently using an impedance analyzer. As a consequence, these theoretical curves contain no free parameters that could be tuned to fit the data.

As seen in Fig. 2.5, the model matches almost exactly the observed frequency dependence of the phase. Accordingly, since e'_{31} is negative, the overall sign of the measured voltage output is consistent with piezoelectric activity. In addition, the model predicts the correct functional form of the corresponding amplitude data as shown in Fig. 2.4. Note that the overall vertical scale of the theoretical amplitude

curve agrees with measurement to within the experimental uncertainty of our strain calibration. Given the congruence of theory and experiment, the model can be used to understand the qualitative features of the frequency response data. At 0 Hz, the diode output vanishes because the piezoelectric current I_{pz} drops out for static strain. For low frequencies, Eqn. 2.14 can be approximated by:

$$V(t;\omega) \approx -i\omega R' A |e'_{31}| S_{1,0} e^{i\omega t} \tag{2.16}$$

In this regime, the voltage amplitude from the diode increases linearly with ω, while the phase is $-90°$. As the strain frequency rises, the diode output becomes increasingly dominated by capacitance. Ultimately, for large ω, the voltage takes on the limiting form:

$$V(t;\omega) \approx -\left[\frac{1}{C_s + C_d}\right] A |e'_{31}| S_{1,0} e^{i\omega t} \tag{2.17}$$

Here, the voltage is $-180°$ out of phase with the strain and its amplitude is flat in frequency.

For the dependence of output amplitude on bias, Fig. 2.6 shows a comparison between theory and experiment. In forward bias, the model captures the observed roll off in amplitude brought on by the rapidly decreasing differential resistance (R_d) of the diode. In the framework of our model, a small R_d acts as a low impedance shunt for the piezoelectric current, causing the output voltage to drop. In reverse bias, however, serious discrepancies appear: while the theoretical response saturates, the experimental curves continue to rise with reverse bias. On the basis of Eqn. 2.17, one might expect the theoretical amplitude to increase in reverse bias as the diode capacitance C_d falls. However, for our experimental setup, this change in C_d is swamped by the much larger fixed capacitance of the test fixture C_s.

The divergence of experiment and theory in reverse bias may point to invalid assumptions in our model. Alternately, it may be the result of effects with a different physical origin that were not included. As discussed before, piezoresistive activity is ruled out. A time-varying capacitance in our circuit, whether in the test fixture or the diode itself, would generate a voltage by the same means exploited in a common

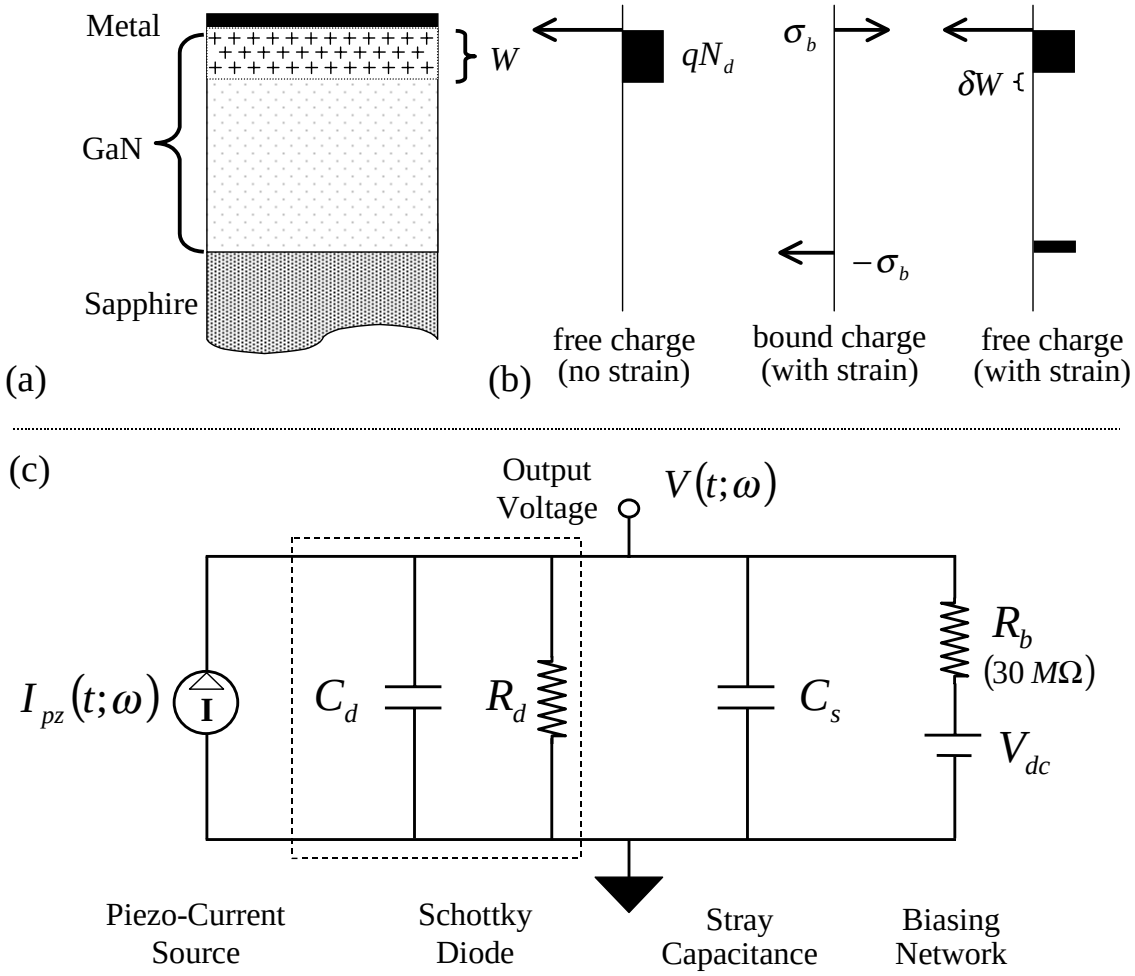

Figure 2.8: (a) Cross section of the Schottky diode showing the depletion region. (b) Schematic diagram of bound and free charge densities depending on strain. (c) Equivalent circuit for diode and connected measurement network.

condenser microphone. This voltage would exhibit roughly the correct frequency and bias behavior, but our estimates suggest that its magnitude is likely too small to contribute significantly.

Based on preliminary response data from other GaN devices, we have reason to suspect that the rising amplitude in reverse bias can be attributed to an additive signal generated by the insulated contact pad which was connected directly to the Schottky contact. In effect, this pad forms a MIS diode having its own unique response characteristics. In fact, for these devices, the output amplitude is expected to depend strongly on the bias state. One important consequence of this dependence is that an ac voltage applied to the diode could be used to modulate the electromechanical output signal. From a practical perspective, intrinsic signal mixing of this sort enhances the functionality of these transducers. Among other applications, it would provide a convenient means to discriminate the response signal from the drive signal in a micro-mechanical resonator.

Signal-to-Noise Ratio

To determine the sensitivity of GaN Schottky diodes for strain detection, we measured the voltage noise appearing across these devices as a function of frequency and bias. The noise measurements were performed using identically the same read-out circuit employed in our earlier studies. Because of dynamic range limitations in the lock-in amplifier, the noise was measured without straining the samples.

Fig. 2.9 shows the voltage noise power spectral density $\langle V_n^2 \rangle$ for a typical diode with no external bias. For low frequencies, the noise power converges to the fundamental Johnson noise limit of the effective resistance of our circuit. At 0 V bias, this resistance R' is essentially that of the bias resistor $R_b = 30M\Omega$. At high frequencies, the spectral density bottoms out at the noise floor of the lock-in amplifier. In the intervening range of frequencies, it rolls off exactly as expected for a Johnson noise voltage source shunted by a capacitance C', namely:

$$\langle V_n^2 \rangle = \left[\frac{4kTR'}{1 + (\omega R'C')^2} \right] \tag{2.18}$$

Overlaid on the data in Fig. 2.9 is a plot of Eqn. 2.18 wherein we have added the noise floor of the lock-in amplifier.

For no applied bias, then, we can calculate the signal-to-noise ratio (SNR) for strain detection by dividing the signal, Eqn. 2.14, by the noise, Eqn. 2.18. The result, valid for high (capacitance-limited) frequencies, and neglecting the additive noise of any external amplification stages, is given by:

$$SNR(\omega) = |e_{31}|AS_0\omega\sqrt{\frac{R'}{4kTB}} \tag{2.19}$$

where B is the measurement bandwidth and S_0 is the strain amplitude. With an optimally designed read-out circuit, the upper limit for R' in Eqn. 2.19 is R_d, the intrinsic leakage resistance of the diode. In this case, for the devices tested here, the fundamental strain detection sensitivity at room temperature is:

$$SNR(\omega) = \left(4.8 \times 10^8/\sqrt{Hz}\right)\frac{S_0\omega}{\sqrt{B}} \tag{2.20}$$

Note that the signal-to-noise ratio in Eqns. 2.19 and 2.20 does not depend upon C': the net capacitance of the circuit attenuates the piezoelectric signal and the noise equally. Furthermore, the SNR rises linearly with ω; this is in contrast to piezoresistive sensors, for example, for which the SNR does not improve with frequency.

As shown earlier, the electromechanical signal from the diode can be amplified by applying a reverse bias. Fig. 2.10 shows the effect of this bias on the noise power spectral density. As seen in the figure, the noise power rises sharply with the onset of current flow in forward bias. In reverse bias, for frequencies above $\sim$ 100 Hz, it remains at the Johnson noise limit throughout the range of biases shown. Thus, in this regime, the sensitivity of the diode will improve with reverse bias. For lower frequencies, however, an excess noise source becomes increasingly dominant as the diode leakage current grows. After comparing with the I-V characteristics of the diode, we find that this excess noise power scales roughly like I^2/f^3, where I is the reverse leakage current. This scaling is consistent with the effects of standard $1/f$

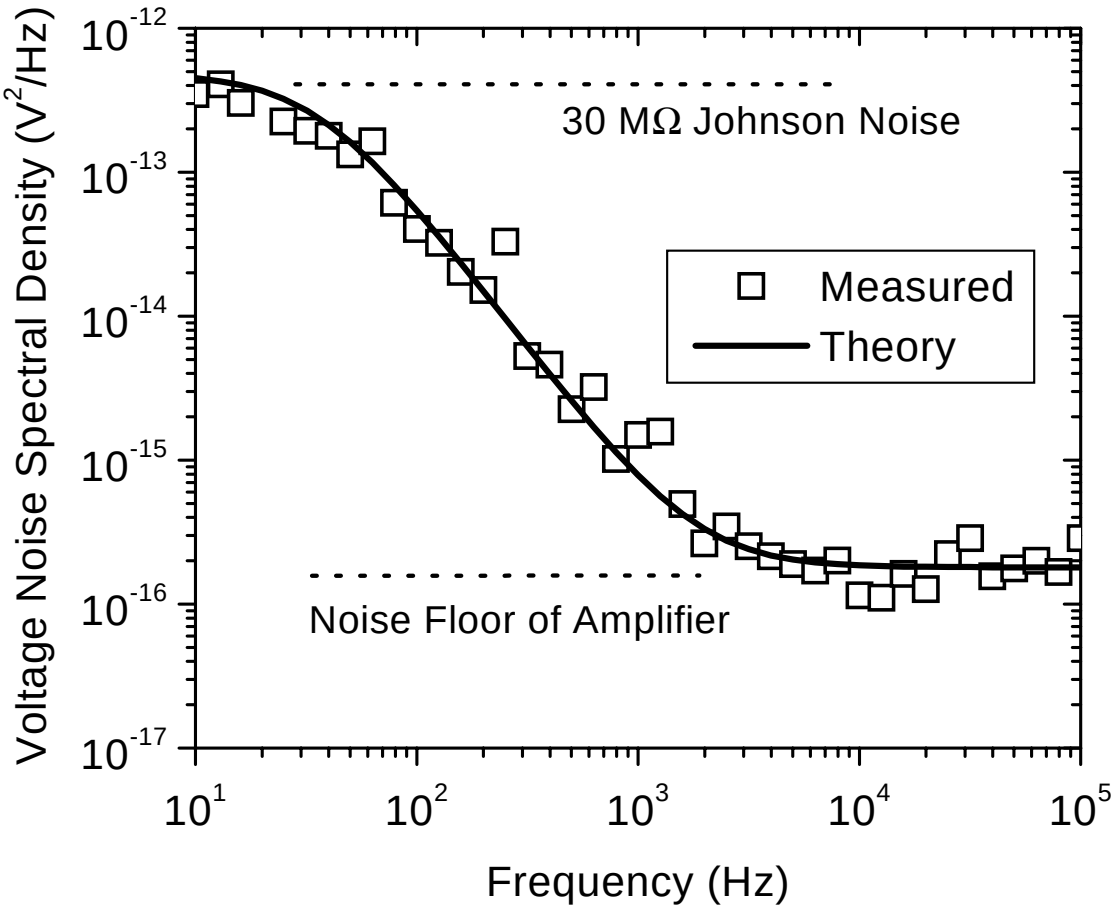

Figure 2.9: Voltage noise power spectral density versus frequency for 0V applied bias. The solid line shows a theoretical fit including the noise floor of the amplifier.

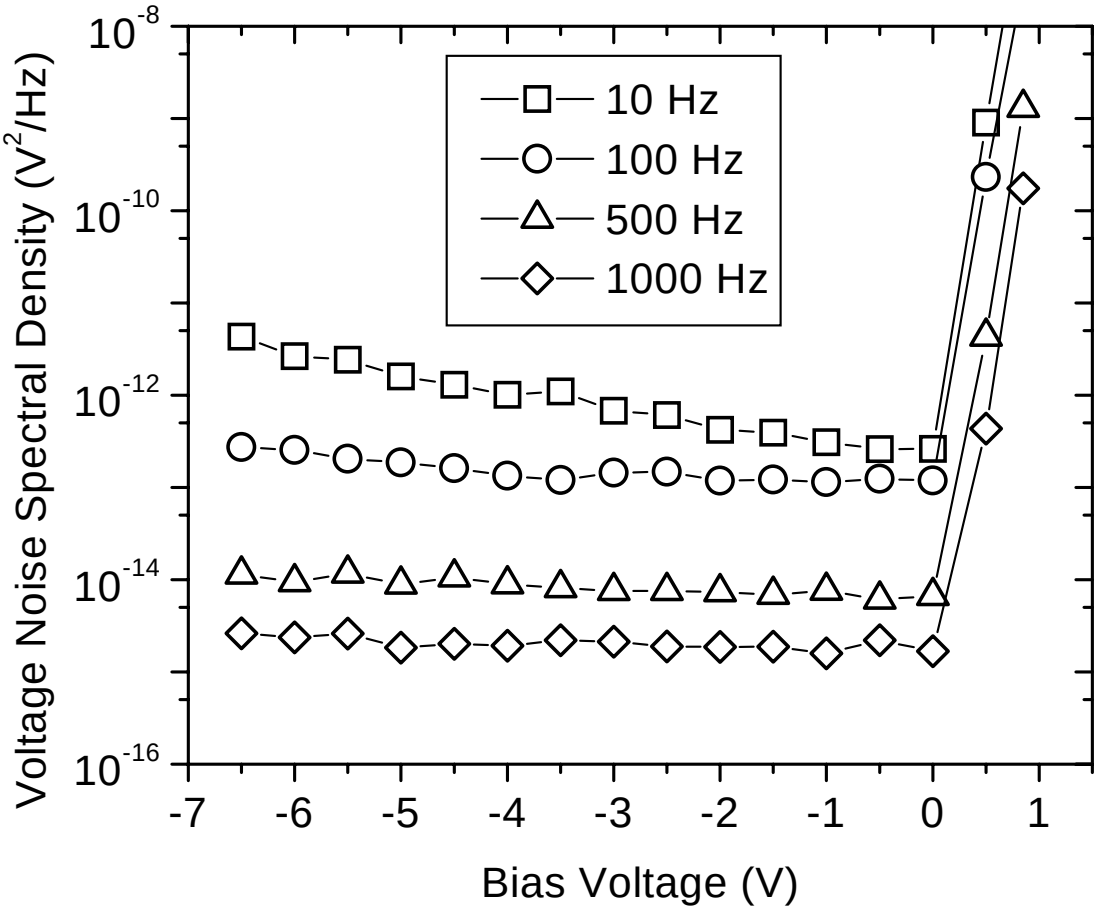

Figure 2.10: Voltage noise power spectral density versus applied bias for various frequencies.

fluctuations of the diode resistance in the context of our measurement circuit [13]. As a result, for frequencies less than $\sim$ 100 Hz, the SNR will be optimum at a bias close to 0 V. However, present and future advances in device design will no doubt achieve a dramatic reduction in the leakage current; these advances will extend the useable range of reverse bias even for very low strain frequencies.

2.2.4 Conclusions

In summary, we have studied the electromechanical response of Schottky diodes on n-GaN as a function of frequency and dc bias. The frequency response data from these diodes can be explained using a simple model of piezoelectric charge generation across the depletion layer. An unexpected rise of the output amplitude with reverse bias can be used to amplify or modulate the electromechanical signal. For frequencies starting around 10 Hz, these diodes demonstrated excellent strain detection sensitivity. Since transduction arises through the piezoelectric effect, these devices do not require external biasing for operation. Owing to their ease of fabrication, GaN Schottky diodes can be readily integrated into MEMS based elements for strain sensing or actuation.

Bibliography

[1] R. Beach and T. McGill, Journal of Vacuum Science and Technology B **17**, 1753 (1999).

[2] S. Nakamura, M. Senoh, N. Iwasa, S. Nagahama, T. Yamada, and T. Mukai, Jpn. J. Appl. Phys. **34**, L1332 (1995).

[3] R. Strittmatter, R. Beach, and T. McGill, Applied Physics Letters **78**, 3226 (2001).

[4] R. Gaska, M. Shur, A. Bykhovski, J. Yang, M. Khan, V. Kaminski, and S. Soloviov, Appl. Phys. Lett **76**, 3956 (2000).

[5] A. Bykhovski, V. Kaminski, M. Shur, Q. Chen, and M. Khan, Appl. Phys. Lett **68**, 818 (1996).

[6] R. Gaska, J. Yang, A. Bykhovski, M. Shur, V. Kaminskii, and S. Soloviov, Appl. Phys. Lett **71**, 3817 (1997).

[7] R. Gaska, A. Bykhovski, M. Shur, V. Kaminskii, and S. Soloviov, Journal of Applied Physics **85**, 6932 (1999).

[8] J. Nye, *Physical Properties of Crystals*, 2nd ed. (Oxford University Press, New York, NY, USA, 1985).

[9] F. Blom, D. Yntema, F. Van de Pol, M. Elwenspoek, J. Fluitman, and T. Popma, Sensors and Actuators A **A21**, 226 (1990).

[10] S. Sze, *Physics of Semiconductor Devices*, 2nd ed. (John Wiley & Sons, Inc., New York, NY, USA, 1981).

[11] The exact nature of the screening of the piezoelectric surface charge, whether by charge in interface states or on the metal surface, can have a noticeable

impact on the final equilibrium barrier height of the Schottky diode. This arises because a potential can develop across the very thin surface dipole layer between the semiconductor and metal. The resulting shift in barrier height has in fact been observed in GaAs Schottky diodes [14]. Given that the thickness of the dipole layer is on the order of angstroms, and given the known magnitude of the piezoelectric charge induced by the strain in our experiment, the maximum voltage that could develop across the Schottky diode as a result of this dipole layer is far too small to account for the electro-mechanical voltage levels observed.

[12] A. Zoroddu, F. Bernardini, P. Ruggerone, and V. Fiorentini, Physical Review B **64**, 1 (2001).

[13] P. H. Handel, Physical Review A **22**, 745 (1978).

[14] K. W. Chung, Z. Wang, J. Costa, F. Williamson, P. Ruden, and M. Nathan, Applied Physics Letters **59**, 1191 (1991).

2.3 Metal-Insulator-Semiconductor Diodes

2.3.1 Introduction

In the preceding section, GaN Schottky diodes were shown to make sensitive piezoelectric sensors. The critical factor in their operation was the electrostatic barrier of the depletion layer which blocked free charge from negating bound charge. The measured output of these sensors agreed well with the model, except for an unexpected rise in the amplitude with increasing reverse bias. At that time, it was speculated that this behavior was spurious, perhaps resulting from an additive source in the insulated contact pads adjacent to the diodes.

To explore this possibility, a study of the electromechanical response of metal-insulator-semiconductor (MIS) diodes was undertaken. Here, special steps were taken to wire-bond directly to the diode gates in order to avoid any contamination from stray sources on the GaN surface. As strain sensors, these devices proved to be well worth study of their own right. Not only do they offer near infinite leakage resistance, but they can be biased much further into reverse without breakdown. As discussed shortly, both of these properties lead to an enhancement in the sensitivity to detect strain.

The following section presents measurements of the electromechanical response of high-quality MIS diodes formed on n-GaN with SiO_2. By modifying the piezoelectric model to account for the distinct device physics of a MIS capacitor, near-perfect agreement with the data is obtained. Furthermore, the output versus bias characteristics strongly suggest that these devices contaminated earlier results for the Schottky diodes. The first part of this section describes the experimental steps used to fabricate the MIS diodes and connect to them directly. In the following part, a model is developed and compared to the data. Finally, the strong relationship between output and bias is exploited to effect nonlinear mixing of the strain signal with a modulation signal applied to the gate. Mixing in this way could be used for low-noise parametric amplification within the sensor itself.

2.3.2 Experimental Setup

The GaN sample used in this experiment was grown by metalorganic chemical vapor deposition (MOCVD) on a c-plane sapphire substrate. The growth consists of three epitaxial layers: (i) a 40 nm AlN buffer layer; (ii) a 5.0 μm n^+-GaN base layer which was doped with Si at a level of $5 \times 10^{18}/cm^3$; and (iii) a 3.0 μm n-GaN surface layer lowly doped at $7 \times 10^{16}/cm^3$. The growth resulted in Ga-polar (0001) film with a sheet resistance of 40 Ω/square.

To form the MIS diodes, a 90 nm SiO_2 layer was deposited on the GaN surface by plasma-enhanced chemical vapor deposition (PECVD) at a temperature of 350 $^\circ$C. A 100 nm Al layer was then sputter deposited on the insulator and subsequently patterned into 390 μm diameter circular gate electrodes by etching down in phosphoric acid. The ohmic contacts, consisting of an Al-Ni-Au (50 nm-30 nm-50 nm) stack, were sputter deposited on the GaN surface in windows etched out of the insulator layer using hydro-flouric acid. These contacts were ohmic as deposited.

The room temperature capacitance-voltage (C-V) characteristics of a typical MIS diode are shown in Fig. 2.11. The forward and reverse sweeps shown here were measured in the dark at a frequency of 100 kHz and a voltage sweep rate of 10 mV/s. The solid line shows a theoretical fit to the data using the exact solution for the high-frequency capacitance of an ideal MIS diode without interface states [1]. Due to the prohibitively low minority carrier generation rate in GaN at room temperature [2], this analytical solution was modified to exclude the effect of any minority carrier holes. As a result, the capacitance exhibits a deep depletion characteristic for large reverse biases. The fit shown corresponds to a flat band voltage of $V_{fb} = 12.0$ V and an oxide dielectric constant of $\epsilon_i = 3.5\ \epsilon_0$. A discussion of the surface state density at the GaN/SiO_2 interface is deferred until the next section, where MIS diodes are used to measure static strain conditions. Given the large time constants for emission from surface states, these traps will not significantly effect the performance of these diodes when operated as ac strain sensors.

To study the effects of strain on these MIS diodes, the setup discussed in the

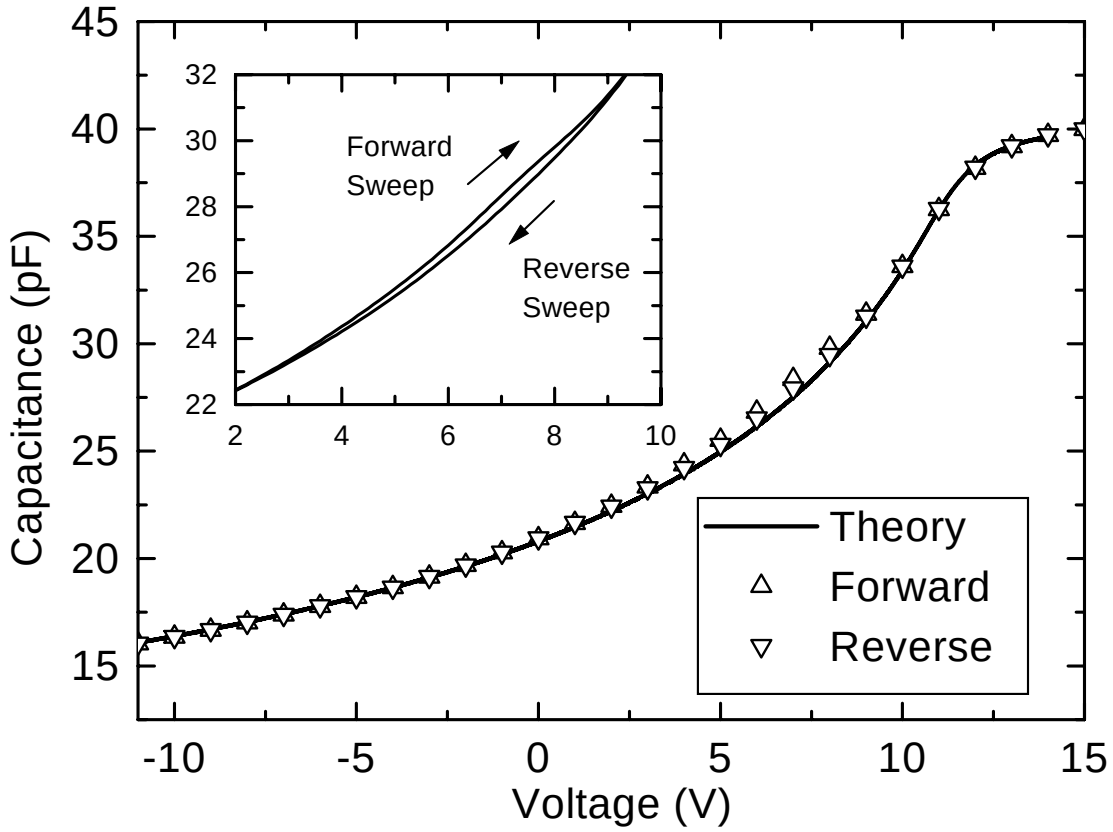

Figure 2.11: Room-temperature C-V characteristics for a 0.12 mm^2 GaN MIS diode showing both forward and reverse sweeps. The data was taken at a ramp rate of .01 V/s and a spot frequency of 100 kHz. The solid line represents a theoretical fit for an ideal diode. The inset shows an expanded view of a small hysteresis likely caused by interface states.

previous section was employed. The GaN samples, with dimensions $5 \times 30\ mm$, were anchored at one end to a rigid support fixture to form a suspended cantilever. A wire, affixed at the free end of the cantilever, conveyed a mechanical line force to the sample from a solenoidal transducer below. As before, the resulting deformation of the GaN epilayer is a mixture of longitudinal strain in x (S_1) and in z (S_3). Using standard reduced notation [3], these components of strain are related by:

$$S_3 = -\frac{C_{31}}{C_{33}} S_1 \tag{2.21}$$

where C_{ij} are the components of the GaN elastic tensor. Given the relative thickness of the GaN epilayer ($8\ \mu m$) to the sapphire substrate ($400\ \mu m$), these strain conditions are approximately uniform in z across the film thickness, but vary in x along the length of the cantilever.

To prevent any spurious electro-mechanical signal arising from contact pads, the circular gate of the MIS diode was wire bonded to directly. Since the force of the wire bonding process would compromise the thin SiO_2 dielectric layer, the gold wire was positioned using micro-probes and adhered with a conductive epoxy. As before, electrical measurements were performed using a SR850 digital lock-in amplifier. The lock-in drove the solenoidal transducer through a custom bridge amplifier with flat frequency response throughout the range of 0 - 10 kHz. At the same time, it measured the amplitude and phase of the voltage generated by the MIS diode in response to this mechanical excitation. Variable dc voltages were applied to the diode through the same high impedance biasing network.

2.3.3 Results and Discussion

Model

In the analysis to follow, we will make the following assumptions:

I) The strain in the GaN epilayer is uniform in the vicinity of the MIS diode. The two nonzero components of strain have a simple harmonic time

dependence of the form $S_1(t) = S_{1,0}exp(i\omega t)$ and $S_3(t) = S_{3,0}exp(i\omega t)$, where the amplitudes are related by Eqn. 2.21.

II) The ohmic contact of the diode is ideal with negligibly small contact resistance. As a result, this contact always sits at a potential equal to that of the bulk semiconductor outside the depletion region.

III) The MIS contact is an ideal metal-insulator-semiconductor junction without either bulk charges in the insulator or surface trap states at the semiconductor-insulator interface.

As discussed before, when the GaN film is strained, bound charge appears in the semiconductor due to the direct piezoelectric effect. Because the strain is spatially uniform, this bound charge takes the form of equal and opposite sheet charge densities on either surface of the epilayer (see Fig. 2.8(b)). For our strain conditions, the bound sheet charge density, σ_b, at the top surface is given by:

$$\sigma_b = e_{31}S_1 + e_{33}S_3 = \left(e_{31} - \frac{C_{31}}{C_{33}}e_{33}\right)S_1 \equiv e'_{31}S_1 \tag{2.22}$$

Here, e_{ij} refer to components of the GaN piezoelectric tensor, and e'_{31} defines an effective piezoelectric constant appropriate for our coupled strain conditions (Eqn. 2.21).

Of course, a bound sheet charge of opposite sign will be generated at the bottom (GaN/sapphire) interface as well. We will assume that this bound charge is screened by free charge carriers in the semiconductor on a time scale which is effectively immediate in comparison to the strain frequency. As a result, the bulk of the GaN, away from the depletion region at the MIS junction, will always remain field free and thus at a potential equal to that at the ohmic contact. The validity of this assumption will break down when the strain frequency approaches the dielectric relaxation frequency of the semiconductor, $f_d = \sigma_s/\epsilon_s$ where σ_s is the conductivity of the semiconductor. In our case, this frequency is on the order of $f_d \approx 5$ MHz, well above the strain frequencies applied in this experiment.

Since the bound sheet charge at the bottom interface is screened by an equal and opposite free charge in the semiconductor, the charges (both bound and free) in the MIS junction must satisfy the following relation to preserve overall charge neutrality:

$$\sigma_m + Q_s + \sigma_b = 0 \tag{2.23}$$

where σ_m is the free sheet charge density on the metal gate, σ_b is the piezoelectric bound charge at the GaN/oxide interface, and Q_s is the integrated total free charge per unit area within the semiconductor depletion region. As a result of Eqn. 2.23, and the assumption discussed above, the voltage V across the MIS diode is completely determined by the interfacial bound and semiconductor free charges:

$$V = F(Q_s, \sigma_b) \tag{2.24}$$

where F is some function that we will determine below.

For an ideal MIS diode biased into depletion, the relationship between the depletion width W and the voltage V across the terminals is given by:

$$V_{bi} - V = \frac{qN_dW^2}{2\epsilon_s} + \frac{qN_dz_iW}{\epsilon_i} \tag{2.25}$$

where z_i is the oxide thickness, ϵ_i is the dielectric constant of the oxide, N_d is the doping density, ϵ_s is the semiconductor dielectric constant, and V_{bi} is the built-in voltage of the MIS junction. Since the integrated charge density in the depletion region is simply $Q_s = qN_dW$, Eqn. 2.25 can be recast as:

$$V_{bi} - V = \frac{{Q_s}^2}{2qN_d\epsilon_s} + \frac{z_iQ_s}{\epsilon_i} \tag{2.26}$$

When the junction is strained, a piezoelectric sheet charge σ_b appears at the GaN/oxide interface. Assuming free carriers in the semiconductor relax as described above to preserve overall charge neutrality in the junction region (Eqn. 2.23), the

relation between the voltage and the relevant charge densities will become:

$$V_{bi} - V = \frac{{Q_s}^2}{2qN_d\epsilon_s} + \frac{z_i}{\epsilon_i}\left(Q_s + \sigma_b\right) \tag{2.27}$$

Taking the time derivative of both sides of Eqn. 2.27 yields:

$$-\frac{dV}{dt} = \frac{Q_s}{qN_d\epsilon_s}\frac{dQ_s}{dt} + \frac{z_i}{\epsilon_i}\left(\frac{dQ_s}{dt} + \frac{d\sigma_b}{dt}\right) \tag{2.28}$$

Eqn. 2.28 is the starting point for analyzing the small signal ac voltage response of the MIS diode. To solve for this voltage, a relation between semiconductor charge Q_s and the piezoelectric surface charge σ_b must be specified. If the terminals of the diode are in an open circuit configuration, there is no path for free charge to flow from the metal gate to the semiconductor below. In this case, the free charge on the metal is constant ($d\sigma_m/dt = 0$), and therefore to satisfy charge neutrality (Eqn. 2.23), the following must hold:

$$\frac{dQ_s}{dt} = -\frac{d\sigma_b}{dt} \tag{2.29}$$

Combining Eqns. 2.29 and 2.28 yields the small signal open circuit voltage across the MIS capacitor in response to strain:

$$\frac{dV}{dt} = \frac{Q_s}{qN_d\epsilon_s}\frac{d\sigma_b}{dt} = \frac{1}{c_d}\frac{d\sigma_b}{dt} = \frac{1}{c_d}e'_{31}\frac{dS_1}{dt} \tag{2.30}$$

where we have introduced c_d to denote the diode capacitance per unit gate area and exploited Eqn. 2.22 in the last step.

Practically speaking, any external circuit which attempts to measure the voltage across the diode will introduce paths for the flow of free charge from the gate to the semiconductor below. If we let Z denote the effective impedance of these parallel paths at the strain frequency of interest, the time rate of change of charge on the gate metal will now be governed by:

$$A\frac{d\sigma_m}{dt} = -\frac{V}{Z} \tag{2.31}$$

where A is the gate area. Since this free current is no longer zero, the charge neutrality condition (Eqn. 2.29) must be modified to read:

$$A\frac{dQ_s}{dt} = \frac{V}{Z} - A\frac{d\sigma_b}{dt} \tag{2.32}$$

Substitution of Eqn. 2.32 into Eqn. 2.28, and using small signal harmonic analysis, gives the closed circuit voltage response of the MIS diode:

$$V\left(i\omega + \frac{1}{ZAc_d}\right) = i\omega\frac{1}{c_s}e'_{31}S_1 \tag{2.33}$$

where we have introduced the semiconductor capacitance per unit area $c_s = \epsilon_s/W = \epsilon_s q N_d/Q_s$. Though our analysis thus far has assumed the diode is biased into depletion, the overall diode capacitance can always be viewed as a series combination of a semiconductor and an oxide capacitance:

$$\frac{1}{c_d} \equiv \frac{1}{c_s} + \frac{1}{c_i} \tag{2.34}$$

where $c_i = \epsilon_i/z_i$ is the oxide capacitance per unit area. With this more general definition of c_s, Eqn. 2.33 is valid not only when the diode is biased into depletion, but for accumulation as well.

Comparison with Data

To facilitate the circuit analysis of the MIS diode under strain, it is convenient to recast our expression for the closed circuit voltage (Eqn. 2.33) in terms of extensive circuit parameters:

$$V = iA\omega e'_{31}S_1\frac{C_d}{C_s}\left(i\omega C_d + \frac{1}{Z}\right)^{-1} \tag{2.35}$$

where $C_d = Ac_d$ and $C_s = Ac_s$ represent the total diode and semiconductor capacitance, respectively. The electo-mechanical voltage expressed in Eqn. 2.35, which we derived by modeling the device physics of the MIS diode, is exactly the voltage which would arise from the equivalent circuit shown in Fig. 2.12(c). Depicted there is a

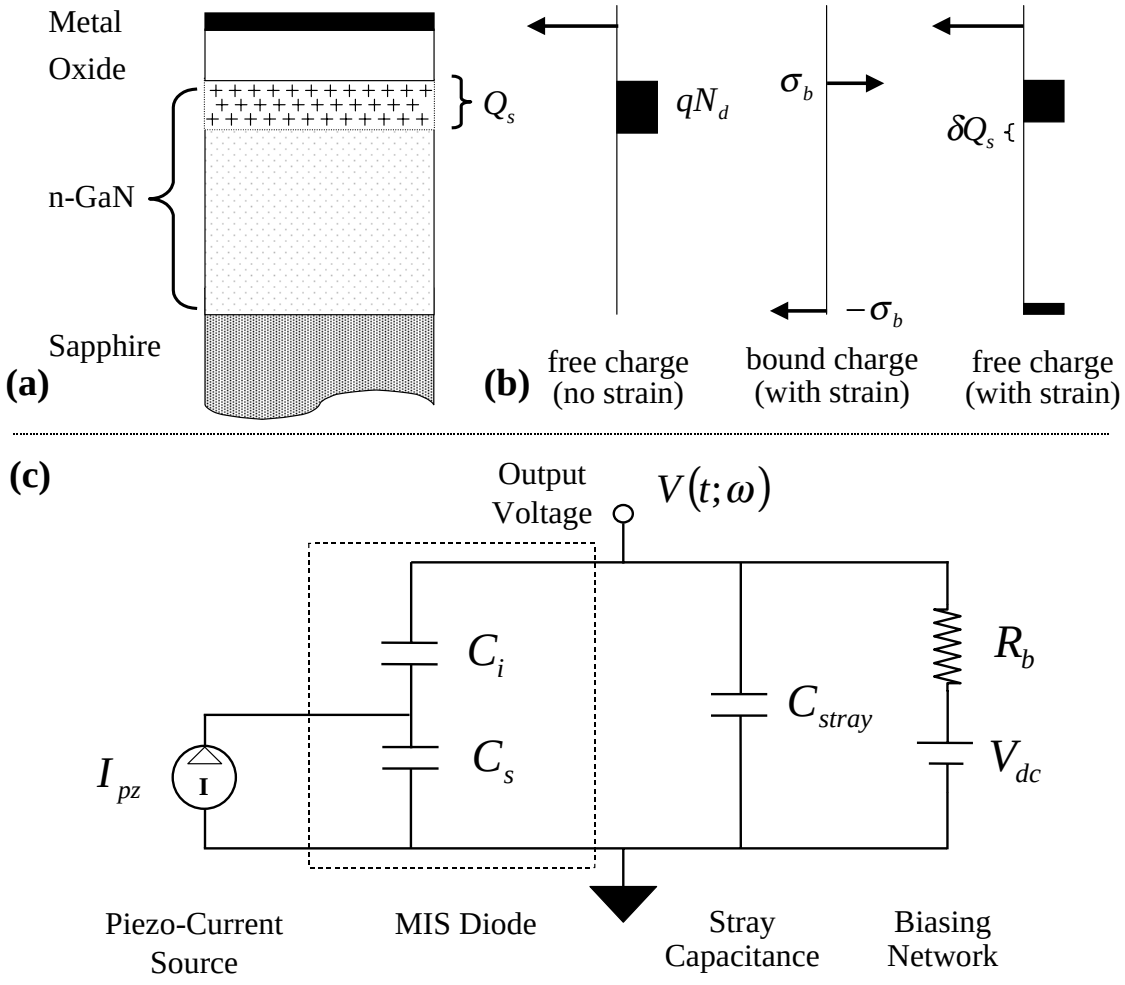

Figure 2.12: (a) Cross section of a GaN MIS diode showing the semiconductor depletion layer; (b) Schematic diagram of free and bound charge densities in the MIS diode depending on strain; (c) Equivalent circuit for the MIS diode under sinusoidal strain with external measurement circuit.

piezoelectric current source I_{pz} connected across the semiconductor capacitance C_s of the series pair comprising the MIS junction. For consistency with the derivation above, the complex amplitude of this current must be given by:

$$I_{pz} = i\omega e'_{31} S_1 \tag{2.36}$$

Also seen in Fig. 2.12(c) are two parallel paths for current flow which characterize our measurement conditions: (i) the resistance R_b of the dc biasing network, and (ii) the unavoidable stray capacitance C_{stray} to ground of the test fixture. Solving for the net impedance Z of these parallel paths and substituting into Eqn. 2.35 yields an expression for the electro-mechanical voltage which can be directly compared with experimental data:

$$V = \frac{C_d}{C_s} \left(\frac{R_b}{1 + i\omega R_b (C_d + C_{stray})} \right) iA\omega e'_{31} S_1 \tag{2.37}$$

Note the similarity of this result with that obtained for the Schottky diode in the previous section:

$$V(t;\omega) = \left[\frac{i\omega R'}{1 + i\omega R'(C_d + C_{stray})} \right] Ae'_{31} S_1 \tag{2.38}$$

The essential difference in the electro-mechanical response between these two diodes is expressed in the leading term of Eqn. 2.37. As we shall see shortly, this term is responsible for an increasing output amplitude as the MIS diode is driven further into reverse bias, even for a read-out circuit dominated by stray capacitance.

Fig. 2.13 shows the scaled measured output amplitude of the MIS diode as a function of gate bias for three different strain frequencies. The solid line, which closely fits each experimental curve, corresponds to the prediction of theory for each frequency using Eqn. 2.37. To produce these theoretical curves, we used material constants for GaN quoted in the literature: $e_{31} = -0.44$, $e_{33} = 0.86\, C/m^2$ and $C_{31}/C_{33} = 0.20$ [4]; these constants yield an effective piezoelectric constant of $e'_{31} = -0.61\, C/m^2$. The bias resistance and stray capacitance were measured independently, while the voltage-dependent capacitances related to the diode itself were calculated

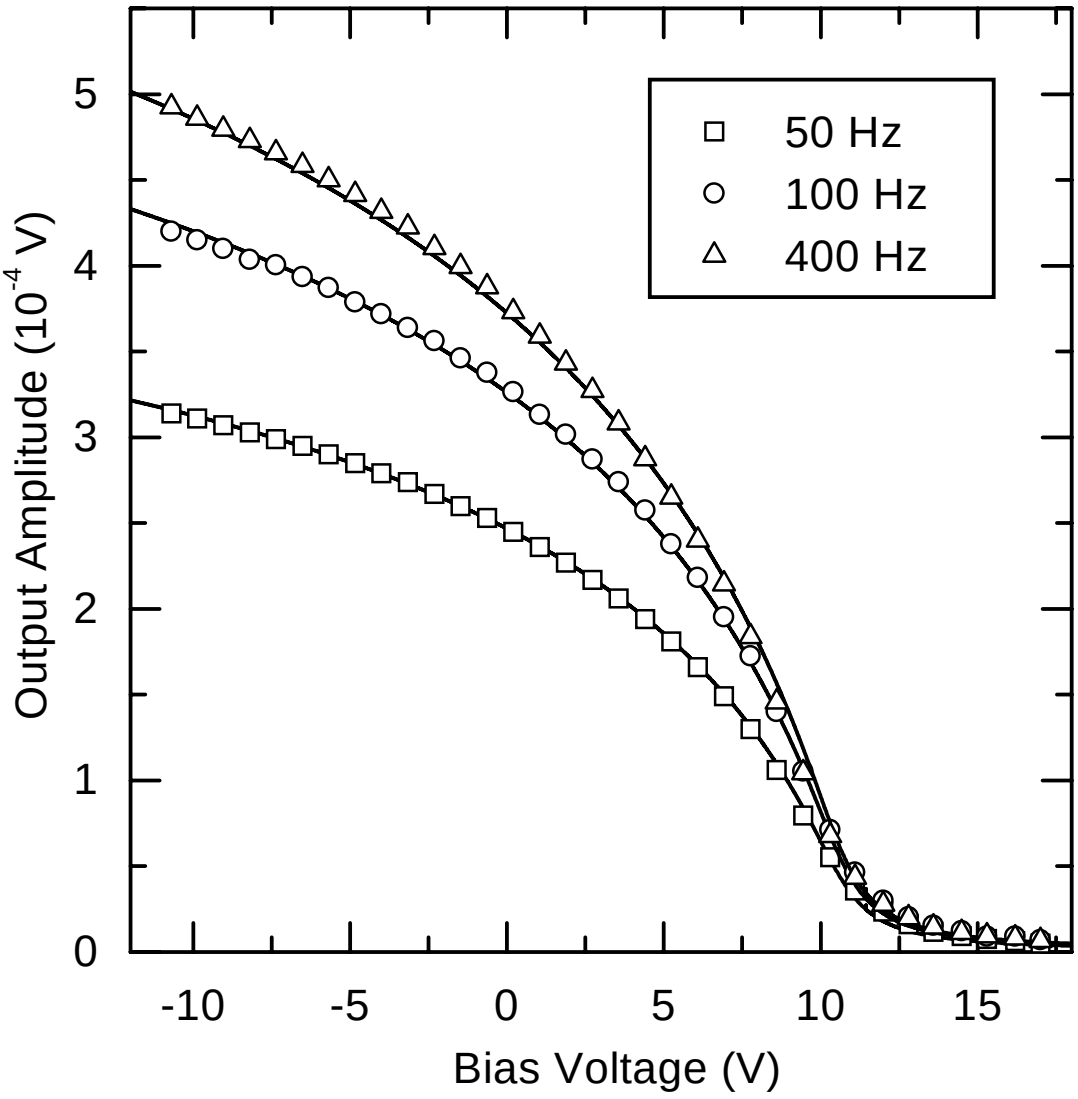

Figure 2.13: Scaled voltage output amplitude of a 0.12 mm^2 MIS diode as a function of dc bias for several strain frequencies. Solid lines show prediction of theory in each case for a strain of 1×10^{-6}. Measured data was scaled vertically to correspond with the theoretical curves.

from the tight theoretical fit of the C-V data. The only adjustable parameter in these curves was the actual strain magnitude S_1, which was not calibrated independently. As a result, each measured curve was scaled uniformly to correspond to its theoretical fit for a strain magnitude of $S_1 = 10^{-6}$.

Unlike in the case of the Schottky diode in the previous section, the prediction of theory here matches the observed voltage dependence of the output amplitude exactly. Note that the amplitude increases in reverse for the MIS diode. This behavior most likely explains the deviation from theory encountered in the last section considering the measurements for the Schottky diodes were contaminated by an additive signal from the MIS contact pads. Note also that the amplitude vanishes as the MIS diode is driven into accumulation, and changes rapidly with bias in the vicinity of the flat-band voltage. Both of these characteristics have important practical applications which we will address later. From the perspective of our equivalent circuit, when the diode is driven into accumulation, the semiconductor capacitance becomes very large, effectively shorting the piezoelectric current source and causing the output voltage to become vanishingly small. From a physical perspective, when the diode is in accumulation, there is no electrostatic barrier to repel free electrons from the GaN/oxide interface. As a result, these carriers can flow toward or away from the surface and effectively negate the piezoelectric charge generated there. Conversely, when the diode is biased in reverse, a large barrier prevents the flow of electrons to the surface. In this case, free carriers can only screen the surface bound charge at a distance no closer than the depletion width. As a result, a voltage will develop across this depletion layer in response to strain, the amplitude of which will increase as the depletion layer widens and hence as the semiconductor capacitance diminishes.

The frequency dependence of the amplitude of the electro-mechanical output voltage is shown in Fig. 2.14. Each empirical curve in the figure corresponds to a different bias state of the diode ranging from deep depletion (-11 V) to accumulation (+18 V). As usual, the solid lines represent the prediction of Eqn. 2.37 for each bias state. As is evident from the figure, when the diode is biased into accumulation, the amplitude is zero for all frequencies f and the device is essentially shut off for strain detection.

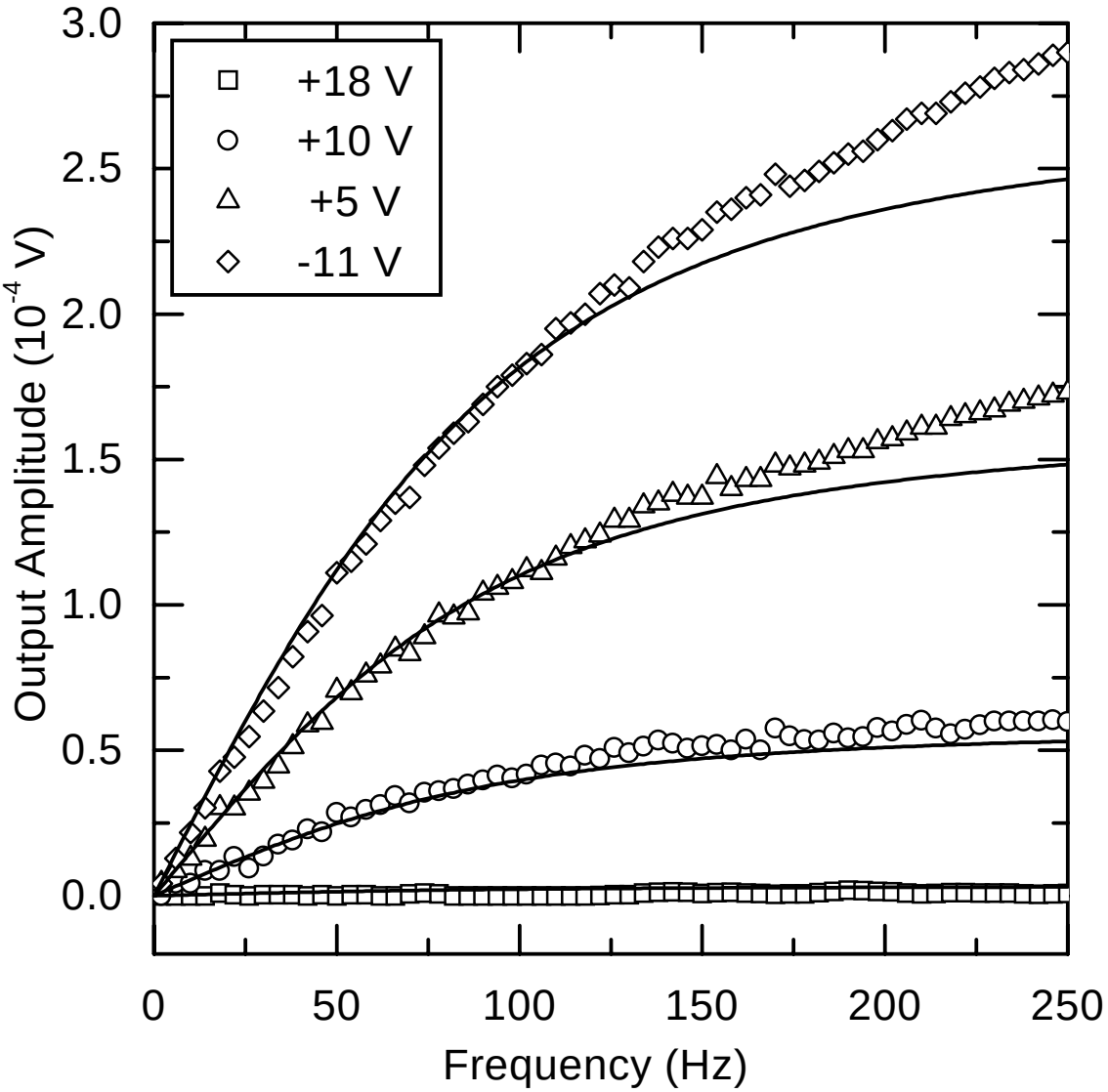

Figure 2.14: Voltage output amplitude as a function of strain frequency for several dc bias states of a 0.013 mm^2 MIS diode. Solid lines correspond to the prediction of theory at a strain amplitude of 3.0×10^{-6}.

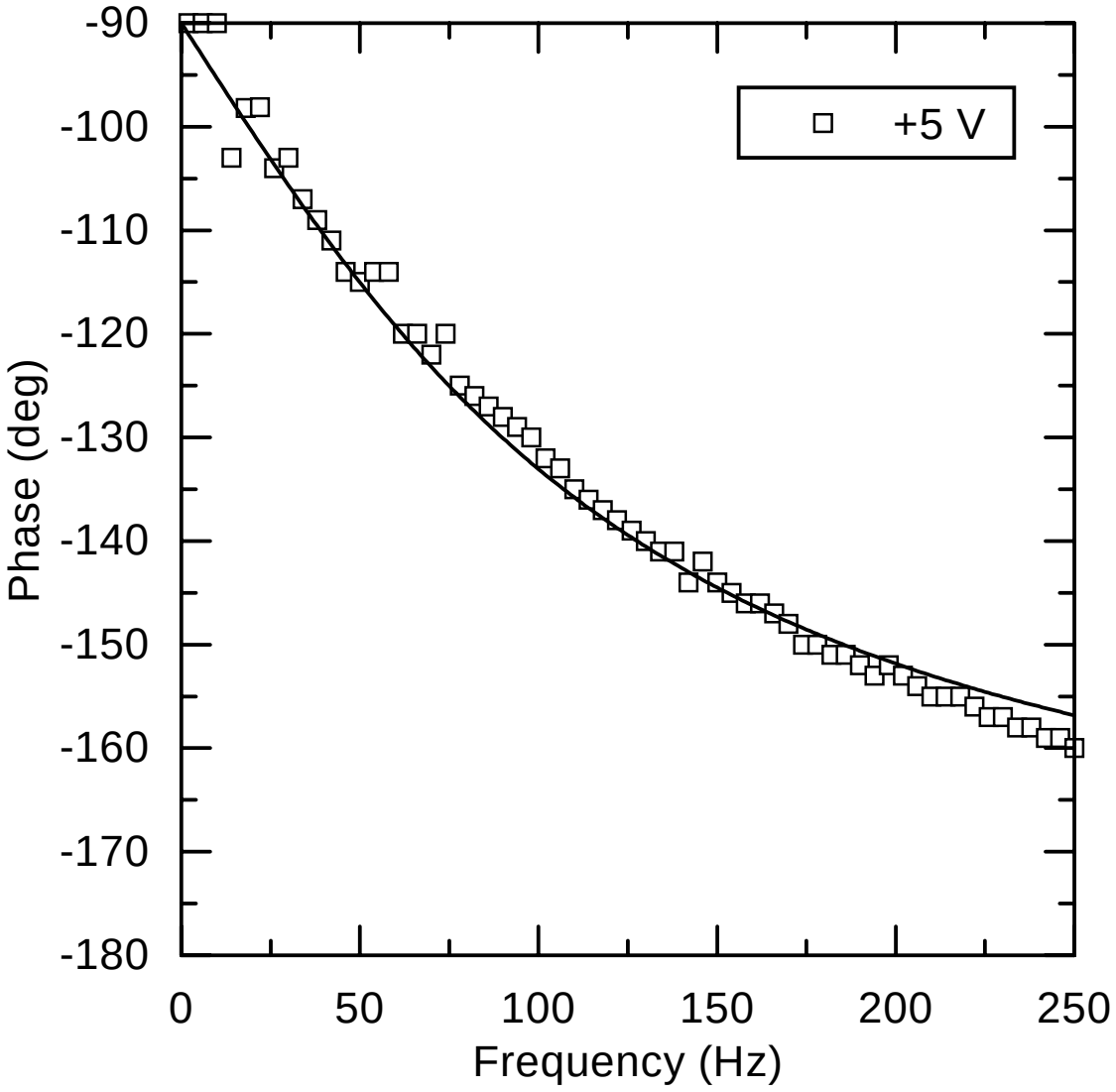

Figure 2.15: Phase of the output signal relative to the strain as a function of frequency for a 0.013 mm^2 MIS diode. For a device of this area, all reverse bias states of the MIS diode give essentially the same phase response. Solid line corresponds to theory.

All other bias states shown in the figure share the same functional characteristics: the amplitude increases linearly with f for low frequencies, and ultimately rolls off to a constant value depending upon the bias. As in the case of the Schottky diode, the behavior of the amplitude with respect to frequency can be easily understood in terms of the parallel RC network discussed above. For low frequencies, this network is resistive in nature, and the electro-mechanical output is given approximately by:

$$V(\omega \to 0) \approx \frac{C_d}{C_s} R_b A i \omega e'_{31} S_1 \tag{2.39}$$

As observed in the data, the amplitude vanishes at dc ($\omega = 0$), and increases linearly with frequency with a slope dependent upon the bias state of the diode as expressed by the leading term (C_d/C_s) in Eqn. 2.39.

For large frequencies, the character of the network rolls over from resistive to capacitive, and the corresponding limit of Eqn. 2.37 becomes:

$$V(\omega \to \infty) \approx \frac{C_d}{C_s} \left(\frac{1}{(C_d + C_{stray})} \right) A e'_{31} S_1 \tag{2.40}$$

In this case, the output voltage amplitude converges to some constant value, independent of frequency, which depends upon: (i) the bias state of the diode, and (ii) the magnitude of the stray capacitance relative to that of the diode itself. The data presented in Fig. 2.14 was measured on a MIS diode with a relatively small gate area of 0.013 mm^2, almost ten times smaller than the device presented in Fig. 2.13. For a device of this size, the capacitance of the diode C_d is dominated by the stray capacitance of the test fixture C_{stray}. As a result, the data in this figure is representative of the frequency dependence expected from a MIS transducer deployed on a typical micron scale electro-mechanical element. As noted before, in contrast to the Schottky diode, the MIS diode will exhibit a strong bias dependence of the output amplitude even when the frequency is high and the stray capacitance is dominant. In Fig. 2.14, the deviation of measurement from theory for larger strain frequencies is caused by a variation in the actual strain supplied to the sample via the transducer.

This variation of strain with frequency was clearly evident in the measurements of the Schottky transducers; for this experiment, however, no correction could be applied because strain gauges were not used to independently calibrate the strain.

Fig. 2.15 shows the phase of the output voltage (relative to the strain in the GaN epilayer) as a function of frequency for the same 0.013 mm^2 device. Since all reverse bias states of the diode yielded essentially the same curve, only one bias (+5 V) is shown. Here again, Eqn. 2.37 models the data very well. In particular, since the sign of the effective piezoelectric constant e'_{31} is negative, in the low frequency limit (Eqn. 2.39), the output voltage should be $-90°$ out of phase with the strain; as the frequency becomes large (Eqn. 2.39), this phase difference should converge to $-180°$.

Parametric Amplification

The strong dependence of the output on the dc bias, even when stray capacitance dominates, is a useful property of the MIS diode that is lacking in the Schottky diode. For one, by moving the bias into strong accumulation, the sensor can be effectively turned off. Using this, MIS transducers could be deployed in a planar array to monitor the strain conditions over a broad area. Elements of this array could be individually addressed using a row-column scheme (like in DRAM memory) without the need for separate interconnects to each sensor.

Another important use for the output/bias characteristics is in mixing or up-conversion of the strain signal. Fig. 2.16 is a demonstration of this possibility. Here, a small ac modulation signal (50 Hz) was superimposed on a 5 V dc bias while the diode was strained at 500 Hz. The various curves correspond to different amplitudes of the modulation signal. Nonlinear mixing of the two signals is evidenced in the sidebands around the ordinary (linear) strain signal peak.

Using a much higher modulation frequency, the strain signal could be up-converted for RF transmission. Alternately, it could simply be shifted away from external interference. The most important application, however, is low-noise parametric amplification of the strain signal. Amplification of exactly this kind was recently demonstrated by Raskin *et al.* in a MEMS capacitor composed of an array of metallized silicon-

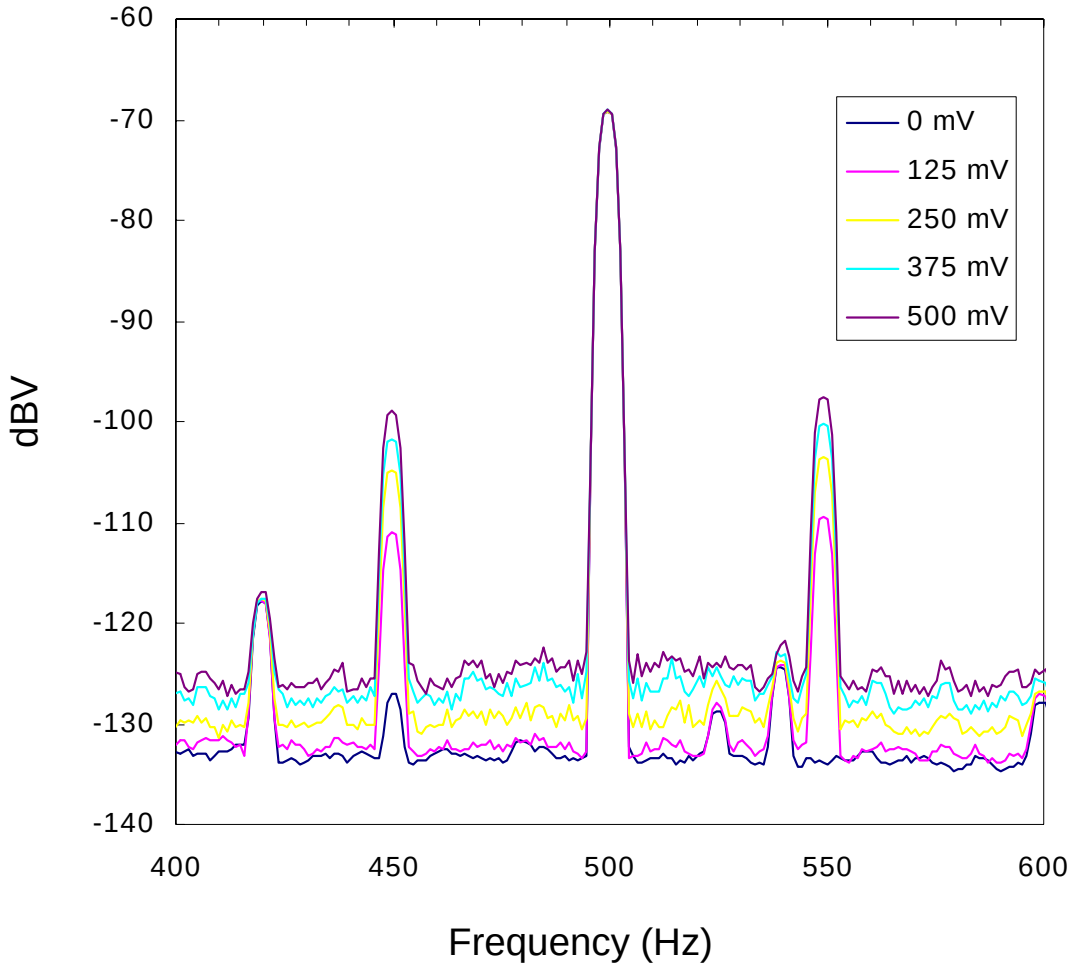

Figure 2.16: Mixing of strain and bias signals at low frequency in a 0.12 mm^2 MIS diode. Each curve corresponds to a different amplitude of the (50 Hz) modulation signal. The strain frequency is 500 Hz.

nitride diaphrams [5].

2.3.4 Conclusions

In summary, we have studied the electromechanical response of MIS diodes on n-GaN as a function of frequency and dc bias. The measurements were found to be in close agreement with a simple model of piezoelectric transduction in this device context. The output versus bias characteristics of these sensors are well suited for a host of signal processing applications.

Bibliography

[1] E. Nicollian and J. Brews, *MOS Physics and Technology*, 1st ed. (John Wiley & Sons, Inc., New York, NY, USA, 1982).

[2] H. Casey, G. Fountain, R. Alley, B. Keller, and S. DenBaars, Applied Physics Letters **68**, 1850 (1996).

[3] J. Nye, *Physical Properties of Crystals*, 2nd ed. (Oxford University Press, New York, NY, USA, 1985).

[4] A. Zoroddu, F. Bernardini, P. Ruggerone, and V. Fiorentini, Physical Review B **64**, 1 (2001).

[5] J. Raskin, A. Brown, B. Khuri-Yakub, and G. Rebeiz, Journal of Microelectromechanical Systems **9**, 528 (2000).

2.4 MIS Capacitive Sensors

2.4.1 Introduction

Piezoelectric effects lie at the heart of many existing III-V nitride devices, most notably the well-studied AlGaN/GaN heterojunction field-effect transistor (HFET) which has marked its place for high power and high frequency electronics [1]. These transistors are but one example of a broader class of *piezoelectronic* devices in the nitrides, devices which exploit the unique combination of large piezoelectricity with conventional semiconductor properties. A natural, but somewhat neglected, extension of this class would be GaN semiconductor strain sensors. The development of sensors of this type is especially germane given the broad range of suspended micro- and nano-mechanical structures that can now be fashioned in GaN [2]. Highly sensitive strain detectors, integrated on these platforms, would open the door for an entire family of diverse and flexible sensors using GaN.

In the previous two sections, we demonstrated how the large piezoelectric effect in GaN can be exploited to create highly sensitive strain detectors using Schottky and MIS diodes. Strain is measured through the voltage which develops across the diode due to its high intrinsic blocking resistance. Because this voltage is transient, GaN Schottky diodes, like other piezoelectric sensors, are only sensitive to dynamic strain, with a practical lower cut-off frequency of approximately 10 Hz. However, many applications, such as in pressure, force, or displacement sensing, call for the measurement of a strain which is either slowly varying or completely static. Sensing at dc would seem to present a serious challenge for GaN owing to the relatively high density of free carriers which will move, if given sufficient time, to negate any piezoelectric bound charge. In the following, we will show that static strain sensing in GaN is not only possible, but highly practical, using a simple MIS diode. Due to the piezoelectric bound charge which forms at the oxide interface, a dc strain will lead to a steady-state shift in the electrostatic surface potential inside the MIS diode. This shift, in turn, will cause a change in the diode capacitance. In this way, GaN MIS diodes can be operated like conventional capacitive strain sensors, but with a

sensitivity that is orders of magnitude larger.

In this work, we present an extensive study on the use of GaN MIS diodes as piezoelectrically enhanced capacitive strain sensors. In section II, we report on the fabrication and interface quality of these diodes, as well as the experimental setup used to measure their response to static strain. In section III(A), we lay out a theory to predict the change in capacitance with strain for the case of an ideal diode without interface states. We find this theory gives excellent agreement with the measurements, in particular, with regard to: (i) the dependence of the capacitance change on the dc bias applied to the diode, and (ii) the linearity of this change with strain magnitude. In section III(B), we exploit the model to infer operational and design rules which optimize the sensitivity, or gauge factor, of the GaN MIS sensor. In the course of this discussion, we find that the devices tested here compare favorably with conventional semiconductor strain gauges, but could readily attain an order of magnitude improvement in sensitivity with only minor design changes. In section III(C), we consider the detrimental role of interface states. To illustrate their effects, we provide data on MIS diodes that were deliberately prepared to have a low quality oxide interface. By modifying the theory to include surface charging, we develop an objective criterion to gauge the effects of interface states on sensor performance. A glaring consequence of this analysis is that static strain sensing in GaN is enabled not only by the large piezoelectric constants, but also by the low surface state densities which are attainable with this semiconductor.

2.4.2 Experimental Setup

The GaN sample used in this experiment was grown by metalorganic chemical vapor deposition (MOCVD) on a c-plane sapphire substrate. The growth consists of three epitaxial layers: (i) a 40 nm AlN buffer layer; (ii) a 5.0 μm n^+-GaN base layer which was doped with Si at a level of $5 \times 10^{18}/cm^3$; and (iii) a 3.0 μm n-GaN surface layer lowly doped at $7 \times 10^{16}/cm^3$. The growth resulted in Ga-polar (0001) film with a sheet resistance of 40 Ω/square.

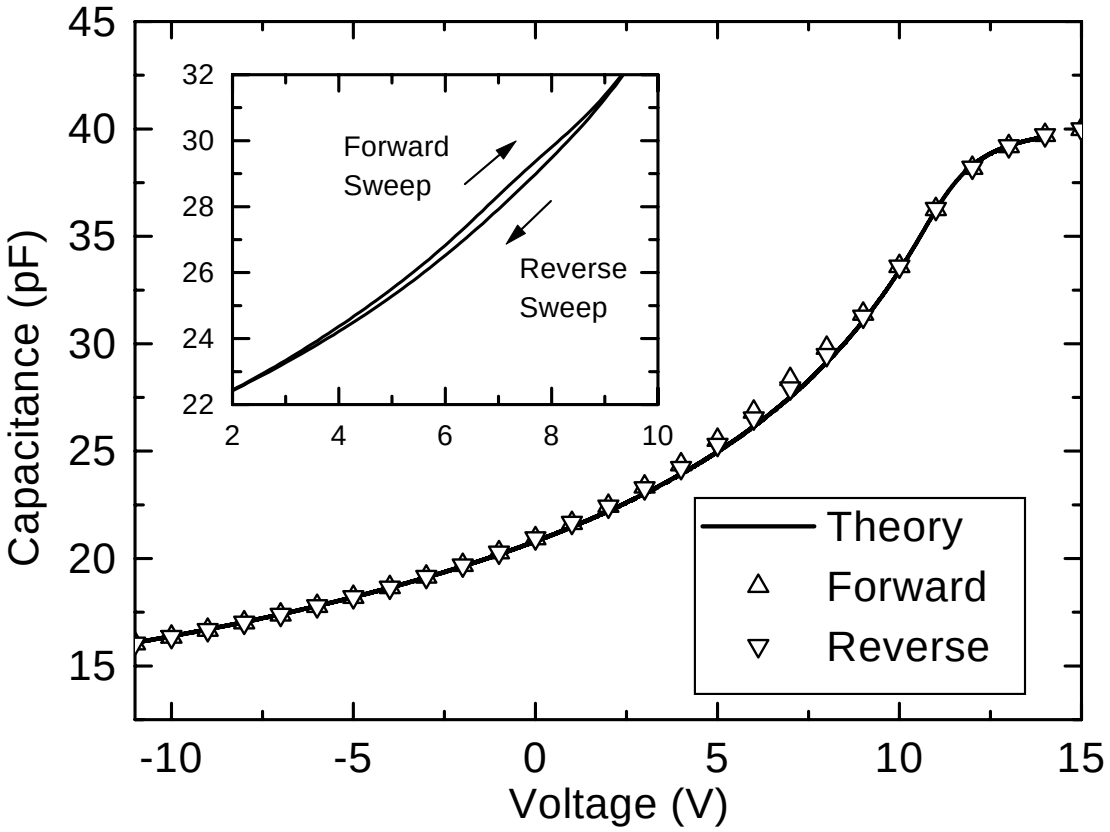

Figure 2.17: Room-temperature C-V characteristics for a 0.12 mm^2 GaN MIS diode showing both forward and reverse sweeps. The data was taken at a ramp rate of .01 V/s and a spot frequency of 100 kHz. The solid line represents a theoretical fit for an ideal diode. The inset shows an expanded view of a small hysteresis likely caused by interface states.

To form the MIS diodes, a 90 nm SiO_2 layer was deposited on the GaN surface by plasma-enhanced chemical vapor deposition (PECVD) at a temperature of 350 °C. A 100 nm Al layer was then sputter deposited on the insulator and subsequently patterned into 390 μm diameter circular gate electrodes by etching down in phosphoric acid. The ohmic contacts, consisting of an Al-Ni-Au (50 nm-30 nm-50 nm) stack, were sputter deposited on the GaN surface in windows etched out of the insulator layer using hydroflouric acid. These contacts were ohmic as deposited.

The room temperature capacitance-voltage (C-V) characteristics of a typical MIS diode are shown in Fig. 2.17. The forward and reverse sweeps shown here were measured in the dark at a frequency of 100 kHz and a voltage sweep rate of 10 mV/s. The solid line shows a theoretical fit to the data using the exact solution for the high-frequency capacitance of an ideal MIS diode without interface states [4]. Due to the prohibitively low minority carrier generation rate in GaN at room temperature [5], this analytical solution was modified to exclude the effect of any minority carrier holes. As a result, the capacitance exhibits a deep depletion characteristic for large reverse biases. The fit shown corresponds to a flat band voltage of $V_{fb} = 12.0$ V and an oxide dielectric constant of $\epsilon_i = 3.5\ \epsilon_0$.

A small capacitance hysteresis is evident in the expanded view inset of Fig. 2.17. The clockwise orientation of this hysteresis, as well as the slight "ledge" seen on the forward sweep [6], are both consistent with the effects of interface states. Using the Terman technique [7], we found a mean interface state density of $3.2 \times 10^{11}\ cm^{-2}\ eV^{-1}$ over the range of 0.3 eV to 0.65 eV below the conduction band edge. On the basis of measured time constants for electron emission from interface traps [8], this narrow range in energy was deemed to be the limits of validity for the Terman method given our measurement conditions. The interface state density found here agrees well with previous measurements for PECVD SiO_2 on n-GaN [9], but is significantly higher than the value of $< 5.0 \times 10^{10}\ cm^{-2}\ eV^{-1}$ quoted for optimized oxide/nitride/oxide insulator stacks [8].

Fig. 2.18 shows the experimental setup used to study the effects of strain on these MIS diodes. GaN samples, with dimensions 5 × 30 mm, were anchored at

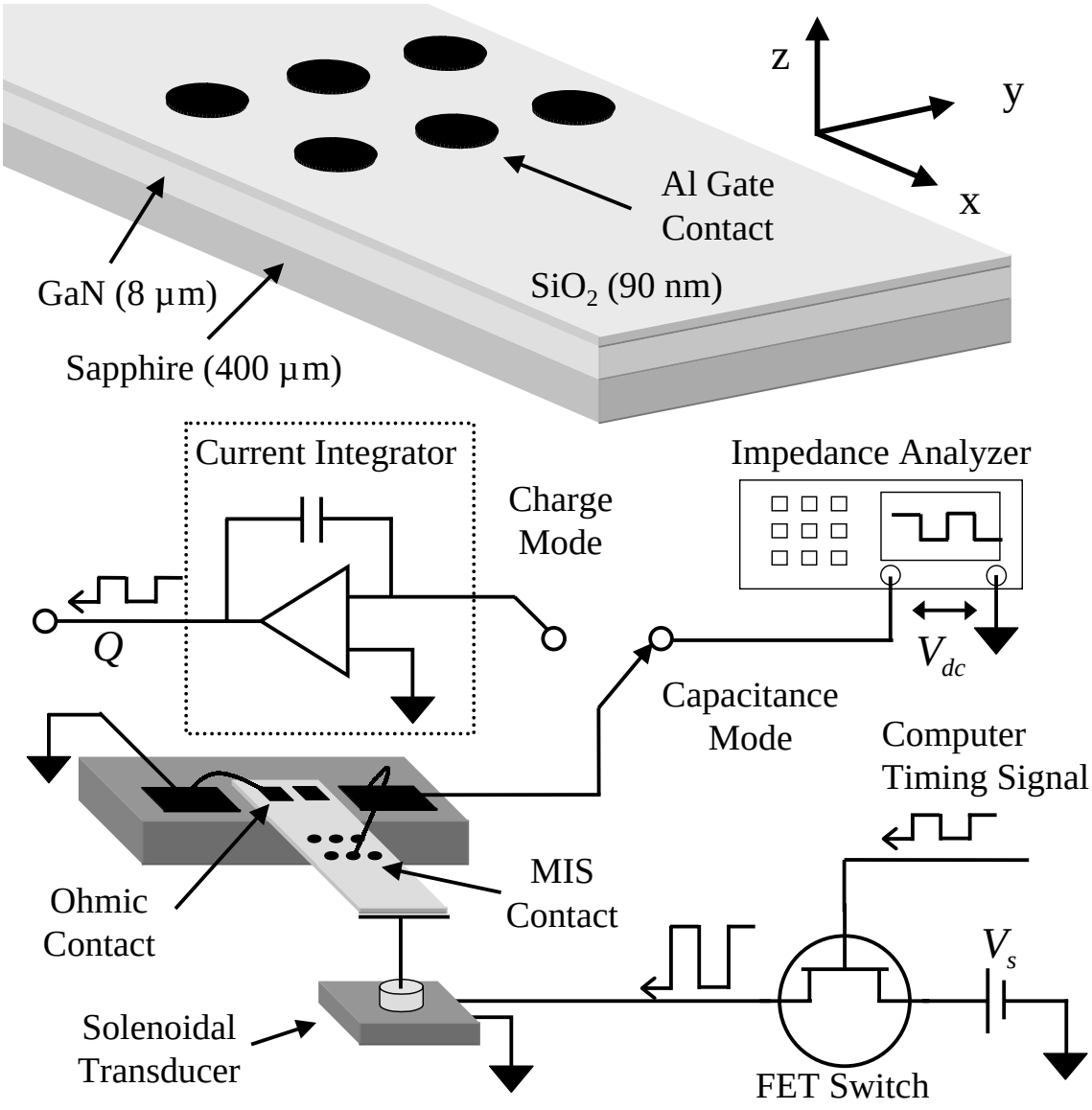

Figure 2.18: Experimental setup used to measure the capacitance change and charge flow of GaN MIS diodes in response to strain.

one end to a rigid support fixture to form a suspended cantilever. A wire, affixed at the free end of the cantilever, conveyed a mechanical line force to the sample from a solenoidal transducer below. Referring to the coordinate axes in Fig. 2.18, the resulting deformation of the GaN epilayer is a mixture of longitudinal strain in x (S_1) and in z (S_3). Using standard reduced notation [10], these components of strain are related by:

$$S_3 = -\frac{C_{31}}{C_{33}} S_1 \tag{2.41}$$

where C_{ij} are the components of the GaN elastic tensor. Given the relative thickness of the GaN epilayer (8 μm) to the sapphire substrate (400 μm), these strain conditions are approximately uniform in z across the film thickness, but vary in x along the length of the cantilever.

As seen in Fig. 2.18, the force supplied by the transducer was computer controlled by way of a digital timing signal sent to the gate of a high-power analog switch. The magnitude of this force could be adjusted by varying the supply voltage V_s of the switch circuit. Synchronously, a HP4192A Impedance Analyzer measured the capacitance of the MIS diode at a particular dc bias level. A representative trace of the resulting capacitance data is shown in Fig. 2.19(a); the corresponding timing signal is shown in Fig. 2.19(c). Because of the large fractional change in capacitance with strain, a Wheatstone bridge circuit was not necessary.

To calibrate the mean strain in the GaN epilayer immediately below the MIS diode, the total charge which had moved from the metal to the semiconductor side of the diode was monitored in time using an ultra-low drift Keithley 6517A current integrator. A typical trace of this charge data is shown in Fig. 2.19(b). As discussed in section III, the change in charge (from peak to trough in the trace) is related in a simple, linear manner to the change in strain of the diode. Charge measurements were performed for each supply voltage V_s and therefore for each force level applied by the transducer. Using this method, the measured strain levels imposed on the diodes in this experiment were in the range from 10^{-6} to 10^{-4}.

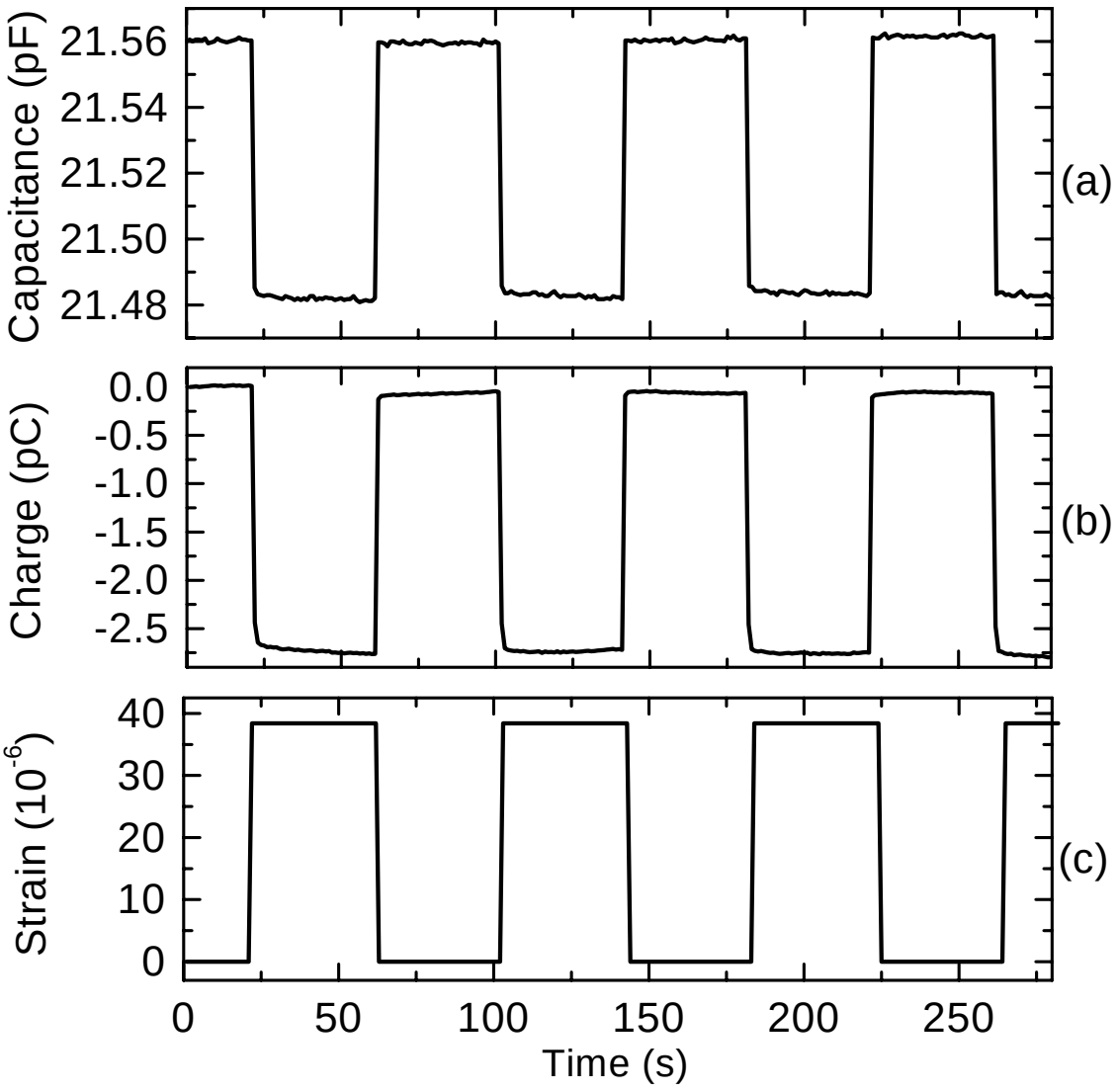

Figure 2.19: Representative time series of the capacitance (a) and charge (b) measured from a MIS diode for a strain (c) cycled every 80 s. The diode bias was 0 V for both traces. The actual strain magnitude shown in (c) was inferred from the amplitude of the charge swing averaged over many cycles.

2.4.3 Results and Discussion

In the following section, we will set forth a simple theory to describe the change in steady-state capacitance of a GaN MIS diode resulting from an applied static strain. In this analysis, we are concerned with the final state of the diode, maintained at constant dc bias, a long time after the initial application of strain. The transient electrical response of the device, however, is the basis for a class of highly sensitive dynamic strain sensors in GaN; sensors of this type, using both MIS and Schottky diodes [3], are treated elsewhere.

Whether static or dynamic, strain affects the state of a MIS diode by introducing a piezoelectric bound charge within the semiconductor. Assuming the strain is uniform in the vicinity of the diode, this bound charge will take the form of equal and opposite sheet charge densities at the two c-plane faces of the epilayer. For the coupled strain conditions in this experiment (Eqn. 2.41), the magnitude of the sheet charge density at the GaN-insulator interface (σ_b) is related to the strain in x (S_1) via:

$$\sigma_b = e'_{31} S_1 \equiv \left(e_{31} - \frac{C_{31}}{C_{33}} e_{33} \right) S_1 \tag{2.42}$$

Here, e'_{31} denotes an effective piezoelectric constant having a value of -0.61 C/m^2 derived from reported material constants for GaN [11].

However, the final state of the diode is determined not only by the bound charge, but also by the redistribution of free charge in response to the strain. In fact, if free charge, of opposite sign, can move to the interface region and form a sheet charge which exactly cancels the bound charge, the strain will have no net electrostatic effect on the final state of the diode. Cancellation of this type is very pronounced in a Schottky diode, where free charge can develop on the metal surface (or in interface states), leaving the diode essentially unchanged as a result of strain.

However, for a MIS diode with no interface states, the situation is fundamentally different. In this case, the insulating layer prevents the formation of compensating sheet charge at the semiconductor surface, not because free carriers are unable to reach the surface, but because there are no states for them to occupy there. Thus,

free charge can not cancel the bound charge, but merely screens it at some distance by redistributing in the bulk of the semiconductor or on the metal surface. As a result, strain will alter the electrostatics inside the diode, and in particular, will change the surface potential at the GaN-insulator interface. This change, in turn, can be readily observed in the capacitance of the diode. For a realistic diode, interface states will act to reduce the change in surface potential for a given strain. If the density of these states is very high, only a relatively small change in surface potential will result in almost complete cancellation of the surface bound charge.

Model for an Ideal Diode

In the following part, we present a theoretical description of the effects of strain in an ideal MIS diode without interface states. This description will compare the state of the diode before and after strain in terms of two measurable quantities: (i) the change in capacitance, and (ii) the total charge which flows from the metal to the semiconductor side of the device. In addition to having no interface states, the diode is assumed to have an insulator layer containing no mobile charge of any kind.

For a GaN MIS diode satisfying these assumptions, the state of the device is completely determined by the surface potential Φ_s, the electrostatic potential at the semiconductor-insulator surface relative to that in the bulk. For an unstrained diode in steady-state, the surface potential is related to the applied dc bias V via:

$$V_{bi} - V = \Phi_s + \frac{z_i}{\epsilon_i}\epsilon_s \dot{\Phi}_s \tag{2.43}$$

where ϵ_i and ϵ_s are the insulator and semiconductor dielectric constants, z_i is the oxide thickness, and V_{bi} is the built-in voltage of the MIS junction [4]. In our sign convention, the spatial derivative of the potential is the electric field. The quantity $\dot{\Phi}_s$ appearing in Eqn. 2.43 is the electric field in the semiconductor at the surface; for a fixed doping level, it is a function of Φ_s alone. Using this formalism, the capacitance

of the diode per unit area, C_d, can be expressed by:

$$C_d \equiv \frac{dQ}{dV} = \left(\frac{1}{\epsilon_s} \frac{d\Phi_s}{d\dot{\Phi}_s} + \frac{z_i}{\epsilon_i} \right)^{-1} \tag{2.44}$$

Eqn. 2.44 is valid for all values of Φ_s, and therefore, for all biases applied to the diode.

When the MIS diode is uniformly strained, a piezoelectric sheet charge density σ_b (Eqn. 2.42) arises at the GaN-oxide interface. Because this bound charge alters the boundary conditions for the electric field at the semiconductor surface, the relationship between the surface potential and the applied bias must be modified to read:

$$V_{bi} - V = \Phi_s + \frac{z_i}{\epsilon_i} \epsilon_s \dot{\Phi}_s + \frac{z_i}{\epsilon_i} e'_{31} S_1 \tag{2.45}$$

A comparison of Eqns. 2.43 and 2.45 shows that, if the diode is maintained at a constant bias V, the application of strain will cause the surface potential to change.

In addition to the surface potential, the charge on the metal surface Q_m will change as a result of strain. Using boundary conditions for the electric field at the metal-oxide interface, this free charge is given by:

$$Q_m = -A(\epsilon_s \dot{\Phi}_s + e'_{31} S_1) \tag{2.46}$$

where A is the device area. The total charge ΔQ flowing from the metal to the semiconductor as a result of strain is the difference in Q_m between the initial and final states of the diode. A combination Eqns. 2.46, 2.45, and 2.44 yields the following expression valid for small strain:

$$\Delta Q = A e'_{31} S_1 \left(1 - \frac{C_d}{C_i} \right) \tag{2.47}$$

where we have introduced $C_i = \epsilon_i / z_i$ to denote the oxide capacitance per unit area. Note that, for any bias, the ratio of the diode to the oxide capacitance appearing in Eqn. 2.47 can be precisely inferred from the C-V characteristics (Fig. 2.17). With

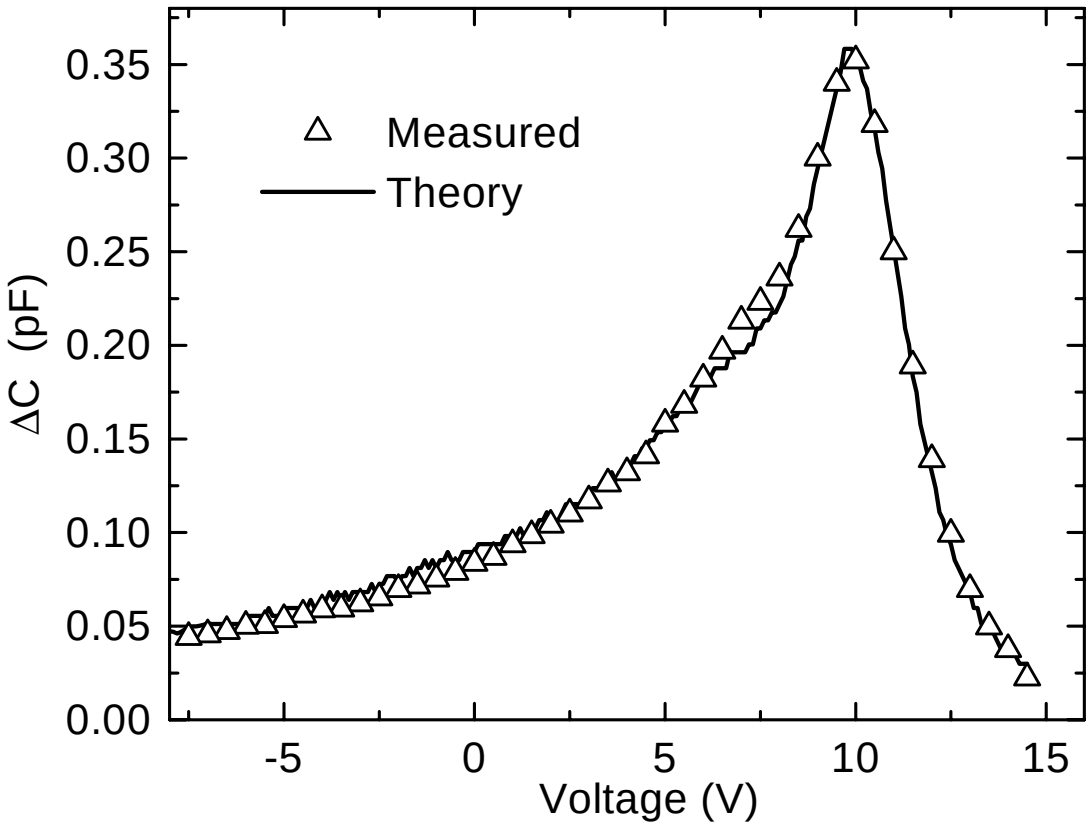

Figure 2.20: Measured capacitance change ΔC versus diode bias for a strain magnitude of 7.0×10^{-5}. The solid line shows the theoretical prediction based on the empirical C-V profile.

this knowledge in tow, a measurement of ΔQ provides a direct determination of the bound charge σ_b at the GaN surface, and an estimate of the actual strain to within the accuracy of the GaN effective piezoelectric constant.

The change in capacitance ΔC resulting from strain can be derived using an intuitive graphical approach. By comparing Eqns. 2.43 and 2.45, the effect of piezoelectric bound charge is to shift the bias voltage corresponding to the same surface potential by an amount:

$$\Delta V = \frac{e'_{31} S_1}{C_i} \tag{2.48}$$

Since the capacitance is a function of Φ_s alone, strain will therefore simply translate the C-V characteristics to the left by an amount ΔV along the voltage axis. In this regard, the piezoelectric charge is totally analogous to the familiar oxide fixed charge appearing at the surface in MOS diodes [4]. Thus, the change in capacitance per unit area is:

$$\frac{\Delta C}{A} = C_d(V + \Delta V) - C_d(V) \approx \left[\frac{dC_d}{dV}\right] \frac{e'_{31} S_1}{C_i} \tag{2.49}$$

where the last equation applies in the limit of small strain.

Fig. 2.20 shows a plot of the measured capacitance change as a function of bias. The strain applied during this sweep was $S_1 = 7.0 \times 10^{-5}$ corresponding to a calibrated charge of $\Delta Q = 2.5$ pC. The voltage shift, on the basis of Eqn. 2.48, is therefore $\Delta V = 0.13$ V. The solid line overlaid on the data in Fig. 2.20 shows the theoretical dependence of capacitance change on bias expressed in Eqn. 2.49. The derivative of the capacitance with respect to voltage was calculated directly from the empirical C-V profile (Fig. 2.17). Since all other quantities in Eqn. 2.49 were known, no adjustable parameters could be used to fit the theoretical curve to the data.

Note that the capacitance change, and hence the sensitivity of the device as a strain sensor, is strongly dependent on gate bias. For large positive gate voltages, electrons in the semiconductor accumulate at the oxide interface. When the diode is strained, these electrons will screen the surface bound charge at close proximity with a corresponding slight change in surface potential. In this case, the screening process is accomplished by a redistribution of charge inside the semiconductor, with

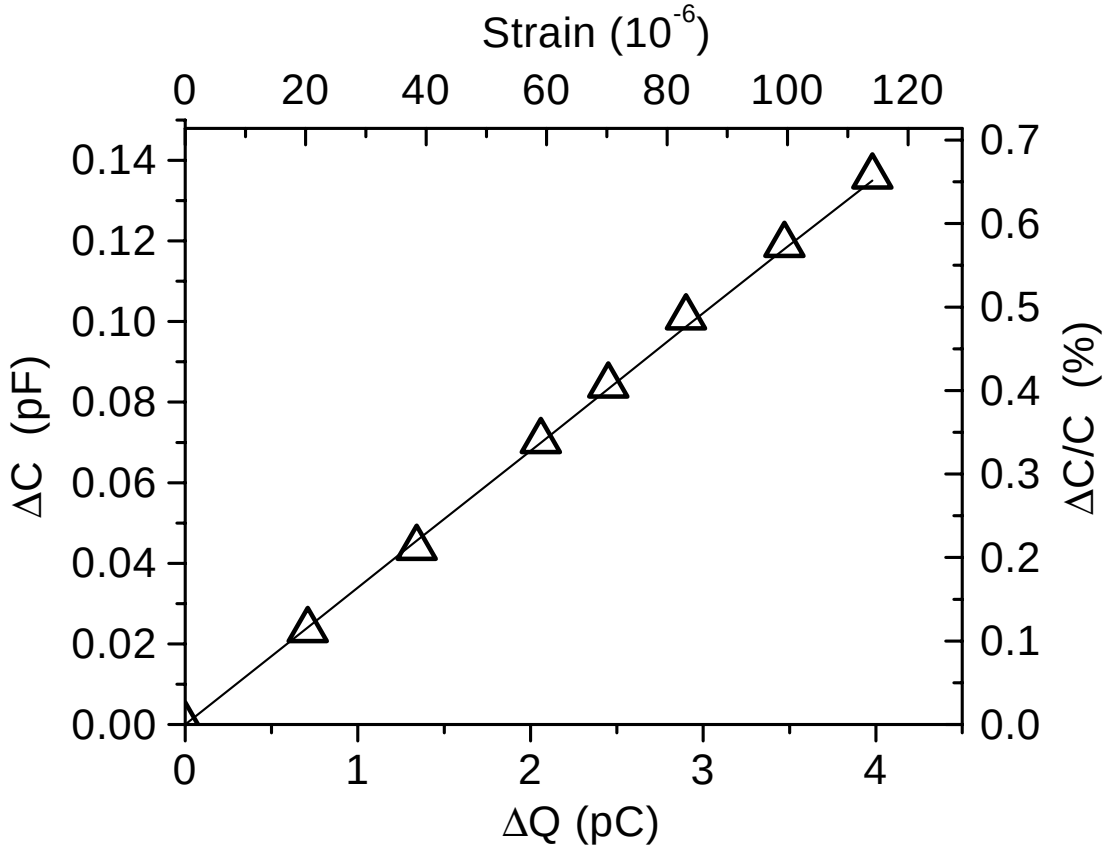

Figure 2.21: Linearity of the capacitance change ΔC with the strain magnitude for a fixed bias of 0 V. For each datum, the strain was calibrated from the charge swing ΔQ. The right axis shows fractional change in capacitance.

no net flow of charge to the metal (as predicted by Eqn. 2.47 when $C_d = C_i$). Since the surface potential changes only slightly, the change in capacitance is small and ultimately vanishes as the diode is biased further into accumulation. For reverse biases, an electrostatic barrier prevents the flow of carriers to the surface. Electrons in the semiconductor can screen the surface bound charge at a distance no closer than the depletion width. As the reverse bias becomes larger, the depletion width widens, and charge begins to flow increasingly to the metal surface in order to screen the piezoelectric charge. Here, the change in Φ_s approaches a maximum, but ΔC drops off because the diode capacitance changes more slowly with surface potential.

Fig. 2.21 shows the measured capacitance change as a function of strain magnitude for a fixed bias voltage of 0 V. Clearly, the capacitance change is a highly linear measure of the strain in the range extending up to $S_1 = 10^{-4}$. For larger strains, the deviation from linearity can be inferred by comparing the exact expression for ΔC in Eqn. 2.49 with its first-order approximation. For the device tested here, operating at 0 V bias, the deviation is less than 10% for strains up to $S_1 = 1.2 \times 10^{-3}$. When operated at the bias for maximal capacitance change, the diode has a linearity better than 99% for strain less than 1.5×10^{-4} and 90% for strain less than 4.5×10^{-4}. If necessary, the linear range of operation for a strain sensor of this type could be greatly extended by introducing a non-uniform doping profile in the GaN epilayer like that used in hyper-abrupt varactor diodes [12].

Device Optimization

To judge the sensitivity of GaN capacitive strain sensors, a useful figure of merit is the gauge factor G_F commonly used to characterize piezoresistive sensors. In our case, this factor is a measure of the fractional change in capacitance per unit strain applied:

$$G_F = \frac{\Delta C}{C} \times \frac{1}{S_1} \tag{2.50}$$

If the MIS diode is deployed in an optimally matched Wheatstone bridge circuit, the gauge factor determines the output voltage amplitude, per unit reference voltage,

resulting from strain [13]. For a GaN capacitive sensor, G_F depends upon the gate bias, the semiconductor doping, and the oxide capacitance. For the device discussed in part A, a maximum G_F of 151 is obtained at a gate voltage of roughly 10 V. This should be compared with a value of 1 for ordinary capacitive sensors, and a value of 150 for the best silicon piezoresistive sensors [13]. However, GaN MIS sensors can attain even larger gauge factors by varying the oxide capacitance and the doping density.

To derive the optimal design criteria for a MIS strain sensor, we can express the gauge factor in terms of device parameters by combining Eqns. 2.50 and 2.49:

$$G_F = -e'_{31}\frac{z_i}{\epsilon_i}\left[\frac{\partial \ln C}{\partial V}\right] \tag{2.51}$$

Using the exact analytic solution for the capacitance of a MIS diode [4], Eqn. 2.51 can be recast into a more dimensionally revealing form:

$$G_F = \frac{e'_{31}L_D}{\epsilon_s(kT/q)} \times F(C'_i, \Phi'_s) \tag{2.52}$$

where L_d is the Debye length of the semiconductor which depends on the doping density via:

$$L_D = \left[\frac{\epsilon_s kT}{q^2 N_d}\right]^{1/2} \tag{2.53}$$

The function $F(C'_i, \phi'_s)$ appearing in Eqn. 2.52 depends only on two dimensionless quantities: (i) a unitless oxide capacitance $C'_i \equiv (\epsilon_i L_D)/z_i\epsilon_s$ and (ii) the normalized surface potential $\Phi'_s \equiv \Phi_s/(kT/q)$. When F is numerically optimized over both variables, the rules for maximal device sensitivity emerge. At a given doping density (and hence L_D), the ideal oxide capacitance will be:

$$C_i = \epsilon_i/z_i = 0.56 \times \epsilon_s/L_d \tag{2.54}$$

For this oxide capacitance, the optimum gate bias is such that the surface potential $\Phi_s = 2.08 \times (kT/q)$, or, alternatively, such that the diode capacitance is half the oxide

capacitance:

$$C_d = 0.5 \times C_i \tag{2.55}$$

Under these conditions, the gauge factor for the MIS capacitive sensor will be given by:

$$G_F = \frac{e'_{31} L_D}{\epsilon_s (kT/q)} \times (9.77 \times 10^{-2}) \tag{2.56}$$

It is apparent from Eqn. 2.56 that the magnitude of the gauge factor scales as the Debye length, and hence as $1/\sqrt{N_d}$. Thus, the device sensitivity will improve as the doping density is reduced. For the doping of the sample used in this experiment, a maximum gauge factor of 385 can be obtained. If we take $N_d = 10^{16}/cm^3$, a conservative estimate for the present-day lower limit of controllable n-type doping of GaN, we achieve a gauge factor of 1020, nearly 7 times the sensitivity of silicon sensors.

Role of Interface States

If the density of interface states at the GaN surface were not so low, MIS diodes in this material would be essentially useless for low frequency strain detection. There are two principal ways in which these states impair device performance. For one, interface states, being at the semiconductor surface, can directly cancel the piezoelectric bound charge induced by strain. If the density D_{ss} is very high, the free charge residing at the surface will simply adjust to negate the bound charge, causing almost no change in surface potential. As a result, the capacitance change (and hence the gauge factor) will be seriously diminished from its ideal value. Perhaps more detrimental, though, is the potentially long time constants for surface states to fill and empty in response to strain. This slow charging of the surface will lead to a drift in the capacitance of the sensor until equilibrium is restored, making it impossible to track strain which varies on the same time scale.

Both manifestations of surface states are seen quite clearly in Fig. 2.22. Shown here is the strain response for a GaN MIS diode which was deliberately prepared to have a high density of interface states. This was achieved by exposing the sample to

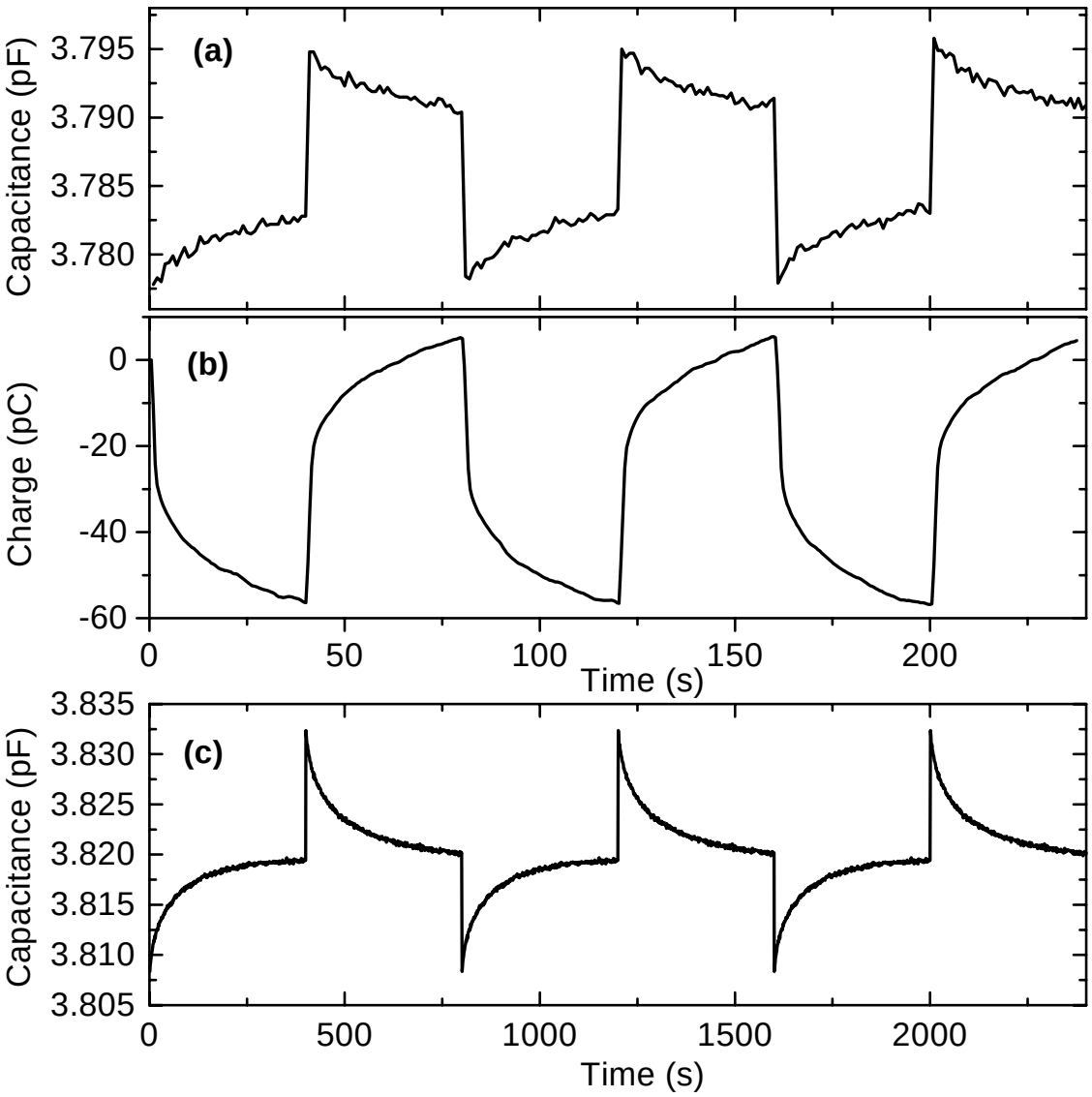

Figure 2.22: Typical traces of the capacitance (a) and charge (b) measured on a GaN MIS diode with high interface state density. The time series in (c) represents the capacitance measured on the same device for a much longer (800 s) strain cycle; for clarity, the data shown here was averaged over many cycles.

hydroflouric acid prior to the SiO_2 deposition, thereby removing some of the native passivating oxide on the GaN surface. Furthermore, the oxide was grown thicker, which, for reasons to be discussed shortly, exaggerates the role of the interface states. The effects on the capacitance and charge traces (Fig. 2.22(a) and (b)) are dramatic; for reference, compare with the same traces for the high-quality diode (Fig. 2.19). When strain is applied to the diode, the capacitance changes but then decays in time toward its original value. During this decay, free charge continues to exchange between the GaN surface and the metal gate. Fig. 2.19(c) shows the capacitance trace of the same diode for a strain cycle with a much longer period. Within 400 seconds after the initial application of strain, the diode capacitance has returned almost completely to its unstrained value; obviously, this sensor is not suitable for detecting static strain.

The final, steady-state capacitance change, when compared to its inital value, represents a loss in the sensitivity to detect static strain. This reduction of ΔC is directly related to the specific density of interface states D_{ss} at the surface Fermi energy set by the given gate bias; the decay rate is related to the time constant for emission from these same states. We can quantify the sensitivity loss by considering the change in surface potential resulting from a small strain in the presence of interface states:

$$\Delta\Phi_s = -e'_{31}S_1\left[C_i + \epsilon_s\frac{d\dot{\Phi}_s}{d\Phi_s} + q^2D_{ss}\right]^{-1} \tag{2.57}$$

where D_{ss} has units of $\mathrm{cm}^{-2}\ \mathrm{eV}^{-1}$. Note that Eqn. 2.57 applies when equilibrium has been restored long after the intial strain. Assuming the diode is biased for optimal response (see section B), the diode capacitance will be half the oxide capacitance, and Eqn. 2.57 simplifies to:

$$\Delta\Phi_s = -e'_{31}S_1\left[2C_i + q^2D_{ss}\right]^{-1} \tag{2.58}$$

Therefore, if we let $\Delta\Phi_s^{ss}$ denote the surface potential shift for a diode with surface

states, and $\Delta\Phi_s^{id}$ the same for an ideal diode, the ratio of the two shifts will be:

$$\frac{\Delta\Phi_s^{ss}}{\Delta\Phi_s^{id}} = \left[1 + \frac{q^2 D_{ss}}{2C_i}\right]^{-1} \tag{2.59}$$

Since the high frequency capacitance in either case depends only on the surface potential, this quantity is also the ratio of the capacitance change with and without surface states. Thus, for measuring static strain, the gauge factor of the diode with interface states (G_F^{ss}) will be reduced from its ideal value (G_F^{id}) by:

$$G_F^{ss} = \left[1 + \frac{q^2 D_{ss}}{2C_i}\right]^{-1} G_F^{id} \tag{2.60}$$

Eqn. 2.60 provides a means to gauge the effect of interface states on sensor performance; for the sensitivity loss to be small, the specific density at the surface Fermi energy must be small in comparision to the oxide capacitance: $q^2 D_{ss} \ll 2C_i$. Using the optimum oxide capacitance for the doping of our samples, the surface state density should be compared to $4.1 \times 10^{12} eV^{-1} cm^{-2}$. In our case, the measured density for the high-quality diodes was more than a factor of ten smaller, leading to less than a 10% reduction of the static gauge factor. If we had matched the lowest reported values to date, $D_{ss} < 5 \times 10^{10}\ eV^{-1}\ cm^{-2}$ [8], the reduction would be utterly neglible. For a surface this close to ideal, the sensor could be doped as low as 10^{15} cm^{-3}, attaining a nominal gauge factor in excess of 3200 with a less than 10% loss from interface states.

No matter the specific density of interface states, if the diode is designed and biased for an optimal gauge factor ($\Phi_s = 2.08 \times (kT/q)$), the drift caused by charging of the surface will seem immediate on timescales longer than $\sim$1 ms. This applies for all attainable doping levels of the semiconductor. If drift is deemed intolerable for a particular sensing application, the diode can always be biased deep into depletion (with an associated penalty in the gauge factor). When the surface Fermi energy exceeds 1 eV from the conduction band edge, the time constant for charging surface states becomes so large ($> 10^7$ s) that drift would not be practically observable.

2.4.4 Conclusions

In summary, we have tested GaN MIS diodes for use as piezoelectrically enhanced capacitive strain sensors. The devices exhibit excellent sensitivity to static strain, with a gauge factor of 151 and a linearity better than 99% for strains less than 1.5 $\times$ 10^{-4}. By changing the oxide capacitance and the doping density, sensors of this type could readily achieve gauge factors in excess of 1000. Finally, we developed an objective criterion to weigh the effects of interface states, and show that, for the high quality surfaces attainable in GaN, these states do not limit sensor performance.

Bibliography

[1] R. Beach and T. McGill, Journal of Vacuum Science and Technology B **17**, 1753 (1999).

[2] R. Strittmatter, R. Beach, and T. McGill, Applied Physics Letters **78**, 3226 (2001).

[3] R. Strittmatter, R. Beach, J. Brooke, E. Preisler, G. Picus, and T. McGill, Journal of Applied Physics (Accepted for publication in May 2003).

[4] E. Nicollian and J. Brews, *MOS Physics and Technology*, 1st ed. (John Wiley & Sons, Inc., New York, NY, USA, 1982).

[5] H. Casey, G. Fountain, R. Alley, B. Keller, and S. DenBaars, Applied Physics Letters **68**, 1850 (1996).

[6] A. Goetzberger and J. Irvin, IEEE Transactions on Electronic Devices **ED-15**, 1009 (1968).

[7] L. Terman, Solid-State Electronics **5**, 285 (1962).

[8] B. Gaffey, L. Guido, X. Wang, and T. Ma, IEEE Transactions on Electronic Devices **48**, 458 (2001).

[9] P. Chen, W. Wang, S. Chua, and Y. Zheng, Applied Physics Letters **79**, 3530 (2001).

[10] J. Nye, *Physical Properties of Crystals*, 2nd ed. (Oxford University Press, New York, NY, USA, 1985).

[11] A. Zoroddu, F. Bernardini, P. Ruggerone, and V. Fiorentini, Physical Review B **64**, 1 (2001).

[12] S. Sze, *Physics of Semiconductor Devices*, 2nd ed. (John Wiley & Sons, Inc., New York, NY, USA, 1981).

[13] J. Fraden, *Handbook of Modern Sensors*, 1st ed. (Springer-Verlag, Inc., New York, NY, USA, 1996).

2.5 MIS-Heterojunction Capacitive Sensors

2.5.1 Introduction

In the last section, it was demonstrated that strain leads to a change in the steady-state band profile of a MIS capacitor. As a result of piezoelectric sheet charge at the oxide/semiconductor interface, the capacitance-voltage characteristics of the device are simply shifted by a certain amount along the voltage axis. For small strains, the change in capacitance is therefore proportional to the derivative of the C-V profile at the operating bias. The larger this slope, the greater the gauge factor of the sensor.

In this section, we discuss a different GaN diode which exhibits a very sharp knee in its C-V characteristic. This diode also employs a MIS structure (with an SiO_2 gate dielectric), but the semiconductor side of the junction consists of an AlGaN/GaN heterostructure. The presence of a two-dimensional electron gas (2DEG) at the hetero-interface in these MISH diodes leads to dramatic differences in the device behavior when compared to ordinary MIS capacitors. As discussed later, the 2DEG, which is primarily a polarization induced phenomena [1], causes action in the device to occur more laterally than vertically. When the gate bias begins to deplete it of carriers, the capacitance drops abruptly to almost zero. When operated in this transition (or threshold) region, a MISH capacitor is expected to exhibit a large gauge factor for sensing strain.

Due to the greater complexity of these devices, modeling of their response to strain is not complete at this time. However, in this section, we present two important sets of empirical data on MISH diodes. The first is the C-V characteristics, which confirm the statements made above. The second is the measured capacitance change ΔC under strain as a function of bias. From this data, we can infer that the gauge factor (at optimum bias) of these devices is at least 500, and likely significantly larger.

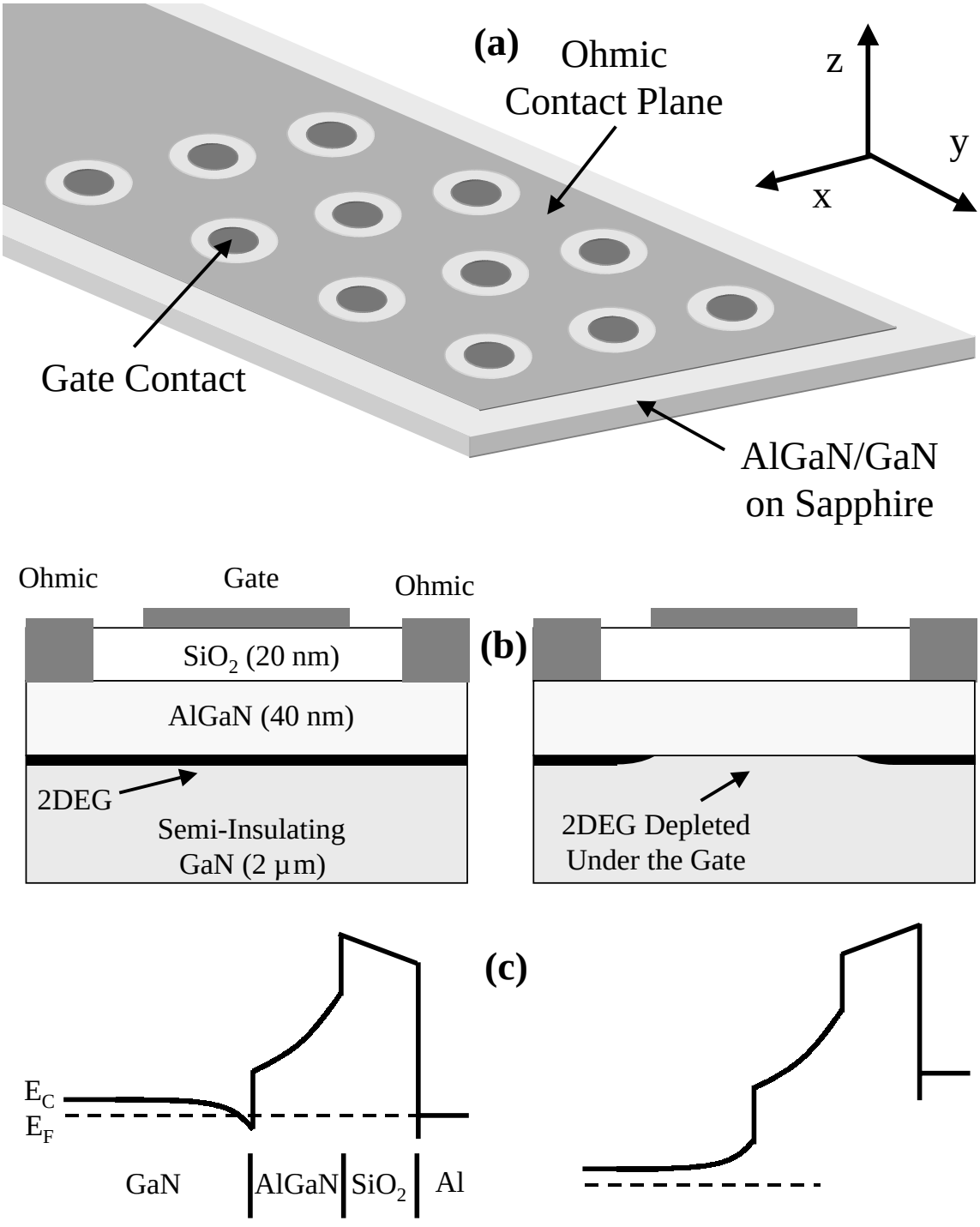

Figure 2.23: (a) Schematic of MISH diode array as laid out on the sample. (b) Side-view of MISH capacitor under no bias (left) and under reverse bias (right). Horizontal and vertical dimensions are not drawn to scale. (c) Schematic band diagram in both cases.

2.5.2 Device Characteristics

The MOCVD growth used here consisted of a 40 nm $Al_xGa_{1-x}N$ (x=30%) layer on a 2 μm semi-insulating GaN layer. The Si doping density in the upper layer is not known. The average sheet resistance of the film was 440 Ω; assuming an electron mobility of 1000 cm^2/Vs, this corresponds to a 2DEG sheet charge density in the range of $1.4\times10^{13}/cm^2$.

Fabrication proceeded as follows. At the outset, a Ti/Al/Ni/Au ohmic contact was sputter deposited and patterned (using lift-off) to have an array of 0.17 mm^2 circular holes. The remaining contact plane was subsequently annealed at 700° C in Ar for 60 seconds. Following this, 20 nm of PECVD SiO_2 was deposited over the entire sample area. At the last stage, circular Al gates (0.12 mm^2) were patterned to coincide with the (larger) holes in the ohmic plane. Fig. 2.23(a) shows a schematic of the resulting diodes as they were laid out on the sample.

A sideview of a MISH capacitor is seen in Fig. 2.23(b); note that horizontal and vertical dimensions are not drawn to scale. The schematic on the left corresponds to the equilibrium state, wherein the 2DEG at the heterojunction extends uniformly under the gate. Since the resistance of this sheet is low, the diode behaves like a parallel plate capacitor with two intervening dielectric layers, namely, the AlGaN and oxide layers. In this case, the entire circular gate area contributes to the overall capacitance of the device. The corresponding band diagram under the gate is shown below (Fig. 2.23(c)). Since the AlGaN layer above is fully depleted, and the GaN layer below is insulating, the hetero-interface is the only path for current flow. When the diode is biased in reverse, and the 2DEG begins to deplete under the gate, the resistance of this path grows. Ultimately, when the 2DEG is fully depleted (right side of Fig. 2.23(b)), the effective area of the MISH diode, and therefore its capacitance, is very small.

These plausibility arguments are confirmed by the impedance data shown in Fig. 2.24. For the two plots here, the impedance of the MISH diode is treated as a parallel capacitance and conductance. Note that the capacitance is flat for quite a range in

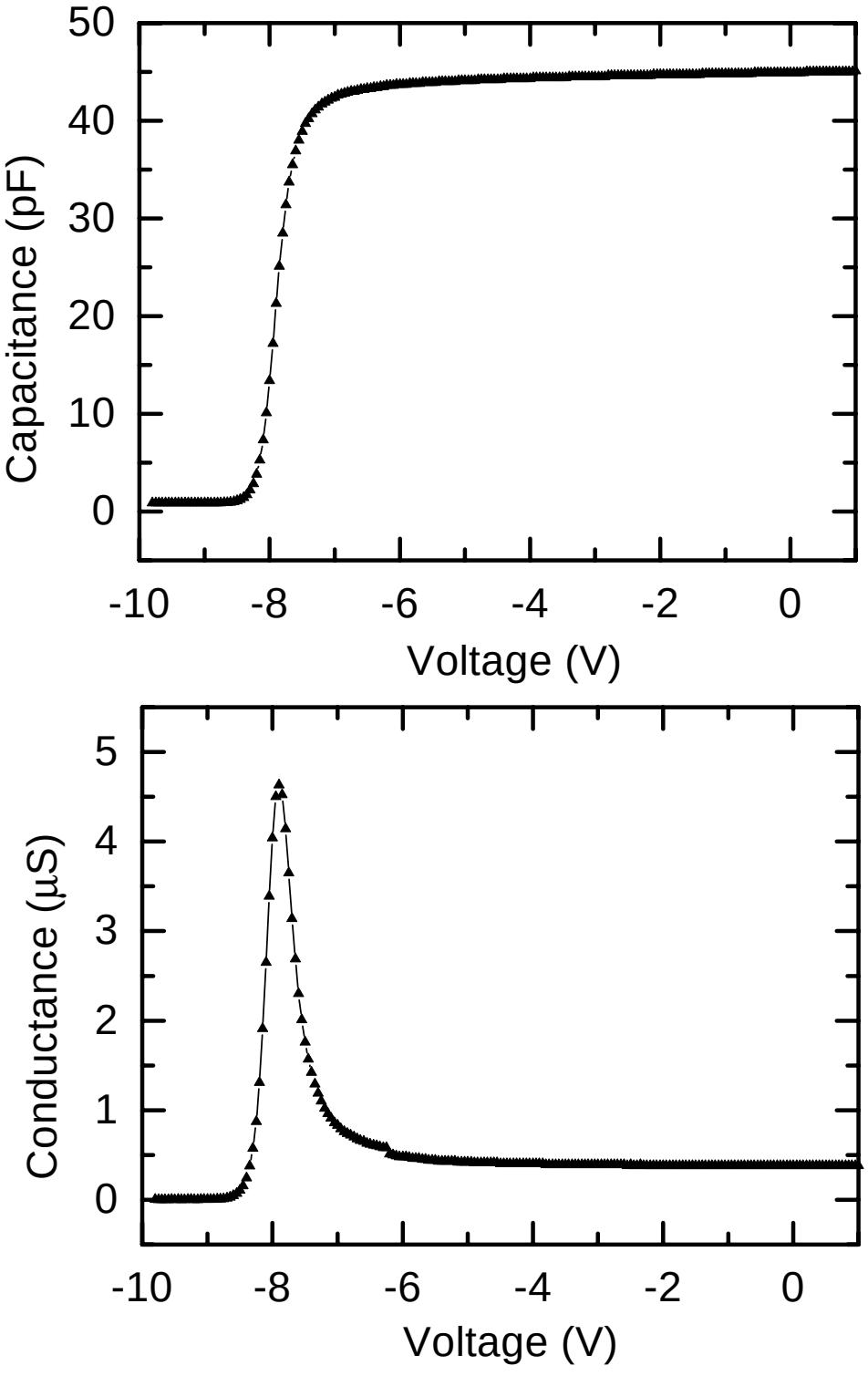

Figure 2.24: Room-temperature C-V and G-V characteristics for a 0.12 mm^2 MISH diode. The data was taken in the dark at a ramp rate of .01 V/s and a spot frequency of 100 kHz.

voltage, but then drops abruptly to near zero as the 2DEG becomes depleted. During this same transition, the conductance reaches a peak as a result of series resistance under the effective gate area.

2.5.3 Response to Strain

When a MISH capacitor is strained, the distribution of piezoelectric bound charge is more complicated than in an ordinary MIS diode. In addition to the usual sheet charges at either face of the layer, there will be a change in the bound charge at the heterojunction resulting from the different piezoelectric constants of the two materials. In addition, the assumption of no electric field in the GaN layer may not apply in this case owing to its semi-insulating nature. As a result of these theoretical complications, we have not yet derived a relationship between the strain and the free charge ΔQ which would flow between the terminals. Hence, measurement of ΔQ could not be used to calibrate the mean strain conditions in this experiment.

However, the capacitance change ΔC under strain was measured, and the averaged results are presented in 2.25. The data shown here was taken using exactly the same setup described in the previous section. During strain cycling, the capacitance of these devices did not exhibit drift or decay as caused by the charging of surface states. Though the fractional capacitance change (bottom of Fig. 2.25) attained a maximum of 3.3%, the optimal gauge factor can not be inferred without knowing the actual strain. However, the force applied by the transducer was known. Because the sample used in this experiment was significantly wider than that used previously, the induced strain (for the same force) is no greater than before. Based on these estimates, the lower limit for the optimal gauge factor of the MISH diode is 500.

2.5.4 Conclusions

While the preliminary data for MISH capacitive strain sensors seems rather promising, and the underlying premise of their operation was confirmed by empirical C-V data, further work is needed to both calibrate the gauge factor and model the device physics.

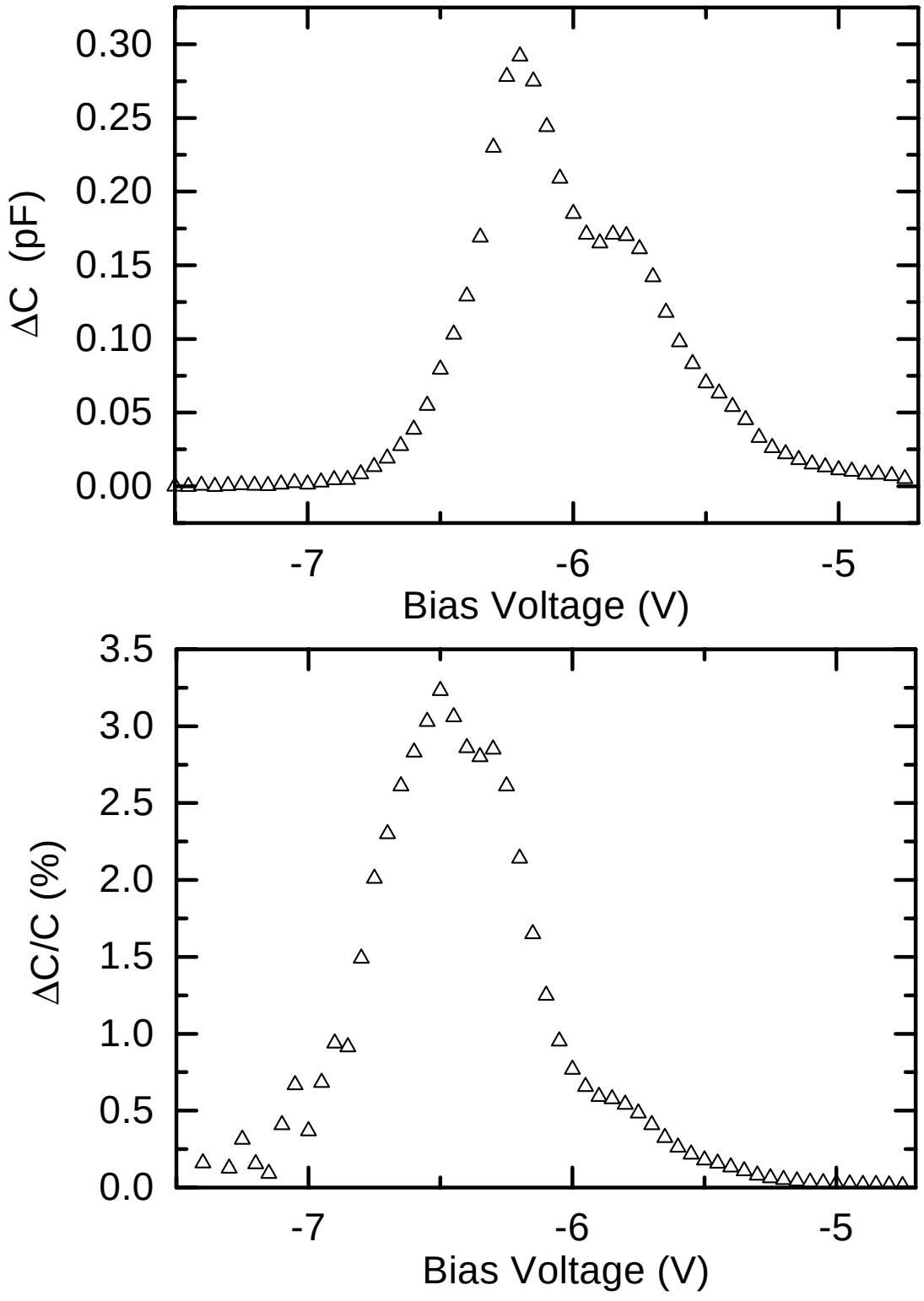

Figure 2.25: Measured capacitance change and fractional capacitance change for a 0.12 mm^2 MISH diode. The actual strain was not calibrated.

Furthermore, since these sensors will be operated at a bias with appreciable resistance (and hence thermal noise) under the gate, the noise characteristics must be studied to determine the overall strain sensitivity.

Bibliography

[1] E. Yu, X. Dang, P. Asbeck, S. Lau, and G. Sullivan, Journal of Vacuum Science and Technology B **17**, 1742 (1999).

Chapter 3 Fabrication of Suspended GaN Microstructures

3.1 Introduction

The following chapter describes two processes that were developed to fabricate suspended microstructures in both p-type and n-type GaN. Each process exploits a distinct electrochemical etch which is dopant selective, the two etches being complementary. In one process, a well-known photo-electrochemical (PEC) method was adapted to undercut p-GaN epilayers that were grown on top of n-type sacrificial layers. For the other, a novel anodic electrochemical etch was developed to undercut n-GaN layers. Both fabrication methods feature high dopant selectivity, rapid undercutting rates, and lateral etch anisotropy.

A graphic illustration of these methods is shown in Figs. 3.1 and 3.2. These figures outline a four step process, combining both etch techniques, in which a 2 mm $\times$ 2 mm area of n-GaN was lifted off its original growth substrate and bonded to a metallic base. The growth used here consisted of a n-type layer grown atop a p-layer. In the first step, opaque metal (Ni) squares were deposited on the sample surface. For reasons discussed below, these served as masks during the subsequent PEC etch step, after which all uncovered regions of the n-GaN layer were completely removed. The p-GaN layer, originally buried but now exposed, was then attacked using the anodic electrochemical etch; in short time, the masked n-GaN area was undercut to completion, and lift-off was thus achieved.

In the first part of this chapter, we offer a brief survey on wet etching in the nitrides, focusing on the chemical reactions and semiconductor electrochemistry which govern the two etches discussed above. The next section describes in detail the process developed to fabricate p-GaN microstructures. In addition to technical aspects of the procedure itself, data is presented on a wide range of devices which were fashioned in this way, including microfluidic pumps, piezoelectric strain sensors, and sub-micron scale beams. The final section deals with the fabrication of n-GaN devices. Though this process is currently less developed, we believe it will figure prominently in the future development of GaN MEMS. Here, the technical steps unique to the anodic etch are outlined, and data on n-GaN cantilevers with integrated piezoelectric transducers

is presented. At the end of this section, we demonstrate the use of anodic etching to create three-dimensional stratified MEMS devices in GaN.

3.2 Background

A characteristic of GaN which makes it attractive for MEMS applications in harsh environments is its unusually high chemical inertness. Though some authors have reported slow etching of GaN in either hot phosphoric acid [1] or highly basic NaOH solutions [2], these results were later attributed to poor material quality. To date, no wet chemistry acting alone has been found to reliably etch GaN [3].

However, Minsky *et al.* found that n-GaN could be etched rapidly using a photo-electrochemical (PEC) approach in an aqueous KOH solution [4]. Standard PEC etching of GaN is achieved by exposing it to above bandgap radiation while immersed in solution. It is believed that band-bending at the n-GaN/electrolyte interface causes photo-generated holes to be swept toward the surface where they participate in the chemical dissolution of the semiconductor [5]. Because this reaction is accompanied by a net flow of electrons to the semiconductor, an electrochemical cell configuration must be used to prevent charging of the sample. Numerous variations or refinements of this process have since been reported, including the use of alternative chemistries such as phosphoric acid [6] and the use of an anodic bias to increase the etch rate [7]. From careful studies of the photoanodic behavior of GaN during PEC etching [8], holes are thought to participate via the following reactions occuring at the surface:

$$GaN + 3h^+ \rightarrow Ga^{3+} + 0.5N_2 \tag{3.1}$$

for etching in H_3PO_4, and

$$GaN + 6OH^- + 3h^+ \rightarrow GaO_3^{3-} + 0.5N_2 + 3H_2O \tag{3.2}$$

for etching in KOH.

Significantly, PEC is found to not etch p-GaN. Youtsey *et al.* [5] suggested this

(I) Deposit Metal on n-p-i GaN

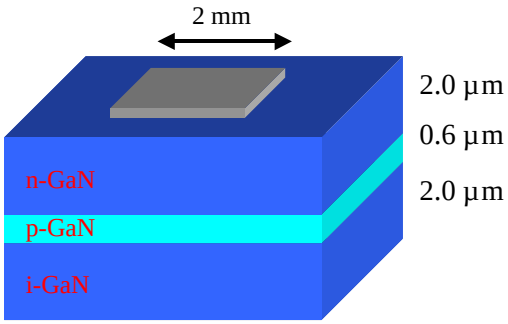

Schematic diagram of the epitaxial layers of the n-p-i GaN growth with 2 mm x 2 mm metal mask deposited on the surface.

SEM image of 100 nm Ni mask deposited on the GaN surface.

(II) PEC Etch

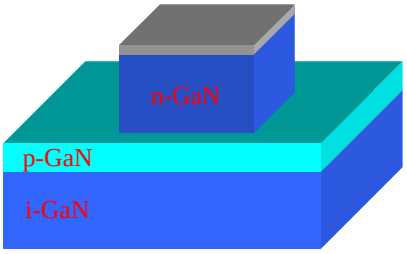

Schematic of the same structure following the PEC etch. The upper n-GaN layer is removed except under the opaque metal mask.

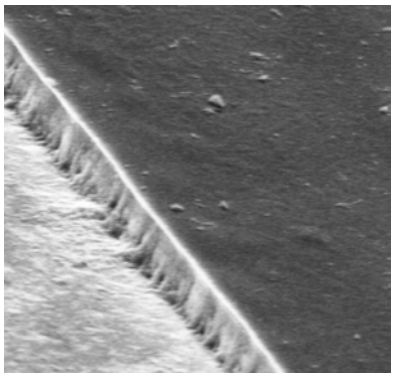

SEM image of a 2 µm sidewall following the PEC etch of the uppermost n-GaN layer.

Figure 3.1: Demonstration of PEC and anodic electrochemical etching.(Part 1/2)

(III) Anodic Electrochemical Etch

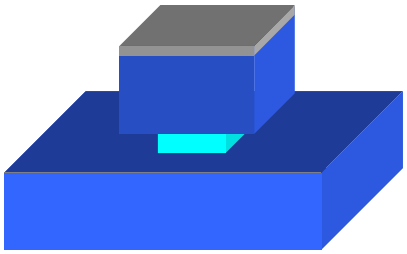

Schematic of the structure in the midst of anodic electrochemical etching. The upper n-GaN layer is undercut as the p-GaN layer etches away.

(IV) Bond to Metallic Substrate

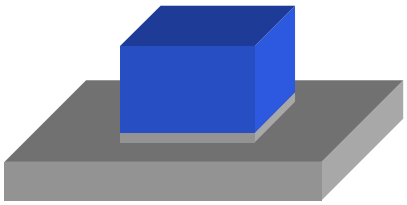

The entire n-GaN area is lifted-off the substrate and then bonded (Ni side down) to a separate metallic substrate.

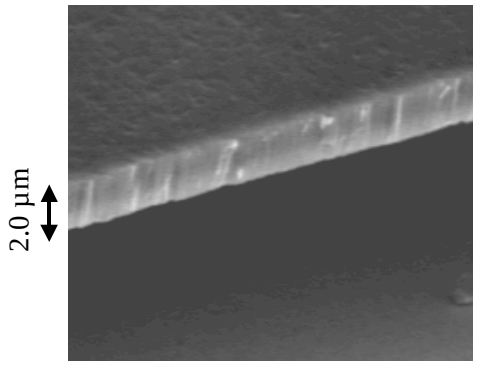

SEM sideview of the 2 µm undercut n-GaN layer.

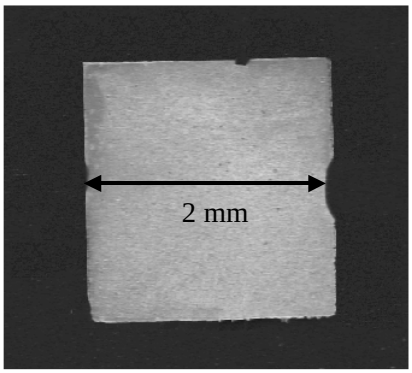

SEM topview of the 2 mm x 2 mm n-GaN area bonded to a metallic substrate after lift-off.

Figure 3.2: Demonstration of PEC and anodic electrochemical etching.(Part 2/2)

may result from an opposite sense to the band bending at the p-GaN/electrolyte interface, creating a barrier for the migration of holes to the surface. This picture was essentially confirmed by electrochemical impedance measurements which proved that a depletion layer does indeed form at the semiconductor surface with an almost Nerstian dependency of flatband potential on pH (-60 mV / unit pH) [8].

The dopant selectivity of PEC etching provides the means to undercut a p-GaN layer grown atop an n-GaN base; it is the cornerstone of the p-GaN MEMS fabrication process discussed in section 3.3. Though this process was conceived and developed in house, undercutting of p-GaN layers has been studied independently by other groups [5],[9].

Given the key role holes play in the etching of n-GaN, we speculated that electrochemical etching of p-GaN could be achieved by applying an anodic bias to the sample relative to solution. Given sufficient voltage, the p-GaN/electrolyte junction would become forward biased, pushing holes to the surface where they would participate in the dissolution of the semiconductor. This speculation was confirmed in a series of experiments which showed that p-GaN could be etched at almost arbitrarily high rates in KOH depending upon the bias applied. Anodic etching of this type was discovered concurrently by Borton *et al.* [10]. In the dark, it was found that n-GaN was highly resistant to this etch even though holes would likewise be drawn to the surface by the bias. This resistance is almost certainly caused by the negligible hole concentration in n-GaN resulting from the extremely low thermal minority carrier generation rate in this (wide bandgap) semiconductor. Hence, anodic etching is dopant selective in a manner exactly converse to PEC etching. As a result, it forms the cornerstone of the n-GaN MEMS fabrication process discussed in section 3.4.

3.3 Fabrication of Suspended p-GaN Microstructures

The process discussed in this section exploits the dopant selectivity of photo-electrochemical (PEC) etching to undercut p-GaN layers grown on sacrificial n-GaN layers. To fabricate complex microstructures in p-GaN, however, this undercutting must be precisely controlled and optimized. For one, etching must be prevented in regions of the n-type underlayer designed to provide mechanical anchoring for the p-type membrane above. Furthermore, for structures with a large undercut span, the lateral etch rate must be high to achieve a practical total etch time.

Fig. 3.3(a) shows the salient features of the etch setup used for controlled undercutting of p-GaN. In these experiments, p-on-n bilayer samples were immersed in either 0.1 M KOH or H_3PO_4 (pH 3) and exposed from the front side by a Xenon arc lamp with 100 mW/cm^2 in the UV ($\leq$365 nm). Prior to the PEC etch, opaque metal masks were patterned onto selected regions of the sample surface. Typically, these masks were then annealed ($\sim$300 °C for 5 minutes in Ar) to promote adhesion and thereby prevent subsequent peeling in the corrosive chemical bath.

As depicted in the Fig. 3.3, the n-type sacrificial layer does not etch in the areas immediately below the masks, allowing these regions to form mechanical anchors for the layer suspended above. However, masked regions near the outermost periphery of the overlayer were seen to undercut slowly as a result of stray UV radiation that is reflected back through the sapphire substrate directly into the n-GaN layer. To suppress this reflection, samples were not etched on a holder in solution, but were instead suspended in solution by a Ni wire epoxied on the GaN surface near an edge. This stray radiation could be effectively eliminated by using a backside polished substrate with a thin anti-reflection coating.

The Ni wire also served as the electrical contact to the GaN electrode of the electrochemical cell. It was maintained at a positive 0.5 V bias with respect to a Pt cathode in solution. The application of this bias was seen to dramatically accelerate the undercutting of the unmasked p-GaN areas, with lateral etch rates in excess of 30

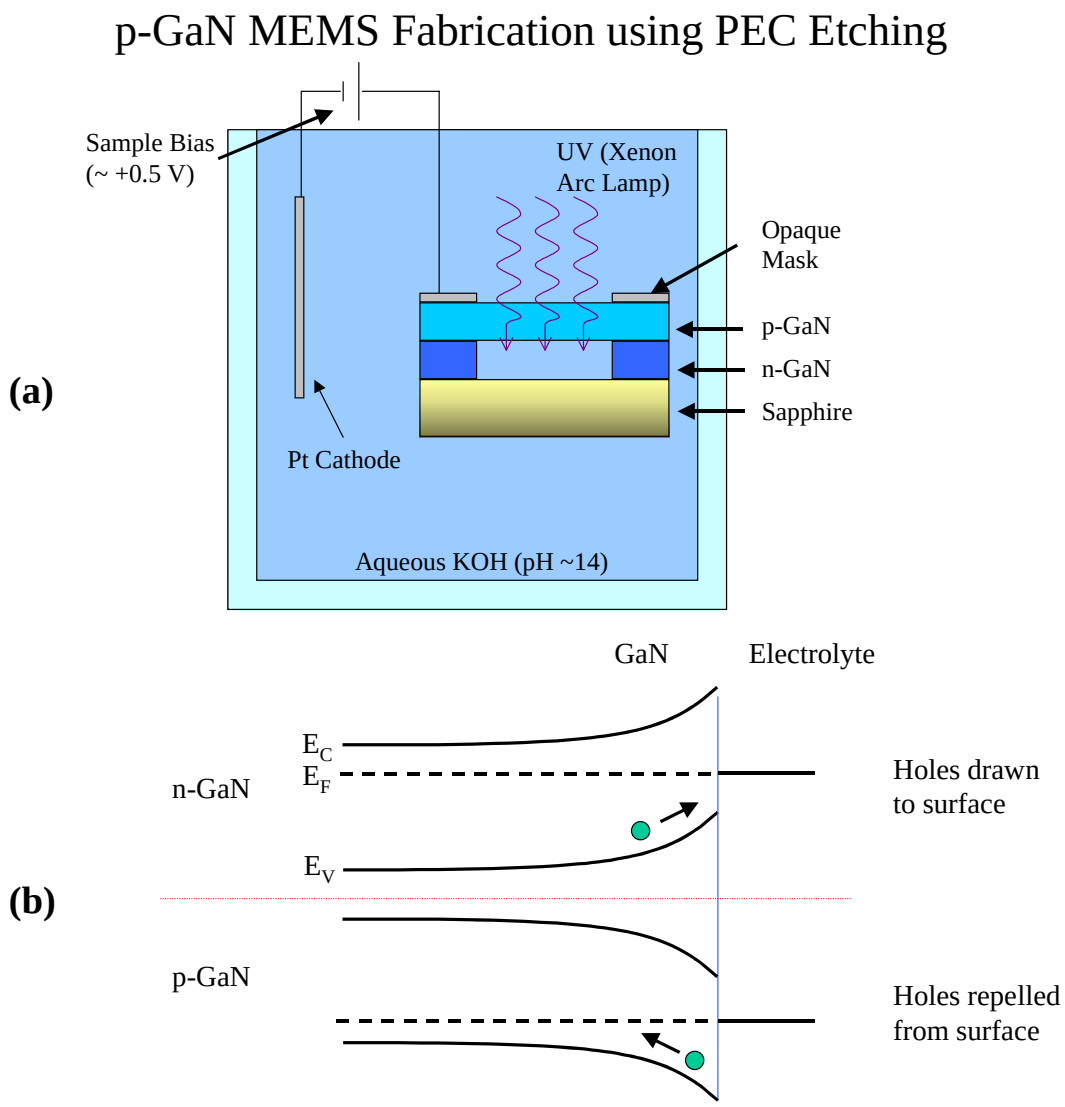

Figure 3.3: (a) Schematic of the PEC etch setup used to undercut p-GaN layers. (b) Schematic band diagram for both doping types when immersed in the electrolyte. Note that band bending attracts photogenerated holes to the surface in n-GaN, but repels them in p-GaN.

μm/min being observed for certain geometries. The origins of this marked increase in etch rate are not fully understood at this time. However, observations of the undercutting dynamics suggest that the sample bias gives rise to drift currents of the electrolyte within the narrow etched channels under the p-GaN film. These currents would deliver chemically active OH^- radicals to the etch front much more efficiently than diffusion alone.

Even with drift currents in the electrolyte, the high lateral etch rates achieved are surprising given the large optical thickness of the p-GaN layers in our experiments. Using values for the optical attenuation constant $\alpha(\nu)$ [11] of undoped GaN and the intensity spectrum of the Xenon arc lamp, we calculate that only 2% of the total optical absorption will occur in the n-GaN below a 1.0 μm p-layer. The resulting hole generation rate in the n-layer is most likely not enough to sustain the etch rates observed. Instead, we believe that holes are injected from the p-layer above as the result of a light-induced forward biasing of the p-n junction. Like holes that are directly photogenerated in the n-layer, these injected holes are subject to recombination there: roughly speaking, those within a diffusion length L_p of the electrolyte interface will reach the surface to participate in PEC etching.

When a bilayer sample is exposed to UV radiation from the frontside, e-h pairs are created predominantly in the top p-layer. Minority carrier electrons which reach the edge of the depletion region are swept away by the built-in fields at the junction, giving rise to a photo-electron current J_{pe} from the p-layer into the n-layer. In the steady-state, the potential drop across the junction is reduced to compensate for this current. In this forward biased configuration, a hole diffusion current $J_{d,h}$ flows over the potential barrier from the p-layer into the n-layer, while an electron diffusion current $J_{d,e}$ flows in the opposite sense. Without any flow of charge between the electrolyte and the sample [12], these currents must cancel the photogenerated electron current: $J_{pe} + J_{d,h} + J_{d,e} = 0$. Ignoring surface recombination on the frontside of the p-layer [13] (as well as recombination in the depletion region), the hole current injected into the n-type layer follows from the standard theory of a p-n junction solar

cell [14]:

$$J_{d,h} = F\Big(\frac{\alpha^2 {L_n}^2}{\alpha^2 {L_n}^2 - 1}\Big)\Big(\frac{\mu_{p,m} p_0}{\mu_{p,m} p_0 + \mu_{n,m} n_0}\Big)\times \Big[e^{\Delta x_p / L_n} - e^{-\alpha \Delta x_p} - \tanh\Big(\frac{\Delta x_p}{L_n}\Big)\Big(\frac{e^{-\alpha \Delta x_p}}{\alpha L_n} + e^{\Delta x_p / L_n}\Big)\Big] \tag{3.3}$$

where p_0 and n_0 are the majority carrier concentrations in each layer, $\mu_{p,m}$ and $\mu_{n,m}$ are the minority carrier mobilities, L_n is the electron minority carrier diffusion length, Δx_p is the p-layer thickness, and F is the incident photon flux. In the regime $1/\alpha < L_n < x_p$, $J_{d,h}$ decays with the p-layer thickness like $\exp(-\Delta x_p / L_n)$, while the light intensity decays much more sharply like $\exp(-\alpha \Delta x_p)$. For this reason, diffusion becomes the primary source of holes in the n-layer. This argument is strengthened by recent reports of large values for L_n after extended periods of minority carrier injection in p-GaN [15]. Using $L_n = 0.5 \mu m$ [15], $\mu_{p,m} = 5$, $\mu_{n,m} = 0.12\ cm^2/Vs$ [16], and integrating over the spectrum of the light source, it is calculated that the hole diffusion current density dominates the hole photogeneration rate per unit area in the n-layer by a factor of 10:1 for a 1.0 μm p-type overlayer.

Fig. 3.4 shows an assortment of conventional MEMS device geometries that were fabricated in p-GaN with the PEC process described above. The intent of these devices was mainly to explore and refine the etch process. In all three cases, the following general recipe was used:

(1) **Deposit metal**: In this step, metal is sputter deposited on selected areas of the GaN surface. These metal areas will later serve as opaque masks for the PEC process; therefore, they delineate the regions of the device which will remain anchored to the sapphire substrate. The choice of metal must be compatible with the PEC chemistry: Ni, Au, Pt and Ti are all robust in KOH. As mentioned earlier, the masks are typically annealed at low temperature to promote adhesion to the GaN surface.

(2) **CAIBE etch**: In the first part of this process, conventional lithography is used to pattern a layer of photoresist to cover only those regions of the p-layer

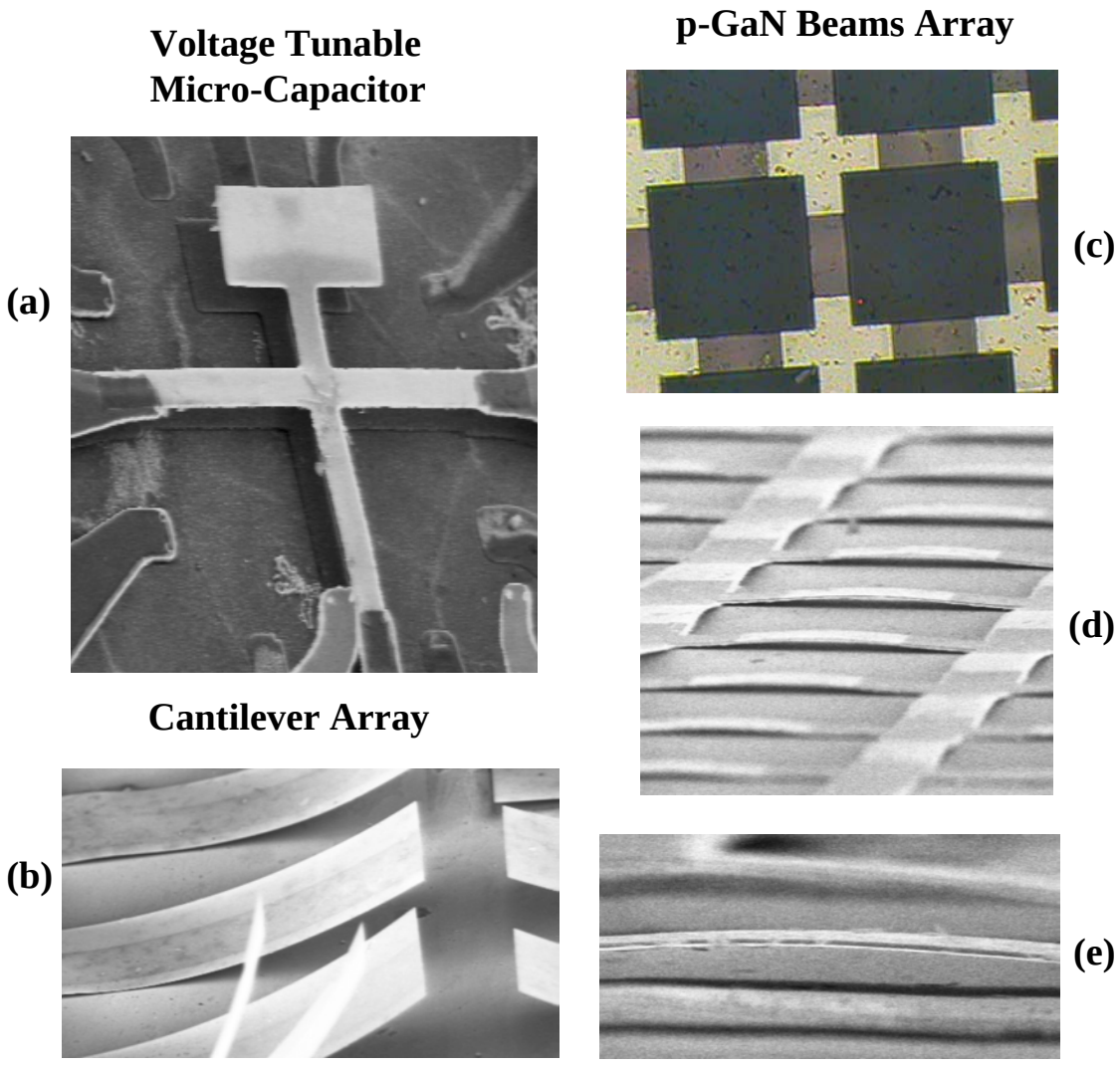

Figure 3.4: (a) SEM image of a voltage tunable micro-capacitor. (b) SEM image of an array of cantilevers. (c) Optical image of a lattice of beams; the beams (light grey) span between the Pt coated supports (bright crosses). (d) SEM sideview image of the same lattice showing bowing of the beams. (e) SEM sideview of a 1 μm thick arched beam.

which will later comprise the device. Following this, chlorine-assisted ion-beam etching (CAIBE) is used to etch down through the uncovered regions, ultimately exposing the underlying n-GaN layer.

(3) **PEC etch**: At this stage, the sample is subjected to the PEC etch process described in length above. The exposed n-GaN regions etch away rapidly, forming the entry points for the subsequent undercutting of the unmasked p-GaN areas.

(4) **Cleaning**: After the PEC step, undercut p-GaN regions with large spans are typically found adhered to the sapphire surface. In most cases, stiction can be remedied by several cleaning cycles in which the sample is alternately soaked in hot deionized water and then isopropanol.

For the beams array and the cantilever array (shown on the right and bottom left of Fig. 3.4, respectively), the GaN sample was grown in house by molecular beam epitaxy (MBE) and consisted of 1 μm p-GaN on 1 μm n-GaN. For the voltage tunable micro-capacitor (Fig. 3.4(a)), the growth consisted of 0.6 μm p-GaN on 0.8 μm i-GaN. Note that bowing or bending of the freestanding p-GaN membrane is evident in all three structures; in particular, the cantilevers relax into a shape which is uniformly curved away from the substrate. This curvature suggests there are vertical stress gradients built into the p-layer during growth that result from crystallographic defects.

Another example of the diverse microstructures which can be realized using the PEC etch process is the GaN microfluidic channel shown in Fig. 3.5. The microchannel consists of an 1 μm thick p-GaN membrane that spans between two long anchoring strips on either side. The $(0, 0, 0, \bar{1})$ GaN layers used here were grown by MBE on c-plane sapphire. Both the n^+ (Si) and the p^+ (Mg) epilayers are $1\mu m$ thick. Both are thought to have carrier concentrations in the range of $10^{18}/\text{cm}^3$ based on Hall measurements of similar samples. To fabricate this microchannel, a series of Ni bars with 100 μm spacing were patterned on the sample using standard lithographic techniques. The sample was then exposed to the PEC etch, during which the unmasked

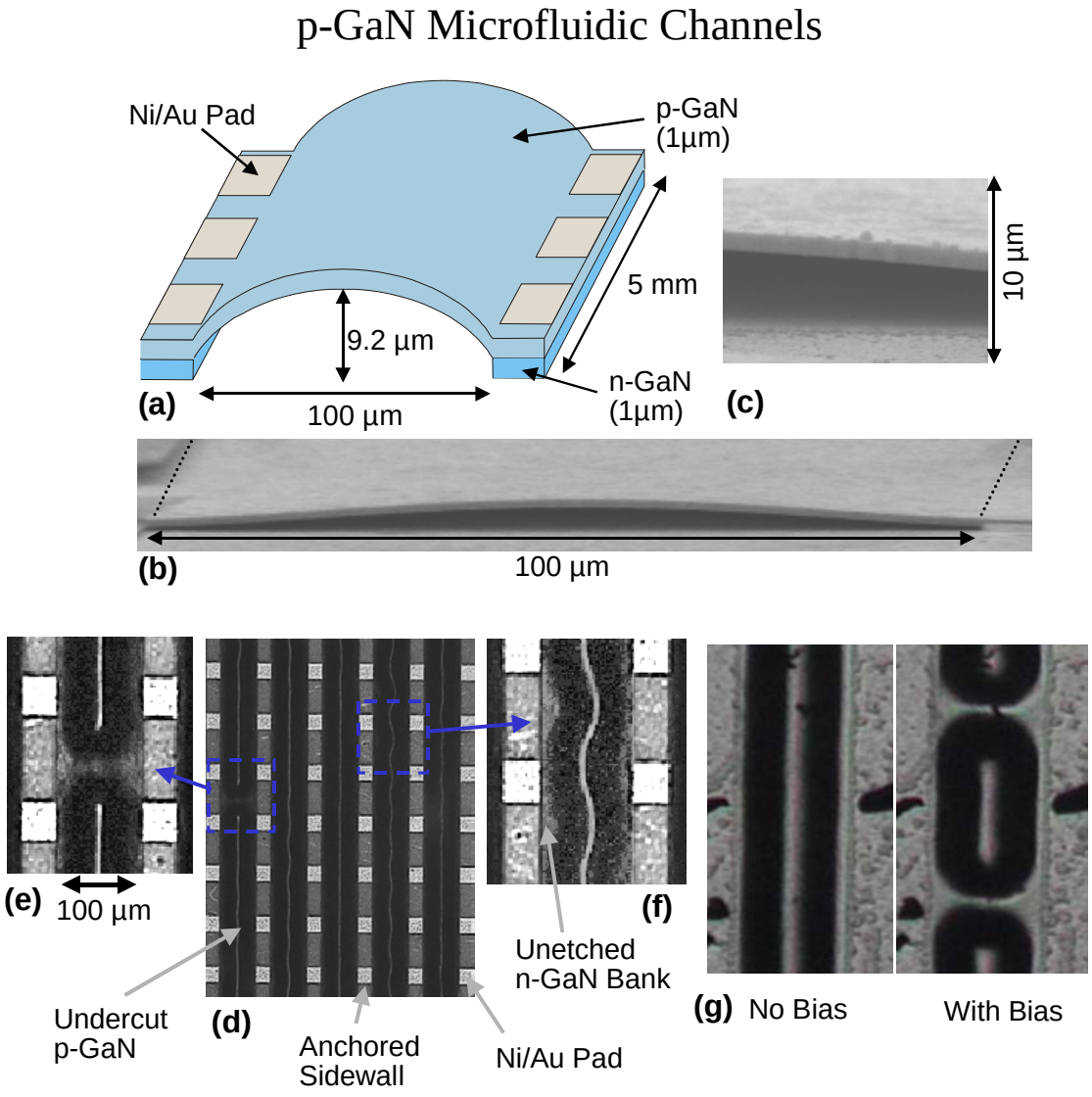

Figure 3.5: (a) Schematic diagram of a p-GaN microfluidic channel; dimensions are not drawn to scale. (b) SEM sideview of the entrance of a channel showing the bowing of the suspended film. (c) Expanded view of the same entrance showing the 1 μm thick p-GaN film. (d) Topview microscope image of a series of microchannels before etching is complete. Dark regions correspond to the undercut p-GaN channels. Narrow bright lines in the middle of the channels are glints from the bowed surface. (e) Expanded view of a region in the channel where two advancing etch fronts have not yet merged. (f) Expanded view showing residual unetched n-GaN banks in the channel. (g) Top view showing buckling of the membrane when a voltage is applied across opposing contact pads.

regions between the bars were undercut. Etching of n-GaN underlayer proceeded inward from both sides in the direction of the bars. A total undercut channel length of 5 mm etched to completion in roughly 2 hours. Afterward, the Ni bars were removed, exposing a series of isolated Au contact pads along the anchored sidewalls.

The surface quality of the p-type film does not appear to degrade as a result of the lengthy PEC etch. Furthermore, the underside of the suspended p-GaN film is smooth and featureless. This is in marked contrast to our observations of p-on-n samples grown by MOCVD, for which the undersides are rough and coated with etch-resilient whiskers.

As seen in the scanning electron microscope (SEM) sideview image of Fig. 3.5(b), the p-GaN membrane bows upward after release to relieve internal stress. A maximum vertical deflection of 9.2 μm is measured at the center of the 100 μm channel width, corresponding to a $\sim$2.2% increase in the area of the p-GaN membrane after release. The magnitude of this expansion can not be explained by the thermal contraction mismatch between GaN and sapphire, and therefore suggests the presence of vertical stress gradients within the epilayer.

Fig. 3.5(e) is a top-view optical microscope image of a series of micro-channels that have not fully etched to completion. The dark bands correspond to regions where the p-GaN is undercut and bowed. The lighter strips are regions still anchored by the n-type underlayer. Except for the square contact pads, the metal masks were completely removed after the PEC etch. As is evident from the image, the masks served to prevent undesired undercutting at the sidewalls. Fig. 3.5(d) highlights a region where two advancing etch fronts have not yet merged. Fig. 3.5(f) shows areas of unetched n-GaN in an unmasked region. This n-GaN remains in the form of banks on the sides of the channel, causing the etched passageway to take on a serpentine profile. As the etch proceeds further, these channel residuals disappear, leaving uniformly straight sidewalls. However, the serpentine nature of the fluid passageways is a hallmark of the initial rapid etch dynamics brought on by a sample bias during PEC. As mentioned earlier, we believe this bias gives rise to drift currents in the undercut channels. When the etch front approaches a resilient sidewall, these

fluid currents rebound off the obstacle and initiate further etching at a reflected angle. In this way, the etched passageway will tend to wind back and forth between the masked sidewalls.

By applying a voltage across a pair of opposing metal contacts along the length of a microchannel, the suspended p-GaN membrane can be made to buckle from thermal expansion in the intervening region. This buckling is seen in Fig. 3.5(g), which shows a section of the microchannel both before and after the voltage was applied. Sequential actuation of the film in this manner will induce a peristaltic wave motion along the length of the channel which could be used for fluid pumping.

An early attempt at a deformable strain sensor in GaN is the piezoresistive strain gauge seen in Fig. 3.6. This device employed a suspended section of p-GaN acting as an electrical pathway between two anchored contact pads. The strain induced resistance change of this pathway ΔR was measured using a standard Wheatstone bridge configuration (shown in the lower left of Fig. 3.6). The fractional resistance change is charted in time at the lower right of the figure; during this span, the suspended section was fully depressed at the tip and then released for several cycles. As is evident from this chart, the signal, even under full range deflection, exhibits low margins over the background noise. The original impetus for this sensor design was the report of a large piezoresistive gauge factor (260) for p-GaN measured by Gaska *et al* [17]. As discussed in Chapter 2.2, we have determined that the effect observed by these authors was in fact piezoelectric and not piezoresistive in nature. By causing an exchange of free carriers with surface depletion regions, piezoelectric effects can change the sheet resistance of a p-GaN film. However, the fractional resistance change only becomes appreciable for very small ($\leq 100\ nm$) layer thicknesses. In chapter 4, data is presented on more sophisticated strain sensors which integrate piezoelectric transducers explicitly.

As a final demonstration of the versatility of the PEC process, Fig. 3.7 shows a collection of suspended p-GaN structures with characteristic lateral dimensions around 1 μm. In fact, the width of the narrowest beams seen in the figure is 600 nm. To fabricate features on this length scale, a combination of e-beam lithogra-

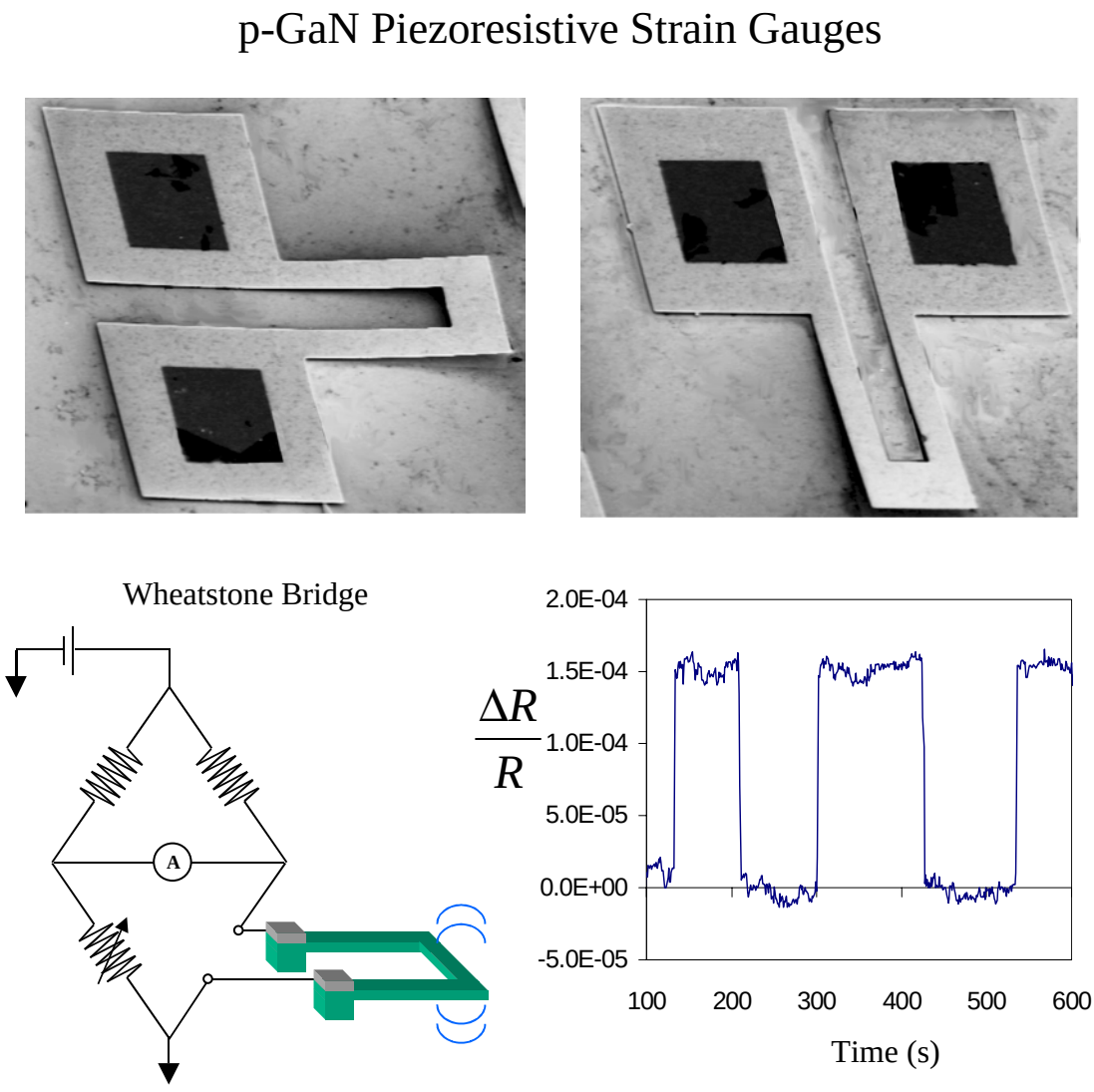

Figure 3.6: [Top]: SEM images showing two views of a p-GaN piezoresistive strain sensor fabricated using the PEC process. [Bottom Left]: Wheatstone bridge circuit used to measure the resistance change of the sensor under strain. [Bottom Right]: Measured fractional resistance change as the sensor is alternately depressed and released.

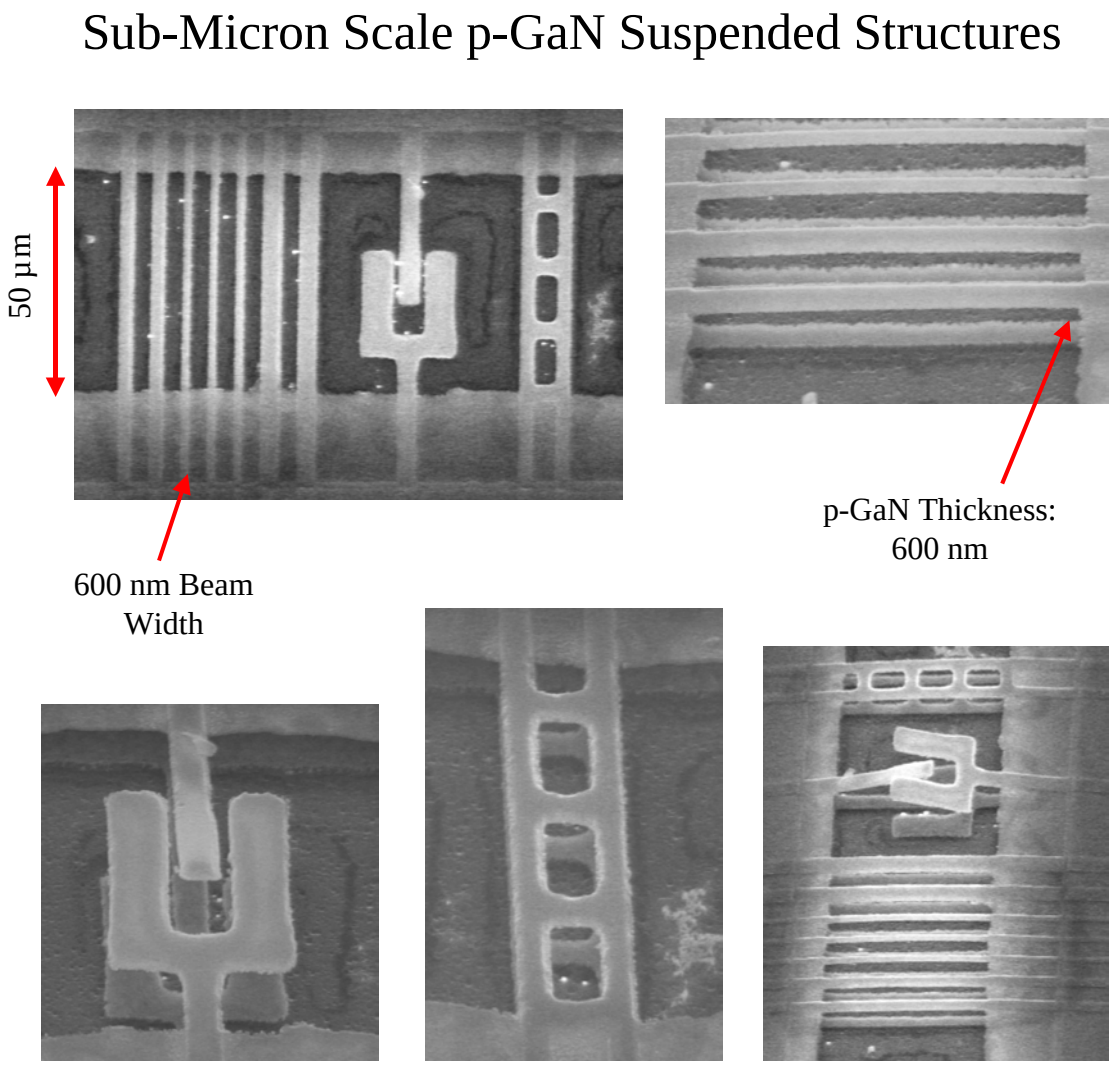

Figure 3.7: SEM images of a series of p-GaN structures suspended between two half-plane supports. The smallest beamwidths are 600 nm.

phy followed by lift-off was used to define metal masks (200 nm Ni) over the regions which would later be suspended. The CAIBE etch proceeded as normal, the GaN having a 5:1 etch selectivity over Ni. Following this, the metal masks were removed in dilute HF/H_2O_2 and the sample was then etched photo-electrochemically. The attainment of sub-micron lateral dimensions with the PEC process is significant because it demonstrates that GaN, as a sensor platform, can be readily extended into the realm of nano-electromechanical systems (NEMS).

3.4 Fabrication of Suspended n-GaN Microstructures

The last section outlined a p-GaN fabrication technology and showed how it could be used to create a diverse range of MEMS structures. However, a fundamental weakness of this process is that the suspended sections must be p-type. Due to the depth of the Mg acceptor level, it is difficult to achieve high hole concentrations in p-GaN without serious degradation of the crystal quality. Lowly doped material is also difficult to attain due to compensation by the high background (10^{17} / cm^3) of donor-like defects native to GaN.

Viewing the nitrides as a platform for MEMS, it is therefore critical that suspended microstructures can be fashioned in n-GaN as well. At the present time, n-type material exhibits electrical and material properties that are far superior to its counterpart. It can be controllably doped to levels as low as ($10^{16}/cm^3$), a fact which has great bearing on the sensitivity of piezoelectric transducers. Perhaps most importantly, n-type is the doping of choice for the well developed GaN/AlGaN heterostructure technology; integrating two-dimensional electron gases into GaN MEMS would greatly increase the functionality and frequency of operation of these sensors.

As mentioned earlier, we developed an anodic electrochemical etch which is highly selective of p-GaN. A clear demonstration of the dopant selectivity of this etch is shown in Fig. 3.8. The MBE growth seen in sideview at the upper left of the figure

consists of a 200 nm p-GaN layer sandwiched between two n-type layers. A view of the same sample after a brief period of anodic etching is seen in the upper right; here, the thin p-layer has etched away, leaving a narrow void between the still intact n-layers. The image at the bottom of Fig. 3.8 provides a cutaway view of the same etched sample. Here, a portion of the upper layer was broken off, revealing the surface of the bottom n-GaN layer which is smooth despite the etch.

Fig. 3.9(b) gives a schematic diagram of the band-bending at the GaN/electrolyte interface for both doping types under anodic bias. For p-type doping, the positive bias applied to the semiconductor lowers the electrostatic barrier height of the depletion region, allowing holes to diffuse toward the surface. For n-type material, the bias adds to the band bending, increasing the electric field which would drive holes to the surface; no etching is observed, however, because there are no holes in the bulk which can enter the depletion region. Provided etching occurs in the dark (to avoid minority carrier photogeneration), the validity of this assumption should hold even if the n-GaN layer has intimate contact with a p-type layer. In this case, both layers will experience the same bias with respect to the solution, but no net bias with respect to each other; hence, there will be no thermodynamic force to cause the flow of majority carrier holes into the n-type layer.

As shown in Fig. 3.9(a), anodic etching of GaN was performed in a standard electrochemical cell with a Pt mesh cathode and a potentiostat to regulate the bias between the sample and the solution (as measured by a Pt reference electrode). In our experiments, the bias was set in the range of 3.5 to 4 V positive with respect to the solution, the higher biases being used for samples with larger undercut span. In our experiments, either KOH (pH 14) or H_3PO_4 (pH 3) was used for the electrolyte.

As depicted in Fig. 3.9(a), samples were partially submerged in the electrolyte, and electrical contact was made through an ohmic contact pad on the dry side. Anodic etching occurred only on the submerged side of the sample. The reasons for this suspension are twofold. At the biases in use, if metals (at the potential of the anode) are not insulated from the solution, significant current will be sourced through the cell, leading to a spatial variation in the voltage drop between the semiconductor and

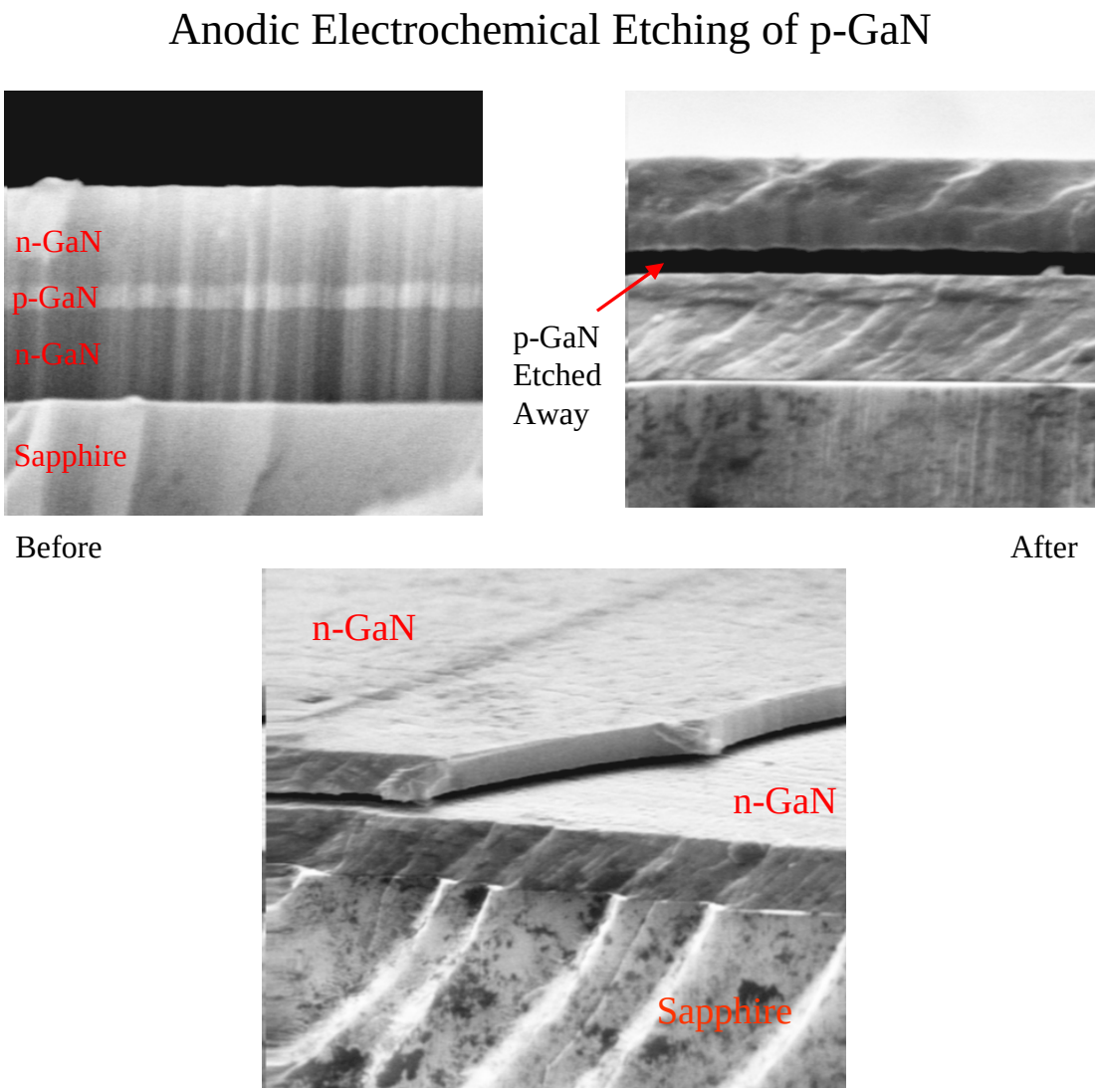

Figure 3.8: [Top]: SEM sideview images of an n-p-n GaN sample both before and after anodic electrochemical etching. [Bottom]: SEM cutaway view of the same sample after etching, revealing a smooth surface to the bottom n-GaN layer despite the etch.

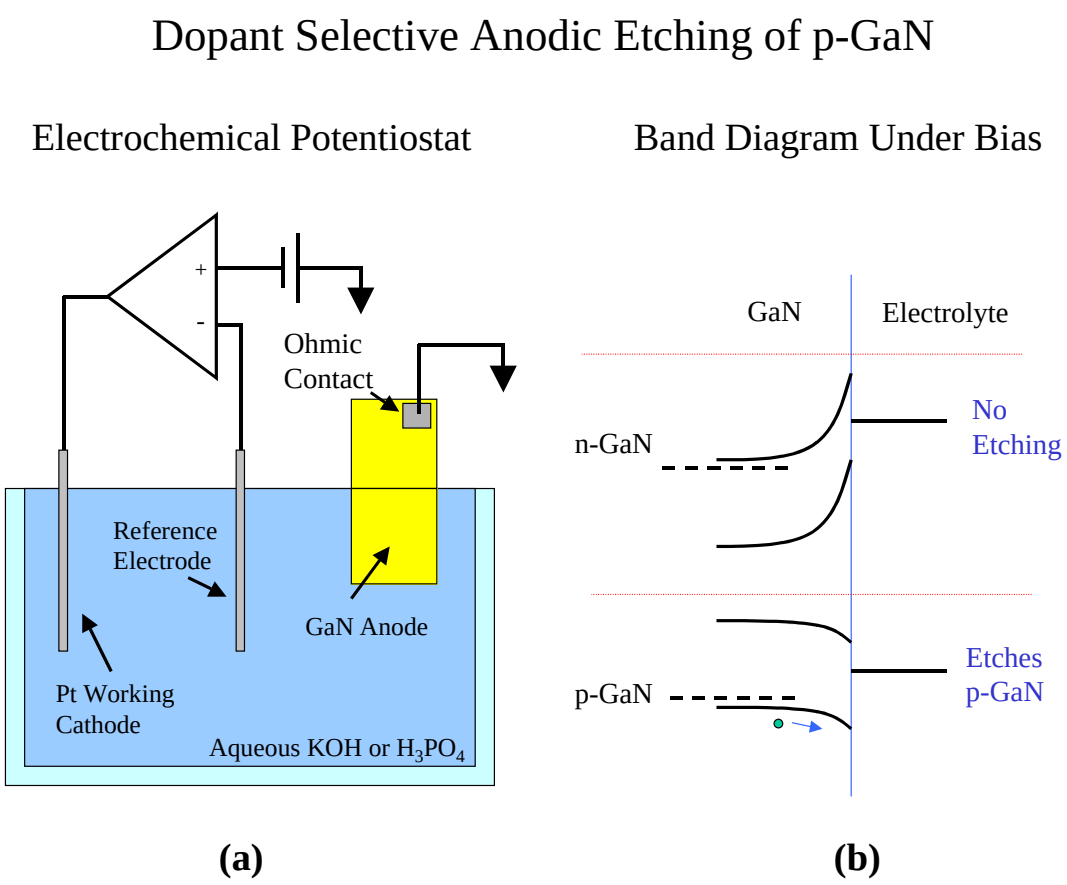

Figure 3.9: (a) Schematic of the setup used to perform anodic etching of p-GaN. The electrochemical cell consists of a GaN anode, a Pt mesh cathode, and a standard potentiostat to regulate the bias between the anode and the solution. (b) Band-bending at the GaN/electrolyte interface under anodic bias; holes are pushed toward the surface in p-type material, but none exist in n-GaN.

the electrolyte. Moreover, most metals etch rapidly under these conditions, and even highly inert Au and Pt suffer visible discoloration. For the same reasons, any exposed metal on the submerged side of the sample must be free to float at the potential of the solution. Both MIS and Schottky contacts, with their large dc blocking resistance, are permissible in this regard. For MEMS devices which required an ohmic (or leaky Schottky) contact, we developed two strategies to insulate the metal surfaces from the electrolyte: for etching in KOH, the metals were covered by a $\sim$100 nm Si_3N_4 layer grown by plasma-enhanced chemical vapor deposition; for etching in H_3PO_4, they were covered by Shipley 1813 photoresist.

With the preceding caveats in mind, fabrication of suspended n-GaN microstructures follows the same basic recipe discussed before with anodic etching simply replacing PEC etching. Fig. 3.10(a) shows an SEM image of the base of a n-GaN cantilever that was created using this process. The 300 μm width of the cantilever undercut to completion in approximately 30 minutes using an anodic bias of 3.5 V. Fig. 3.10(b) gives an enlarged view of the device, revealing the smoothness of the n-GaN surface despite direct exposure to the etch. Cantilevers of this type, fashioned in n-GaN with integrated piezoelectric transducers, will be discussed at length in Chapter 4.

The images at the bottom of Fig. 3.10 demonstrate an important extension of GaN MEMS that is enabled by anodic etching. Shown there is an MBE growth containing two thin p-type epilayers (200 nm) embedded in a n-type matrix. After brief anodic etching, both p-layers were seen to etch away, leaving a stack of suspended n-GaN layers. By adding more intervening p-layers at the time of growth, the number of strata in such a stack could be made arbitrary large. Furthermore, we believe the spacing between the strata could be very small. Roughly speaking, the minimum spacing is set by the thickness at which the sacrificial layers become fully depleted of holes; for doping at 10^{18} /cm^3, this distance is on the order of tens of nanometers. Stratified microstructures are a unique capability of the anodic etch; PEC etching could not achieve complementary results in p-GaN because strong UV absorption in the topmost layers would starve the etch below. By adding an important third dimension to the design of micro-devices, anodic etching opens the door for dramatic

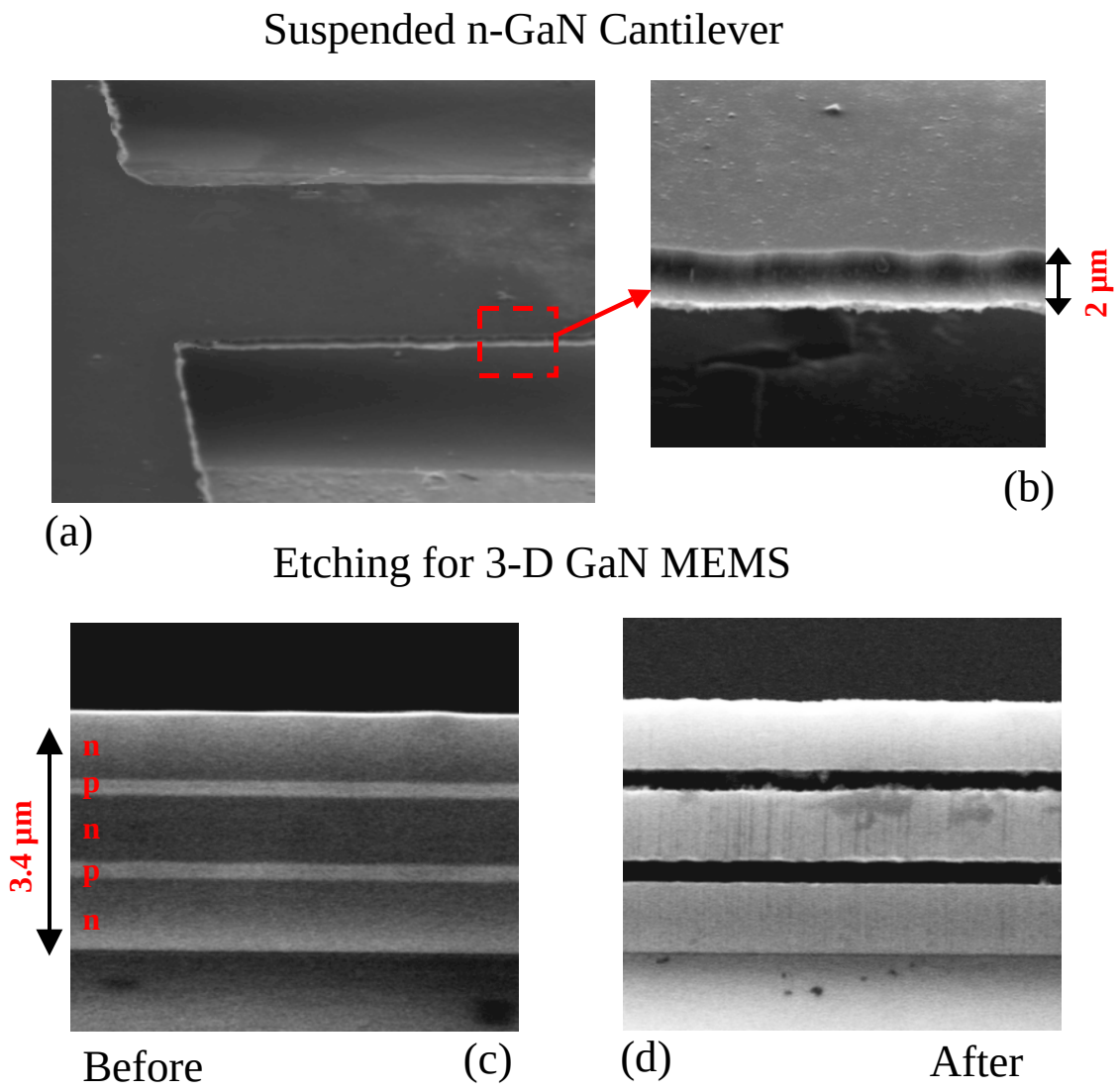

Figure 3.10: (a) SEM image of the base region of a 300 μm wide n-GaN cantilever that was fabricated using anodic etching. (b) Expanded view of the edge of the 2 μm thick cantilever. (c) SEM sideview image of a n-p-n-p-n GaN sample grown by MBE. (d) Image of the same sample after a brief anodic etch. The sacrificial p-type layers have etched away, leaving a vertical stack of suspended n-GaN layers.

enhancements in the overall functionality of GaN MEMS.

3.5 Conclusions

In summary, two fabrication technologies have been described which allow for the creation of MEMS devices in both p-type and n-type GaN. Both utilize a dopant selective electrochemical etch which hinges on the presence of holes at semiconductor/electrolyte interface. For p-type devices, the PEC process is fairly mature, having demonstrated a diverse range of microstructures including microfluidic pumps, piezoelectric strain sensors, and sub-micron scale beams. For n-type devices, the anodic etch process is less developed. However, given the superiority of n-type material (and the possibility of three-dimensional structures), anodic etching is likely to play a leading role in the advancement of GaN MEMS.

Bibliography

[1] A. Shintani and S. Minagawa, Journal of the Electrochemical Society **123**, 706 (1976).

[2] S. Pearton, C. Abernathy, F. Ren, J. Lothian, P. Wisk, and A. Katz, Journal of Vacuum Science and Technology A **11**, 1772 (1993).

[3] J. Mileham, S. Pearton, C. Abernathy, J. MacKenzie, R. Shul, and S. Kilcoyne, Journal of Vacuum Science and Technology A **14**, 836 (1996).

[4] M. Minsky, M. White, and E. Hu, Appl. Phys. Lett **68**, 1531 (1996).

[5] C. Youtsey, G. Bulman, and I. Adesida, Journal of Electronic Materials **27**, 282 (1998).

[6] L. Peng, C. Chuang, J. Ho, C. Huang, and C. Chen, Applied Physics Letters **72**, 939 (1998).

[7] H. Cho, K. Auh, J. Han, R. Shul, S. Donovan, C. Abernathy, E. Lambers, F. Ren, and S. Pearton, Journal of Electronic Materials **28**, 290 (1999).

[8] I. Huygens, K. Strubbe, and W. Gomes, Journal of the Electrochemical Society **147**, 1797 (2000).

[9] A. Stonas, P. Kozodoy, H. Marchand, P. Fini, S. DenBaars, U. Mishra, and E. Hu, Appl. Phys. Lett **77**, 2610 (2000).

[10] J. Borton, C. Cai, M. Nathan, P. Chow, J. Van Hove, A. Wowchak, and H. Morkoc, Applied Physics Letters **77**, 1227 (2000).

[11] G. Yu, G. Wang, H. Ishikawa, M. Umeno, T. Soga, T. Egawa, and J. Wa-tanabe, Appl. Phys. Lett **70**, 3209 (1997).

[12] From measurements of the impedance of the GaN/KOH interface, we find that the current density flowing between the sample and solution during the etch is very small in comparison to J_{pe}. Hence, we believe the electrolyte does not significantly alter the basic open-circuit condition.

[13] Band-bending at the electrolyte interface repels holes and thereby suppresses surface recombination.

[14] S. Sze, *Physics of Semiconductor Devices*, 2nd ed. (John Wiley & Sons, Inc., New York, NY, USA, 1981).

[15] L. Chernyak, A. Osinsky, V. Fuflyigin, and E. Schubert, Appl. Phys. Lett **77**, 875 (2000).

[16] Z. Guan, J. Li, G. Zhang, S. Jin, and X. Ding, Semiconductor Science and Technology **15**, 51 (2000).

[17] R. Gaska, M. Shur, A. Bykhovski, J. Yang, M. Khan, V. Kaminski, and S. Soloviov, Appl. Phys. Lett **76**, 3956 (2000).

Chapter 4 Integration of Piezoelectric Transducers on Suspended GaN Microstructures

4.1 Introduction

The second chapter of this manuscript discussed two classes of strain transducers in GaN which exploit the unique combination of large piezoelectric activity with conventional semiconductor properties. The third chapter presented a versatile process for fabricating suspended, deformable microstructures in both p-type and n-type GaN. This, the final chapter, will concern itself with the union of these two technologies. In particular, we will present data and modeling of simple cantilevers, fashioned in n-GaN, with integrated Schottky and MIS piezoelectric transducers. For this integration, cantilevers were chosen for their simplicity and because they have been studied extensively in other material systems, providing a standard by which GaN can be evaluated in the MEMS arena.

Devices of this type are judged based on two principal benchmarks: (i) the sensitivity to detect end-point displacement, and (ii) the quality factor Q of the resonance. Based on the theory of transducers, outlined in the second chapter and well verified by measurements, the sensitivity of GaN cantilevers can be made significantly higher than in piezoresistive Si devices. If the Q of these GaN resonators can be shown to be comparable, then we have closed the final chapter on the fundamental development of GaN as a candidate material for MEMS. In a sense, the commercial and scientific worthiness of GaN MEMS as an area of research would be established, and further progress in the field could then focus on refinements of the technology applied to specific market needs.

Unfortunately, the data presented in this chapter does not constitute the aforementioned final step of the basic development of GaN MEMS. Though the electrical output from these devices was readily measurable, and in most cases, the sensitivity of the transducers met up with theoretical expectations, the resonance quality factor was found to be rather low. As discussed later, the shortcomings of these devices do not suggest a fundamental crisis for the use of GaN in high Q micro-resonators. Instead, the low Qs are likely rooted in a fabrication rather than a material limitation. In fairness, the data presented here is the first demonstration of a n-GaN cantilever

with an integrated piezoelectric transducer; as a proof of concept, the results were indeed successful.

The first section of this chapter deals with the experimental details surrounding this measurement. These details include the epitaxial structure of the GaN samples, the overall device geometry, and the steps followed during fabrication. Furthermore, we describe the setup used to measure the electrical response of the cantilevers in an evacuated ambient. The next section deals with the theory of piezoelectric transduction through a Schottky contact located on the top surface of the cantilever. The analysis here differs from our earlier results in order to account for the distinct strain conditions inside a bending beam. At the conclusion of this section, we arrive at an expression for the gauge factor of the sensor which relates the output voltage to the end-point deflection of the cantilever. Next, we present measurements of the electromechanical impulse response of the cantilevers in varying ambient pressures, and use this impulse response to infer the Q of the resonators. At this point, we discuss possible damping factors which may limit the Q, and derive a theoretical expression for the acousto-electric dampening which is caused by the ohmic dissipation of electrical currents in the bulk of the semiconductor. Finally, in the conclusion of this chapter, we assess the current state of development of piezoelectric GaN cantilevers, and propose avenues for future research.

4.2 Experimental Setup

Three cantilever samples were tested in this experiment, which we label as **N158A**, **N158B**, and **SVTA**. Each sample employed a distinct combination of transducer with epitaxial structure of the GaN below. However, the basic device geometry in all cases is depicted in the upper portion of Fig. 4.1. Shown there is an array of cantilevers, of length L and width W, with a piezoelectric transducer located at the base where the strain is highest. Connected to each transducer pad is a slightly larger contact pad for wire bonding. Away from the beam array sits a large ohmic contact plane; for all three samples, this ohmic metalization consisted of a sputter deposited

Al/Ni/Au (40 nm/30 nm/50 nm) stack. The following is a description of the epitaxial structure and the transducer deployed in each case:

N158A: The GaN sample used here was grown in house by molecular beam epitaxy (MBE) on a MOCVD template. The template consisted of a 600 nm activated p-type layer grown on top of a lowly n-doped 2.0 μm base layer. The MBE layer consisted of a 1.5 μm intrinsically n-doped epilayer followed by a 0.5 μm surface layer in which the Si doping was ramped from 10^{17} up to 10^{19} $/cm^3$. Because of the very high doping level at the surface, rectifying Schottky contacts could not be created. As a result, for this sample only, a 100 nm Si_3N_4 insulating layer was deposited by plasma enhanced chemical vapor deposition over the entire surface of the sample. A 100 nm Pt layer was then sputter deposited over the insulator to form an array of MIS transducers. The thin Si_3N_4 film was not later removed over the area of the suspended beams.

N158B: This sample came from the same growth described above. In this case, however, the top 1.0 μm of highly doped GaN was first etched away using CAIBE. As a result, it was possible to make leaky but still rectifying Schottky transducers consisting of 100 nm of Pt deposited directly on the semiconductor surface. The Schottky contacts exhibited a rather low differential resistance at zero bias of $\sim 1M\Omega$.

SVTA: This sample was obtained from SVTA Associates and consisted of a 800 nm n-type layer ($N_d \sim 10^{18}/cm^3$) grown atop a very thin 200 nm heavily doped p-type layer. Both epilayers were grown by MBE on a 1 μm intrinsic MOCVD template. As before, leaky Schottky transducers were patterned directly on the semiconductor surface using 100 nm of Pt.

In all cases, the final Pt deposition of the transducer array was accomplished using e-beam lithography followed by lift-off. Once this array was in place, the actual cantilevers were patterned using the standard technique of conventional lithography followed by a CAIBE etch to expose the sacrificial p-type underlayer. The ensuing anodic chemical etch to undercut the cantilevers varied between the samples. For

Sample	Length L (μm)	Width W (μm)	Thickness Δz (μm)	Transducer Type
N158A	1070	155	2.0	MIS
N158B	1070	155	1.0	Schottky
SVTA	1460	155	0.8	Schottky

Table 4.1: Summary of cantilever geometry for the various samples

the case of **N158A**, the beams were etched in KOH (pH 14) with an applied voltage of 4.0 V relative to the solution. The sample was only partially submerged in the solution to prevent contact of the ohmic contact plane with the electrolyte. However, no steps were taken to insulate the gate metal of the transducers because dc current flow from the semiconductor was blocked by the intervening insulating layer. For samples **N158B** and **SVTA**, the etching was performed in phosphoric acid (pH 3) at a 3.7 V bias voltage. As before, the samples were partially submerged, but now the transducers themselves had to be insulated from electrolyte because of their relatively large inherent leakage. This was accomplished by covering the transducers with a layer of photoresist prior to the etch. This layer extended no further than the edge of the metalization on the base of the beams, leaving the remaining length of the cantilevers uncoated. In all cases, the etch was completed in approximately one hour. Following this, the samples were soaked in heated deionized water to remove residual etch by-products. In the case of the latter two samples, this soak was followed by an acetone dip to remove the photoresist. After this stage, the undercut beams were found adhered to the n-GaN layer below; using gentle force from probe tips, they could be freed from the base layer after which they assumed a characteristically upward bent profile. Table 4.1 summarizes the transducer and beam geometry for each sample. The lower left portion of Fig. 4.1 shows a side view of the epitaxial structure of the undercut n-GaN layer with the associated transducer atop for all three cases.

To perform electrical measurements on the piezoelectric cantilevers, the samples were mounted on a custom circuit board and connected by means of wire bonds. As depicted in the schematic on the lower right of Fig. 4.1, the output from the transducer went to the input of a $\times 50$ non-inverting amplifier which was mounted

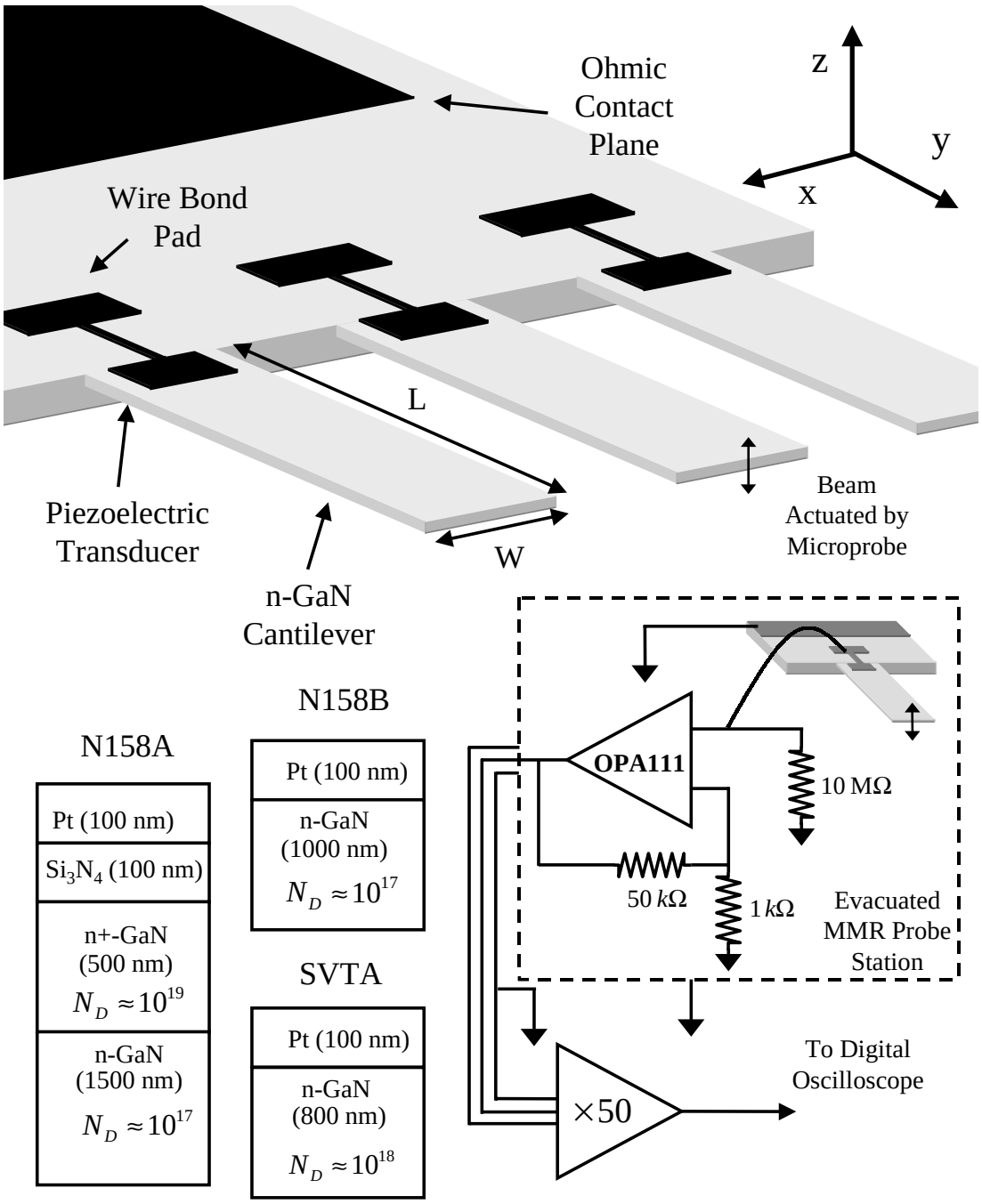

Figure 4.1: [Top]: Schematic diagram of n-GaN cantilever array with integrated piezoelectric transducers. [Bottom left]: Side view of epitaxial layer and transducer associated with each sample. [Bottom right]: Schematic of the electrical setup used to measure the impulse response of the cantilevers. The dashed line corresponds to the boundaries of the MMR probe station which was evacuated to varying pressure levels.

on the same board in close proximity to the sample to minimize the effects of stray capacitance (see Chapter 2). The OPA111 operational amplifier was chosen for its low voltage noise and high input impedance. To prevent saturation, a 10 $M\Omega$ resistor was used to shunt the input stage to ground. The entire circuit board (including batteries to power the op-amp) was loaded into a MMR probe station capable of moderate ($\geq$1 mTorr) vacuum levels. As seen in the figure, the output from the amplifier was connected to the exterior by means of an electrical feedthrough; from there, it traveled along a shielded cable to a second $\times$50 gain stage and ultimately to a digital oscilloscope. To excite the cantilevers, a probe tip first depressed the free end vertically, and then retracted laterally along the length until it came off the tip completely. In this way, the mechanical impulse response of the beams could be measured, from which the gauge factor and Q could be inferred.

4.3 Theory of Transduction for Simple Beams

In the following section, we aim to understand the behavior of a simple Schottky transducer integrated onto a GaN cantilever. The ultimate goal here is to derive an expression which predicts the voltage generated across the diode as a function of the displacement of the lever. This analysis is somewhat more complicated than our earlier results because of the non-uniform strain profiles in a moving beam. An understanding of the gauge factor is nonetheless vital, for it provides a means to compare Schottky diodes with other methods of transduction on these microstructures. In the first part of this section, we briefly quote relevant equations in the well established elastic theory of beams. In the second part, this theory is incorporated into the electrostatic analysis of the Schottky diode, leading to a general expression for the gauge factor of a transducer situated arbitrarily along the top surface of a cantilever.

4.3.1 Basic Elastic Theory for Cantilevers

As mentioned before, the basic elastic theory of beams has long been well understood; in this section, we merely quote results from the wide literature on the subject [1][2].

Referring to the coordinate axis of Fig. 4.1, the y-axis measures distance along the length (L) of the cantilever starting from the base, x along the width (W), and z along the thickness (Δz) with z = 0 located at the neutral axis, or geometrical center, of the beam. For longitudinal bending modes, the strain in the cantilever can be characterized by the local radius of curvature R which varies along the length of the beam. At a particular point along the length, the strain is predominantly longitudinal in y. This strain component S_2 will vary in height as:

$$S_2 = -\frac{z}{R} \tag{4.1}$$

where R is local radius of curvature of the beam. The strain will be zero along the neutral axis, compressional on one half of the thickness, and extensional on the other half. For these modes, the deformation of the beam can be specified by a function z(y) which measures the local vertical deflection of the beam from its unstrained state. Using this deflection, the local curvature will be given by:

$$\frac{1}{R} = \frac{d^2z}{dy^2}\left[1 + \left(\frac{dz}{dy}\right)^2\right]^{-3/2} \approx \frac{d^2z}{dy^2} \tag{4.2}$$

where the last approximation is valid in the limit of small deflection. If the beam is rigidly anchored at its base, the equations of motion will yield normal mode solutions for z(y) of the form:

$$z(y,t) = A\left[(\cos(k_n y) - \cosh(k_n y)) + \alpha_n(\sin(k_n y) - \sinh(k_n y))\right]\cos(\omega_n t) \tag{4.3}$$

Here, k_n and α_n are constants which depend upon the mode in question; for the first five modes, they have values of:

$$k_n L = 1.875, 4.694, 7.855, 10.996, 14.137 \tag{4.4}$$

and

$$\alpha_n = -0.7341, -1.0185, -0.9992, -1, -1 \tag{4.5}$$

The frequency of vibration ω_n appearing on the right-hand-side of Eqn. 4.3 is related to k_n via:

$$k_n^4 = \frac{12\rho}{Y\Delta z}\omega_n^2 \tag{4.6}$$

where ρ is the mass density and Y is the Young's modulus respectively. Combining Eqns. 4.4 and 4.6 gives the resonant frequency for the first (fundamental) mode:

$$\omega_1 \approx \frac{\Delta z}{L^2}\sqrt{\frac{Y}{\rho}} \tag{4.7}$$

For a particular mode, the strain S_2 will depend upon height (z) and distance (y) along the beam via:

$$S_2(y,z,t) = -zk_n^2 A\left[-(\cos(k_n y) + \cosh(k_n y)) - \alpha_n(\sin(k_n y) + \sinh(k_n y))\right]\cos(\omega_n t) \tag{4.8}$$

The displacement of the cantilever z(y) for the lowest four normal modes is depicted in the upper portion Fig. 4.2; the corresponding strain is shown in the lower portion. Note that for all modes, the strain is largest at the base of the beam where the transducers were situated in this experiment.

4.3.2 Integrated Schottky Transducers

Eqn. 4.1, which describes the variation in strain vertically (in z) at a particular point (y) along the length of the beam, is the starting point to describe the behavior of Schottky transducers integrated onto a cantilever. To facilitate this description, we will assume for the moment that any variation in strain with y is small over the extent of the Schottky contact so that we may treat the local radius of curvature R appearing in Eqn. 4.1 as constant. Later, we will relax this restriction to accommodate laterally non-uniform strain under the transducer. Furthermore, we will assume that the strain S_2 follows a simple harmonic time dependence with a frequency ω.

Since the strain is not uniform in z, the distribution of piezoelectric bound charge will differ from our earlier results. In addition to the bound sheet charges at either

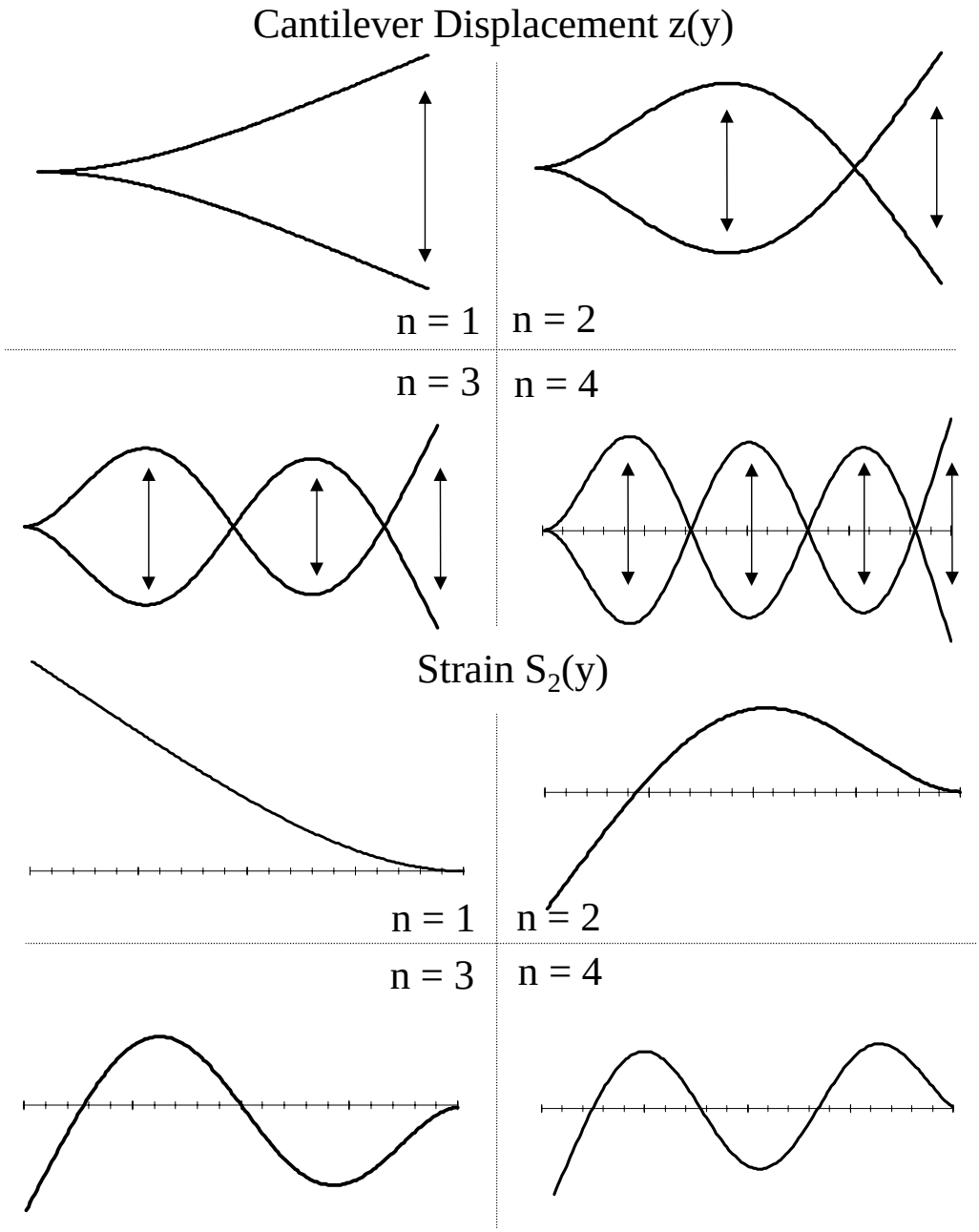

Figure 4.2: [Top] Displacement envelopes for the first four normal modes of a cantilever. The beam is anchored to the left side. [Bottom] Strain S_2 at the top surface during the peak displacement of the cantilever for the first four modes.

surface of the beam, there will be a distributed volume bound charge whose density ρ_b is given by:

$$\rho_b \equiv -\nabla \cdot \vec{P} = -e_{32}\frac{dS_2}{dz} = \frac{e_{32}}{R} \tag{4.9}$$

The surface sheet charges in this case will both have the same sign; their common areal density will be:

$$\sigma_b = -e_{32}\frac{\Delta z}{2R} \tag{4.10}$$

where Δz is the thickness of the cantilever. Note that the total bound charge, integrated over the entire thickness, will always remain zero.

At the top surface of the GaN, immediately under the Schottky contact, a finite depletion region extends into the bulk of the semiconductor. Likewise, at the bottom surface, a depletion region is likely to exists as a result of surface charge or spontaneous piezoelectric fields. Inside the bulk of the GaN layer, away from either surface, will be a field free region populated by free electrons. As before, we will assume that this bulk region will always remain field free even in the presence of time varying bound charges. The validity of this assumption depends upon the speed at which the free carriers redistribute themselves to expel an electric field. Provided that the period of a strain cycle is much longer than the dielectric relaxation time of the semiconductor, the bulk region will always remain field free. Since no electric field exists in the bulk, if we make a Gaussian pill box with its top surface in the metal and bottom surface in the bulk, the total charge (both free and bound) contained within must be zero. Working in the depletion approximation, we arrive immediately at the following charge neutrality equation:

$$\sigma_m + W(qN_d + \rho_b) + \sigma_b = 0 \tag{4.11}$$

where σ_m is the free sheet charge on the metal surface and W is the depletion layer width.

To determine the voltage generated across the diode in response to strain, we start from the familiar electrostatics of a Schottky junction [3], but must add the volume

bound charge ρ_b to the ordinary background of ionized dopants:

$$V_{bi} - V = \frac{(qN_d + \rho_b)W^2}{2\epsilon_s} \tag{4.12}$$

By combining the time derivatives of Eqn. 4.12 and Eqn. 4.11, we find that:

$$\frac{dV}{dt} = \frac{1}{\epsilon_s}\left[\frac{W^2}{2}\frac{d\rho_b}{dt} + W\frac{d\sigma_m}{dt} + W\frac{d\sigma_b}{dt}\right] \tag{4.13}$$

Since the time rate of change of the bulk and surface bound charges are fully dictated by the strain, the electromechanical voltage could now be solved once the dynamics of the metal charge is known. As before, we assume that the flow of free charge from the metal to the semiconductor is governed by:

$$\frac{Ad\sigma_m}{dt} = -\frac{V}{Z} \tag{4.14}$$

where Z is effective impedance of all stray paths which shunt the Schottky diode, including the intrinsic leakage paths of the device itself. When Eqn. 4.14 is substituted into Eqn. 4.13, and the relations between the two bound charge densities are invoked, the voltage can be solved by using small signal techniques:

$$V(t) = \left[\frac{1}{i\omega C_d + 1/Z}\right] Ai\omega\frac{e_{32}}{2R}(W - \Delta z) \tag{4.15}$$

where A is the device area and $C_d = A\epsilon_s/W$ is the diode capacitance. At the frequencies of interest in this experiment, the effective impedance Z will be that of the usual parallel capacitance/resistance pair:

$$\frac{1}{Z} = \frac{1}{R'} + i\omega C_{stray} \tag{4.16}$$

where C_{stray} is the stray capacitance and R' is the net resistance (including both the bias resistor and the intrinsic leakage resistance of the diode). Furthermore, we can eliminate the radius of curvature in Eqn. 4.16 by expressing it in terms of the

(maximum) strain S_2^m at the upper surface of the GaN layer ($z = \Delta z/2$). Folding in both results, we arrive at a final expression for the voltage generated across the transducer which is applicable to our measurement conditions:

$$V(t) = \left[\frac{R'}{1 + i\omega R'(C_d + C_{stray})}\right] Ai\omega e_{32} S_2^m (1 - W/\Delta z) \tag{4.17}$$

Note this result is very similar to that obtained for the case of a uniform strain, the only difference being the extra term on the very right-hand-side which acts to diminish the voltage as the depletion width approaches the layer thickness. In practice, this term is not of great significance because the depletion width under the transducer can be no larger than roughly half the actual beam thickness. If this were not the case, considering the finite depletion layer likely at the bottom surface, the entire thickness of the beam could be devoid of carriers and no piezoelectric voltage would form. These statements are the basis of an important design rule for integrated cantilevers, namely, for a given doping level of the semiconductor, the minimum beam thickness is roughly twice the Debye length: $\Delta z \geq\sim 2L_D$.

For the cantilevers tested in this experiment, the strain was not uniform laterally under the area of the transducer. To extend Eqn. 4.17 to handle this case, we can imagine decomposing the transducer into a collection of differential area elements. Each element has a capacitance proportional to its area, and each will contribute a piezoelectric current proportional to its area and the local strain. Each element is therefore electrically equivalent to a current source across a capacitor; the overall transducer is simply the sum of all these equivalent circuits connected in parallel. It is obvious then that the current sources will sum, the capacitances will sum, and the only modification required to Eqn. 4.17 is to replace the constant strain S_2^m with:

$$S_2^m \rightarrow \frac{1}{A}\int_A S_2^m(x, y)dA \tag{4.18}$$

where the integral is performed over the transducer area. In other words, a transducer acting over a non-uniform strain field will generate a response proportional to the

average strain under its area.

To determine the relation between the output voltage and the endpoint displacement of the cantilever, we can use Eqns. 4.8 and 4.3 to solve for the surface strain at the base of the cantilever $S_2^m(y=0)$ in terms of the peak deflection at the end $z(L)$:

$$S_2^m(y=0) = \left(\frac{\Delta z}{L}\right)\left(\frac{z(L)}{L}\right) \times (-1.76, +11.0, -30.4, +63.8, ...) \tag{4.19}$$

where the numeric constants on the right hand side depend upon the normal mode in question. At this stage, plugging the base strain into Eqn. 4.17 would allow us to predict the output voltage that would be expected if the cantilever is excited in a particular mode with a given endpoint amplitude. For the first mode, the maximum voltage that could be generated for an ideal measurement circuit ($C_{stray} = 0$, $R_b = \infty$) is given by:

$$V \approx \frac{e_{32}}{c_d} S_2^m(0)\left(1 - \frac{W}{\Delta z}\right) = 1.76 \times \frac{e_{32}}{c_d}\left(\frac{\Delta z - W}{L}\right)\left(\frac{z(L)}{L}\right) \tag{4.20}$$

where c_d is the transducer capacitance per unit area. We will return to this result in the next section where we evaluate the measured gauge factors of the integrated GaN cantilevers.

4.4 Results and Discussion

4.4.1 Impulse Response Data

Fig. 4.3 shows a representative time series of the impulse response measured on an integrated cantilever from sample **N158A**. The lower portion of the figure (Fig. 4.3(b)) shows the measured voltage from the transducer in a narrow window of time within which the beam was released. At the onset of ringing, the initial endpoint deflection, normalized by the length of the cantilever, was estimated to be $z(L)/L \sim 0.1$. The voltage scale seen on this graph is referred to the input of the first amplification stage, i.e., it is a direct measure of the voltage generated by the piezoelectric transducer. It

is clear from the trace that the mechanical excitation of the cantilever is dominated by the first mode, in this case at a frequency of 2900 Hz. Fig. 4.3(a) shows the same data but viewed over a much longer time scale. Here, the individual cycles of the beam are obscured, but an overall exponential decay of the signal amplitude is quite evident. We will return to this later in our discussion of the quality factor.

Fig. 4.4(a) shows the Fourier transform of the impulse response for a typical cantilever from sample **SVTA**. As with sample **N158A**, the spectrum is dominated by the first normal mode, in this case at a frequency of 400 Hz. The inset of the graph shows an expanded view of the first resonant peak. However, other peaks are evident at higher frequency. Using Eqn. 4.6 from earlier, we can predict the frequencies of the higher order longitudinal modes by means of:

$$\frac{\omega_n}{\omega_1} = \left(\frac{k_n}{k_1}\right)^2 \tag{4.21}$$

Fig. 4.4(b) shows the same spectrum in log scale over a wider frequency range; the black bars on the upper axis of this plot are situated at the predicted frequencies of the higher modes using 400 Hz as the fundamental in Eqn. 4.21. Note that the observed spectrum exhibits peaks in fairly good correspondence with prediction. The extraneous peaks seen in the plot are likely due to torsional modes of the cantilever.

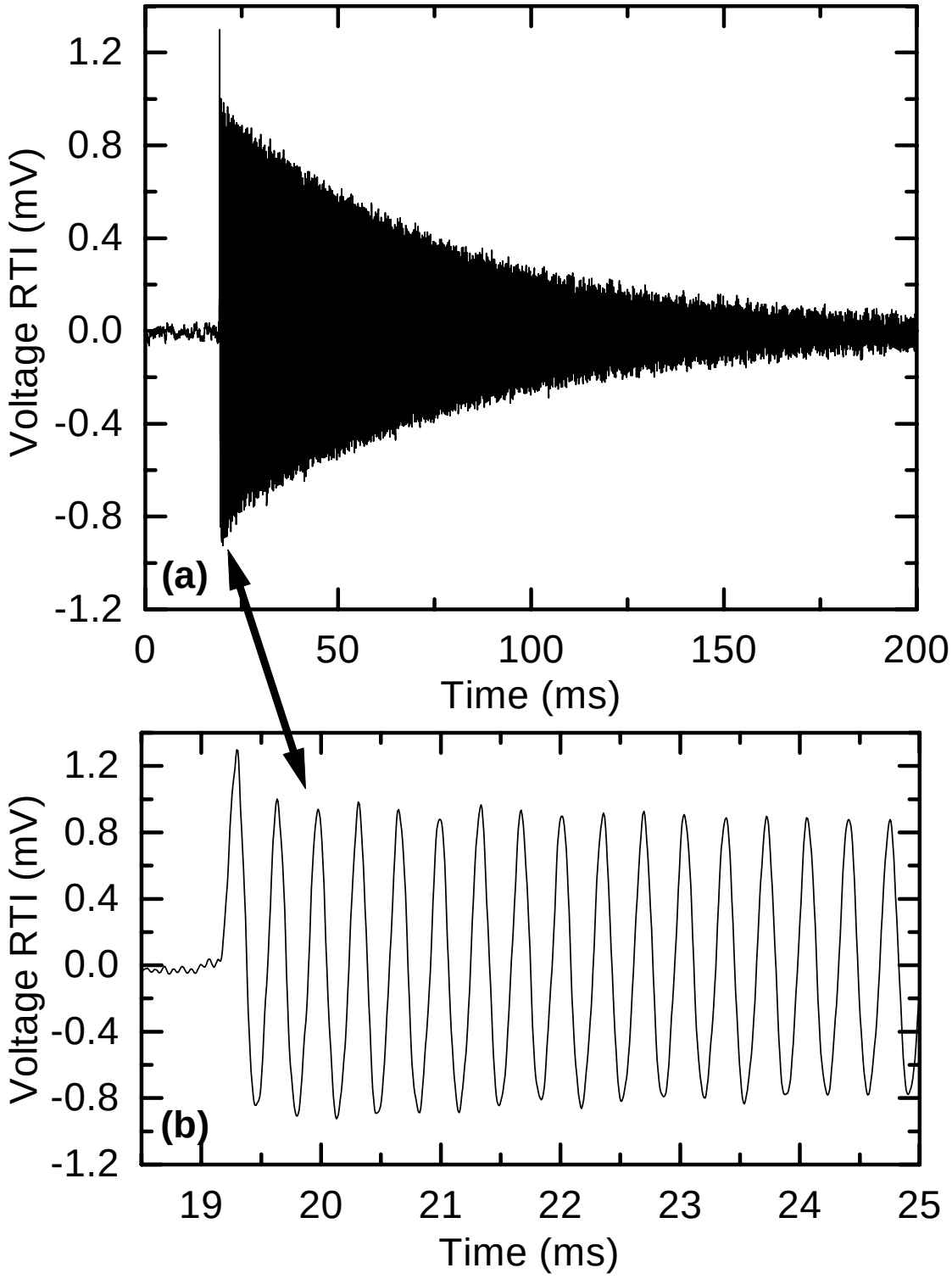

Figure 4.3: (a) Impulse response of a typical GaN cantilever from sample **N158A** viewed over a long time scale. (b) Enlarged view of the same data at the onset of ringing. The initial endpoint deflection, normalized by beam length, was estimated to be $z(L)/L \sim 0.1$. All voltages are referred to the input of the first amplification stage.

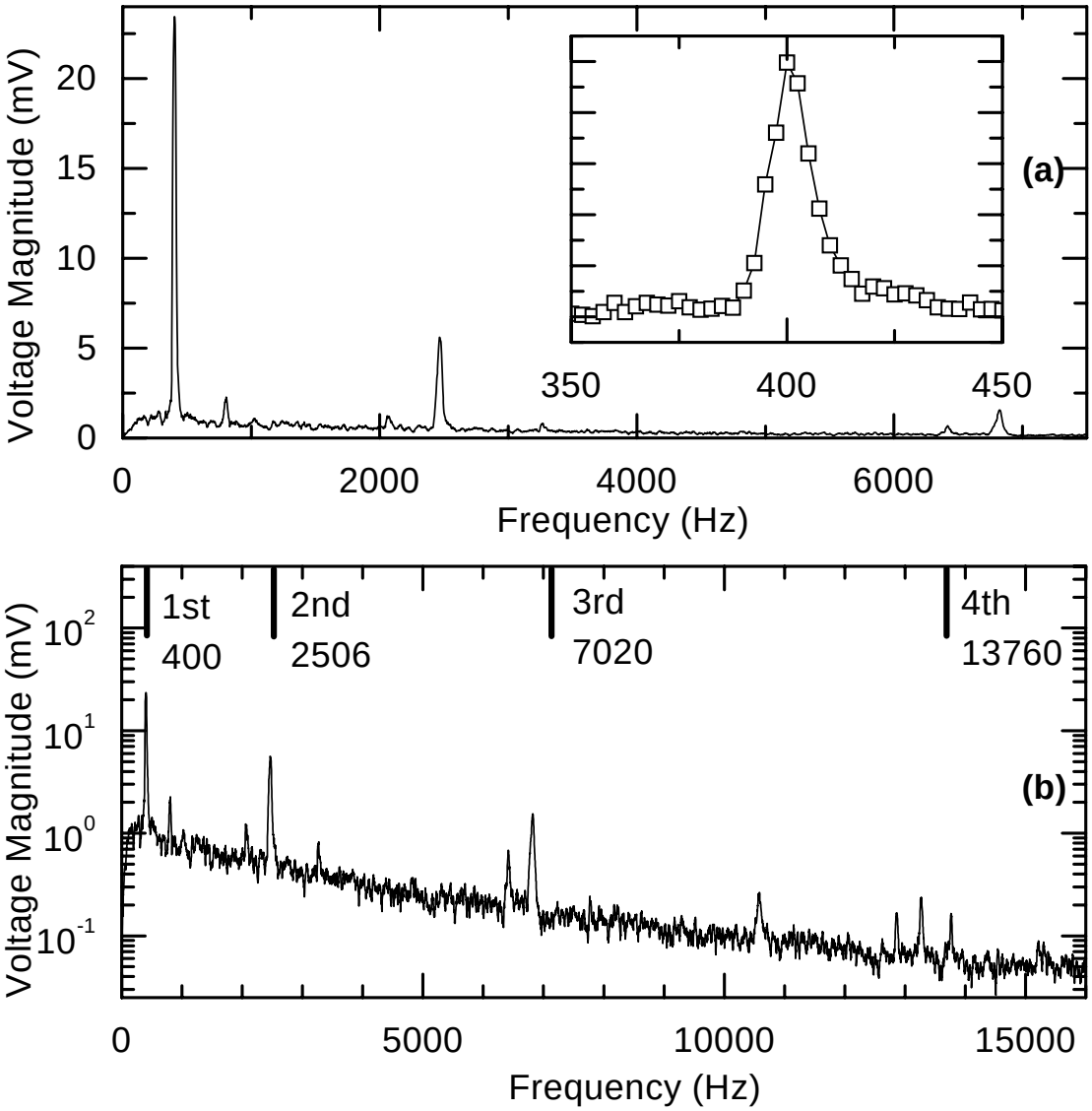

Figure 4.4: (a) Fourier transform of the impulse response of a typical cantilever from sample **SVTA**. The inset shows an expanded view of the lowest order resonance peak. (b) Log-scale view of the same data over a wider frequency range. The black bars on the upper axis correspond to frequencies for the first four modes predicted by elementary beam theory.

Sample	Observed f_0 (Hz)	Theory f_0 (Hz)	Observed GF (V)	Theory GF_{max} (V)
N158A	2900	2160	1.3×10^{-2}	2.02×10^{-2}
SVTA	400	464	0.24×10^{-2}	1.88×10^{-2}
N158B	?	1080	?	1.01×10^{-1}

Table 4.2: Comparison of data and theory for the resonance frequency and gauge factor of the three GaN cantilever samples.

A comparison of the theoretical and observed lowest order resonant frequency (f_0) for the GaN cantilevers is shown in the first two columns of Table 4.2. The theoretical numbers were derived from Eqn. 4.7 using a Young's modulus of $Y = 367$ GPa [4] and a mass density of $\rho = 6.1 \times 10^3$ kg/m^3 [5] both obtained from the nitride literature. Note that for the first two samples listed in the table, the measured f_0 agrees fairly well with prediction given the lingering uncertainty of the GaN material constants. No data was available for sample **N158B** because it yielded no measurable piezoelectric output under strain.

The last two columns of Table 4.2 refer to the gauge factor (GF) of the cantilevers, an important figure of merit which we define in this context by:

$$V = GF \times \frac{z(L)}{L} \tag{4.22}$$

Thus, GF will determine the voltage output by the transducer for a given normalized endpoint amplitude. Comparing Eqn. 4.22 with Eqn. 4.20 from the theory of Schottky transducers, the maximum GF (for an ideal read-out circuit) of an integrated GaN beam in its lowest mode will be:

$$GF_{max} = 1.76 \times \frac{e_{32}}{c_d} \left(\frac{\Delta z}{L} \right) \tag{4.23}$$

To calculate this theoretical maximum, a piezoelectric constant of e_{32} = -0.44 C/m^2 was used [5]. Furthermore, since the empirical C-V data on these transducers was unrevealing, we were forced to estimate the capacitance per unit area using $c_d = \epsilon_s / L_D$, where L_D is the Debye length derivable from the doping level. As seen in Table 4.2, sample **N158A** exhibited a gauge factor reasonably close to the theoretical

maximum of our theory; this is not surprising given its relatively high f_0 and its negligible diode leakage. Sample **SVTA** operated at a lower frequency and, because it employed Schottky rather than MIS transducers, displayed a low intrinsic leakage resistance of $\sim$1 MΩ. Therefore, it is not surprising that the gauge factor here was considerably lower than the maximum for an ideal circuit; note, however, that the agreement between experiment and theory was still within an order of magnitude. While the first two results were comprehensible and even encouraging, the behavior of sample **N158B** remains a mystery. From a theoretical basis, this sample was projected to have the highest sensitivity due to its relatively low doping in the GaN layer. Though the diodes suffered from rather poor blocking, they were roughly on par with those in sample **SVTA**. No cantilever tested on this sample gave an impulse response that was detectable over the noise floor of the amplifier. It is possible that the transducers were compromised during the chemical etch due to a breakdown of the protective photoresist layer that was observed in their vicinity. As a result, the Pt contacts were partially lifted off the GaN at the base of the beams, and suffered from visible discoloration. Because the transducers were connected to wire-bond pads away from the damaged area, there was no real means to probe the electrical integrity of the Schottky contact on the base of the cantilever. Clearly, further investigation is needed to flush out the source of the low GF for this sample.

4.4.2 Resonance Quality Factor

To measure the quality factor of the GaN integrated cantilevers, we used the so-called *ring down* method [6] in which the measured impulse response voltage $v(t)$ is fit to an equation of the form:

$$v(t) = A \exp\left[-\frac{ft}{2Q}\right] \cos(2\pi f t) \equiv A \exp\left[-\frac{t'}{2Q}\right] \cos(2\pi t') \tag{4.24}$$

where f is the frequency of vibration and $t' \equiv ft$ is the wavecycle. Fig. 4.5 shows the amplitude envelopes for two traces recorded on sample **N158A** at different background pressure levels. The envelopes were obtained by applying a moving average

(spanning several cycles of oscillation) to the absolute value of the raw impulse response function. The time axis in these plots was rescaled to measure the wavecycle t'. The lower plots in the figure show the same data in log scale; superimposed on each envelope is an exponential fit to the data (with an additive offset to account for the noise floor). Note that the actual envelopes do indeed follow an exponential decay law. Using the values from the fit, with due reference to Eqn. 4.24, the Q of the resonator could be measured as a function of ambient pressure.

The results of this technique are shown in Fig. 4.6, which plots the Q of an **N158A** cantilever versus the background pressure. The general trend of the data here is consistent with that reported throughout the MEMS literature [7]. It is clear from this figure that fluid damping limits the quality factor for pressures in excess of $\sim$10 mTorr; at lower pressure, however, some other damping mechanism becomes dominant. For a cantilever of this size, the Q of 100 measured here compares very unfavorably with that achieved in other material systems, where Q's in excess of 10^4 are routinely achieved [8].

Based on a visual inspection using a microscope over the probe station, there was no significant difference in the *ring down* time between cantilevers connected to the read-out circuit and those not; thus, electrical dissipation in this circuit is not the cause of the low Q. Electrical dissipation in the bulk of the cantilever itself, brought on by free currents responding to the changing piezoelectric fields, is known as acoustoelectric dampening [6]. This effect is considered in depth below, and it is found to be far too small to explain the low Q. All attempts to stiffen and anchor the beams at their base to minimize *anchor* or *clamping* [8] losses were likewise found to be inconsequential. For dissipation this strong, the most likely candidate is viscoelastic dampening [6] in thin films of residual etch by-products which coat the surfaces of the cantilever. These by-products formed colorful deposits that were particularly concentrated at the underside of the base of the beam; elsewhere, their presence could be detected in the scratch marks left by a probe tip. Clearly, the source of these viscoelastic deposits must be identified, and processing steps must be developed to either remove them or prevent their initial formation.

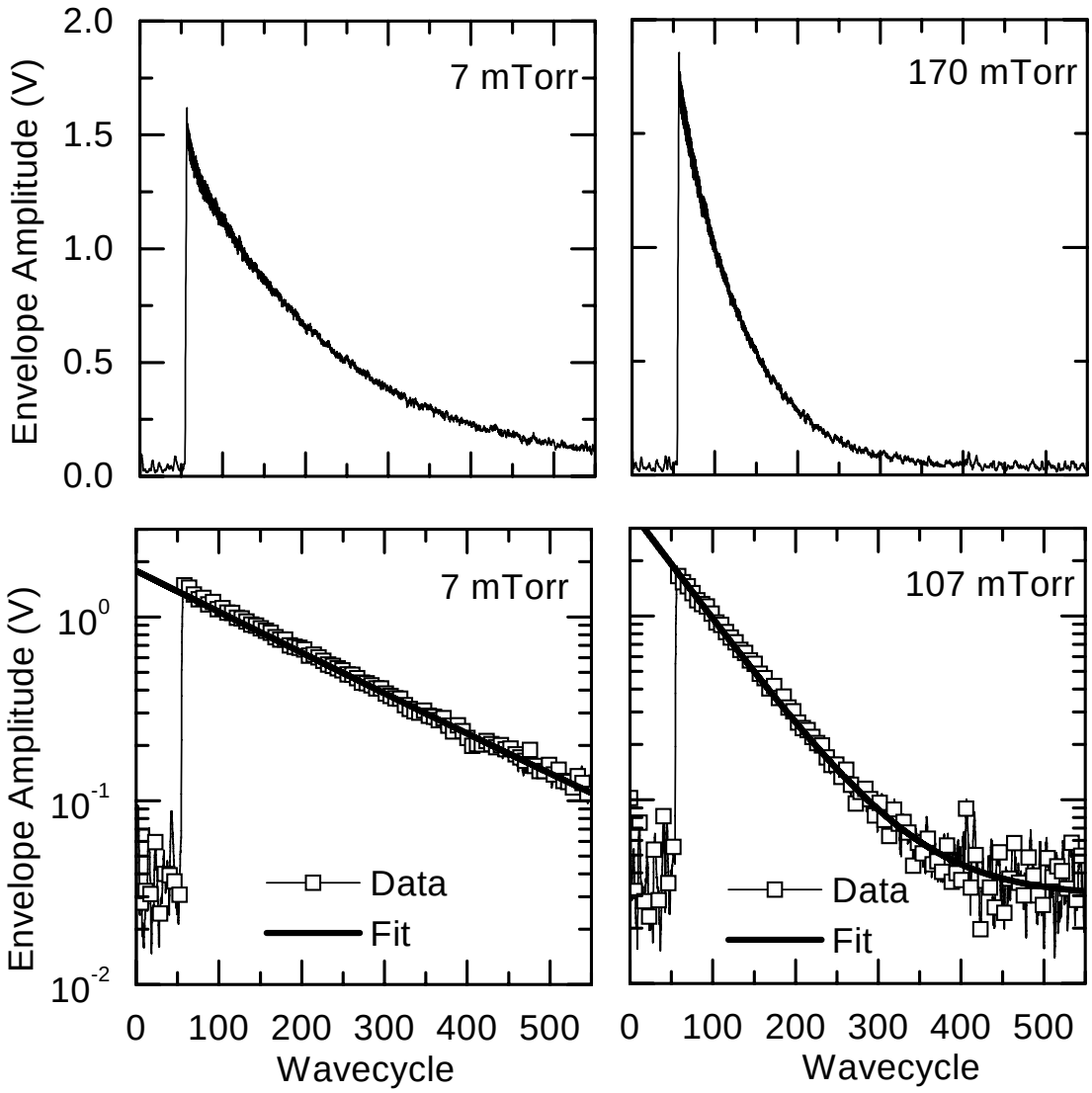

Figure 4.5: [Top]: Amplitude envelope of the impulse response of a **N158A** cantilever at two ambient pressures. [Bottom]: Log-scale view of the same envelopes with an exponential fit superimposed on the data. The horizontal axis measures time in wavecycles, or periods of the fundamental resonant frequency.

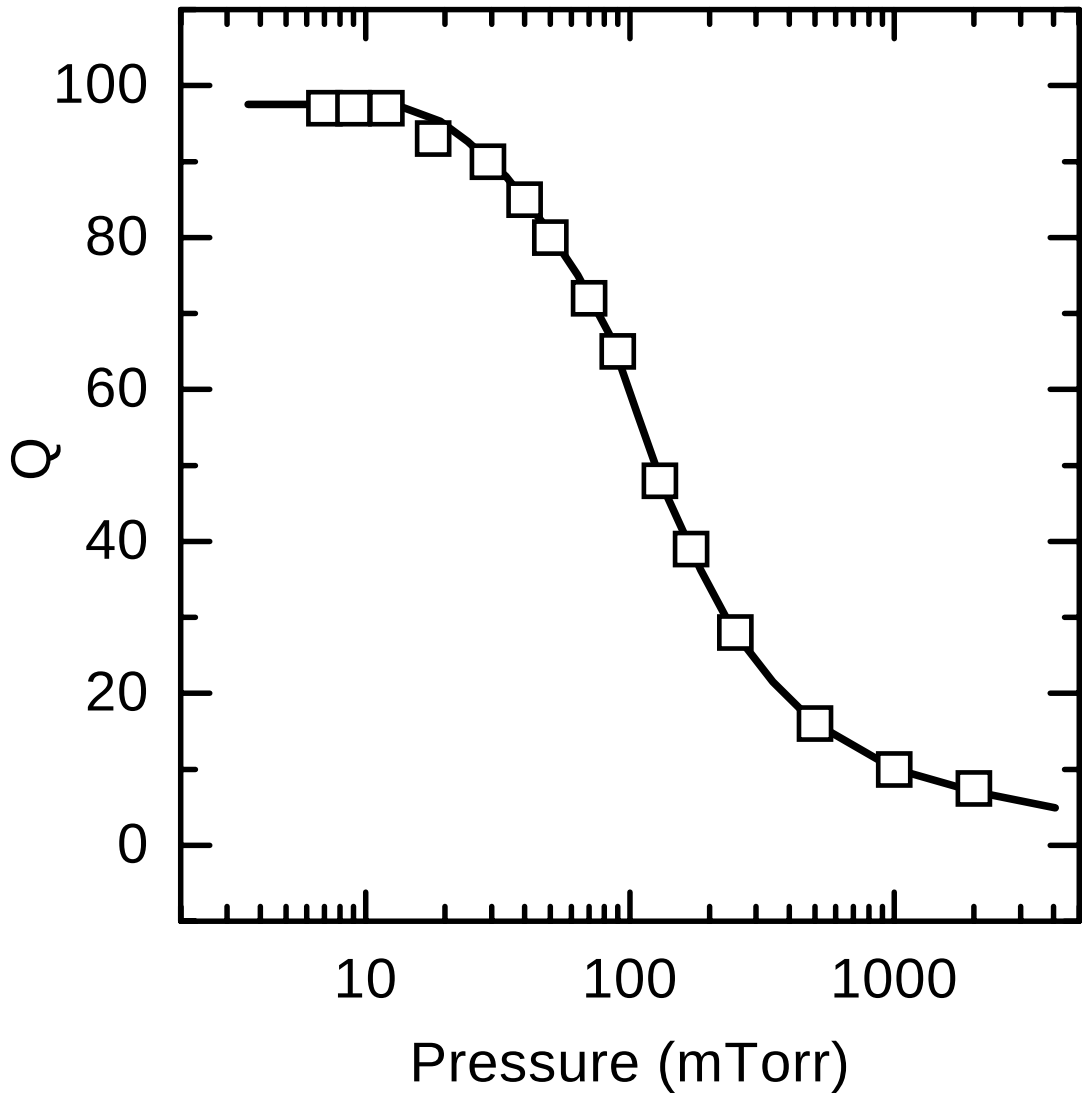

Figure 4.6: Quality factor of a **N158A** cantilever as a function of ambient pressure. Solid line is an aid to the eye.

4.4.3 Acoustoelectric Damping

The unique combination of piezoelectric activity with free charge carriers, possible in the III-nitrides, allows for the simple yet powerful transducers discussed throughout this text. An important concern, however, is whether this same combination could lead to a serious limitation of the Q in GaN micro-resonators. Acoustoelectric dampening, or ohmic dissipation of free currents responding to piezoelectric bound currents, has been extensively studied throughout the sensor community [6]. For a conventional piezoelectric resonator, the acoustoelectric loss occurs in metal films in contact with an otherwise insulating piezoelectric crystal. In the case of doped GaN, however, this loss will occur within the bulk of the semiconductor. In the following, we will calculate the acoustoelectric dampening for the specific geometry of a cantilever and thereby find the upper limit it sets on the quality factor Q_{ae} of such a resonator.

To set the stage for this calculation, we imagine a bare GaN cantilever with no integrated transducer or any other extraneous material covering its surface. As the beam resonates, free currents $\vec{J_f}$ will arise in the semiconductor in response to the local piezoelectric fields. Since, at any place along the length of beam, the bound charge will always integrate to zero, these free currents will be directed only in z across the beam thickness.

Locally, the ohmic dissipation per unit volume w from this free current is given by:

$$w = \vec{J_f} \cdot \vec{E} = \frac{1}{\sigma}\vec{J_f^2} = \frac{1}{\sigma}J_{f,z}^2 \tag{4.25}$$

where σ is the conductivity. We know from our discussions earlier that within the cantilever, away from any surface depletion regions, the free carriers will adjust to preserve overall neutrality of free and bound charge. Since the distributed bound charge density ρ_b is constantly changing in the bulk, so too must the free electron concentration (n). This will be accomplished by a continual exchange of electrons between the bulk and either the surface depletion regions or the surfaces themselves, but the exact details of this exchange are not important. The bulk charge neutrality

relation can be stated as:

$$qn(t) = qN_d + \rho_b(t) \tag{4.26}$$

where N_d is the doping density.

Consider a particular point y along the beam at which the local radius of curvature R(y) varies in time with a frequency ω_n. Making use of Eqn. 4.9, the electron concentration there must satisfy:

$$qn(t) = qN_d + \frac{e_{32}}{R}\cos(\omega_n t) \tag{4.27}$$

From the continuity equation, the electron current necessary to maintain this balance in time is given by:

$$J_{f,z} = \frac{e_{32}}{R} z\omega_n \sin(\omega_n t) \tag{4.28}$$

Combining Eqns. 4.28 and 4.25, we find that the energy dissipated Δe per unit volume in a single cycle is given by:

$$\Delta e = \frac{1}{\sigma}\left(\frac{e_{32}}{R}\right)^2 z^2 \pi\omega_n \tag{4.29}$$

Meanwhile, the mechanical energy density e_m present at the same location in the cantilever is simply:

$$e_m = \frac{1}{2} Y S_{32}^2 = \frac{1}{2} Y \left(\frac{z}{R}\right)^2 \tag{4.30}$$

The quality factor of the resonator, if it were limited by acoustoelectric dampening only, will be given by the ratio of the total mechanical energy in the beam to the total energy lost in a cycle:

$$Q_{ae} = \frac{E}{\Delta E} = \frac{\int_V e dV}{\int_V \Delta e dV} = \frac{Y}{2\pi\omega_n}\left(\frac{\sigma}{e_{32}^2}\right) \tag{4.31}$$

where we have integrated Eqns. 4.30 and 4.29 over the entire volume of the cantilever. For the first mode of the cantilever, which was the dominant mode in our test

Sample	Sheet Resistance ρ_s (Ω)	Q_{ae}
N158A	30	3×10^{11}
SVTA	750	8×10^{10}
N158B	6000	7×10^{9}

Table 4.3: Calculated quality factors for the three cantilever samples from acousto-electric dampening alone.

conditions, the quality factor will be:

$$Q_{ae} = \frac{1}{2\pi}\sqrt{(Y\rho)}\left(\frac{1}{\rho_s e_{32}^2}\right)\left(\frac{L}{\Delta z}\right)^2 \tag{4.32}$$

where ρ_s is the sheet resistance of the GaN layer related to the conductivity by $\rho_s = (\sigma \Delta z)^{-1}$.

Table 4.3 lists the Q_{ae} for the three samples in this experiment calculated on the basis of Eqn. 4.32. It is quite clear from these numbers that acoustoelectric dampening was not the limiting loss mechanism in this experiment. Furthermore, it will never present a fundamental material limit for GaN micro-resonators.

4.5 Conclusions

In summary, the successful integration of piezoelectric transducers on suspended n-GaN cantilevers was demonstrated. An expression was derived for the gauge factor of these transducers, and it was found, in two of three samples, that the measured values were in reasonable agreement with theory. Furthermore, data was presented on the quality factor of these resonators measured in vacuum. The Q's were found to be $\sim$100, much lower than those reported in other material systems [8]. We derived an expression for the acoustoelectric dampening in a GaN cantilever, and found that this loss mechanism does not present an inherent limit on the use of GaN for high Q micro-resonators.

Further research in this area should focus on the problem of obtaining higher Q's. It is likely that the root cause lies in viscoelastic deposits that result from the wet etch process. These by-products must be characterized, and post-processing steps or

alternate etch chemistries must be developed to either remove them or prevent their initial formation. With further refinements of the device processing, the outlook for integrated GaN micro-devices seems promising.

Bibliography

[1] D. Sarid, *Scanning Force Microscopy*, 1st ed. (Oxford University Press, New York, NY, USA, 1991).

[2] K. Graff, *Wave Motion in Elastic Solids*, 1st ed. (Oxford University Press, New York, NY, USA, 1975).

[3] S. Sze, *Physics of Semiconductor Devices*, 2nd ed. (John Wiley & Sons, Inc., New York, NY, USA, 1981).

[4] A. Wright, Journal of Applied Physics **82**, 2833 (1997).

[5] A. Zoroddu, F. Bernardini, P. Ruggerone, and V. Fiorentini, Physical Review B **64**, 1 (2001).

[6] D. Ballantine, R. White, S. Martin, A. Ricco, E. Zellers, G. Frye, and H. Wohltjen, *Acoustic Wave Sensors*, 1st ed. (Academic Press, San Diego, CA, USA, 1997).

[7] A. Duwel, J. Gorman, M. Weinstein, J. Borenstein, and P. Ward., Sensors and Actuators A **103**, 70 (2003).

[8] V. Srikar and S. Senturia, Journal of Microelectromechanical Systems **11**, 499 (2002).